INTERACTIONS OF LITHIUM-CARBON NANOSYSTEMS: MOLECULAR DYNAMICS SIMULATIONS AND DENSITY FUNCTIONAL THEORY CALCULATIONS

A THESIS SUBMITTED TO
THE GRADUATE SCHOOL OF NATURAL AND APPLIED SCIENCES
OF
MIDDLE EAST TECHNICAL UNIVERSITY

BY

RENGİN PEKÖZ

IN PARTIAL FULFILLMENT OF THE REQUIREMENTS
FOR
THE DEGREE OF DOCTOR OF PHILOSOPHY
IN
PHYSICS

SEPTEMBER 2008

Approval of the thesis:

INTERACTIONS OF LITHIUM-CARBON NANOSYSTEMS: MOLECULAR DYNAMICS SIMULATIONS AND DENSITY FUNCTIONAL THEORY CALCULATIONS

submitted by **RENGİN PEKÖZ** in partial fulfillment of the requirements for the degree of **Doctor of Philosophy in Physics Department, Middle East Technical University** by,

Prof. Dr. Canan Özgen
Dean, Gradute School of **Natural and Applied Sciences**

Prof. Dr. Sinan Bilikmen
Head of Department, **Physics**

Prof. Dr. Şakir Erkoç
Supervisor, **Physics**

Examining Committee Members:

Prof. Dr. Vedat Akdeniz
METE, METU

Prof. Dr. Şakir Erkoç
Physics, METU

Prof. Dr. Demet Gülen
Physics, METU

Assoc. Prof. Dr. Oğuz Gülseren
Physics, Bilkent University

Assoc. Prof. Dr. Hatice Kökten
Physics, METU

Date: 26.09.2008

I hereby declare that all information in this document has been obtained and presented in accordance with academic rules and ethical conduct. I also declare that, as required by these rules and conduct, I have fully cited and referenced all material and results that are not original to this work.

Name, Last Name: RENGİN PEKÖZ

Signature :

ABSTRACT

INTERACTIONS OF LITHIUM-CARBON NANOSYSTEMS: MOLECULAR DYNAMICS SIMULATIONS AND DENSITY FUNCTIONAL THEORY CALCULATIONS

Peköz, Rengin
Ph.D., Department of Physics
Supervisor : Prof. Dr. Şakir Erkoç

September 2008, 88 pages

Single walled carbon nanotubes have been attracting interest for their electronic, magnetic, chemical and mechanical properties. Moreover, since they are ideal nano-containers, the adsorption and absorption properties provide them to be used as Li/Li$^+$ ion batteries. The capacity, rate capability and cycle life of the batteries are the important points which must be improved to have better results. In this thesis Li/Li$^+$ ion doped carbon nano structures are investigated theoretically in order to contribute to the lithium battery technology. The present studied carbon nano structures are the fullerenes, single-walled carbon nanotubes, pristine and defected (Stone-Wales and mono-vacancy defected) carbon nanocapsules. The Li/Li$^+$ interactions with these nano structures have been investigated using semi-empirical molecular orbital method at PM3 level, density functional theory method with B3LYP exchange-correlation functional using 3-21G or 6-31G basis sets. Furthermore, the systems have been investigated by molecular dynamics simulations in which Tersoff potential and an empirical many-body potential have been used to define the various interactions. In this thesis the optimized geometries, thermodynamical quantities, interfrontier molecular orbital eigenvalues and dipole moments of the studied systems have been reported.

Keywords: Carbon nanocage structures, density functional theory, molecular-dynamics simulations.

ÖZ

NANOSİSTEMLERDE LİTYUM-KARBON ETKİLEŞMELERİ: MOLEKÜLER DİNAMİK MODELLEMELER VE YOĞUNLUK FONKSİYONU TEOREMİ HESAPLARI

Peköz, Rengin
Doktora, Fizik Bölümü
Tez Yöneticisi : Prof. Dr. Şakir Erkoç

Eylül 2008, 88 sayfa

Tek duvarlı karbon nanotüpler elektronik, manyetik, kimyasal ve mekanik özelliklerinden dolayı ilgi çekiyorlar. Bundan başka, ideal nano-kaplar oldukları için, dıştan ve içten emilim özellikleri Li/Li$^+$ iyon pilleri olarak kullanılmalarını sağlar. Pillerin kapasite, hız yeteneği ve devir ömrü daha iyi sonuçlar elde etmek için geliştirilmesi gereken noktalardır. Bu tezde Li/Li$^+$ iyon katkılanmış karbon nano yapılar teorik olarak lityum pil teknolojisine katkıda bulunmak üzere incelenmiştir. Çalışılan nano yapılar fullerenler, tek duvarlı karbon nanotüpler, hasarsız ve hatalı (Stone-Wales ve tek-boşluklu hatalı) karbon nanokapsüllerdir. Bu sistemler ile Li/Li$^+$ iyon etkileşmeleri yarı-empirik moleküler orbital metodunda PM3 seviyesinde, yoğunluk fonksiyoneli teoremi metodunda B3LYP değişim-korelasyon fonksiyoneli ile 3-21G ya da 6-31G temel setleri kullanılarak incelendi. Bundan başka, sistemler molekül dinamik modellemeler ile de incelendi. Bu modellemelerde değişik etkileşmeler için Tersoff potansiyeli ile deneysel çok-parçacıklı sistemler için geliştirilmiş potansiyel kullanılmıştır. Bu tezde çalışılan sistemlerin optimize edilmiş geometriler, termodinamik nicelikler, içsınır moleküler orbital enerji değerleri ve dipol momentleri verilmiştir.

Anahtar Kelimeler: Karbon nanokafes yapılar, yoğunluk fonksiyonel kuramı, molekül-dinamiği modellemeleri

To my dear family

ACKNOWLEDGMENTS

I would like to express my deepest gratitude and thanks to my supervisor, Prof. Dr. Şakir Erkoç, for his patient guidance, encouragement, being accessible and willing to help me all the time.

A very special thanks goes out to Dr. Emre Taşçı and Dr. Barış Malcıoğlu, for their help, friendship, smiling faces and support. I had really nice time during the long hours in the lab and I felt if we were a family.

I am thankful to Dr. Hande Üstünel for her friendship, valuable assistance in the researches, and for her willing to help me.

I do not know how to express my gratitude to my dear friends, Özge Amutkan, Emel Kilit, and Revan Çoban. They have been always with me whenever I needed. Thank you for your extensive and continuous moral support, understanding me without judging and having heart-to-hearth talks. My sincere thanks are also for Başak Aldemir, Yasemin Saraç, Nazım Dugan, Ayşe Çağıl and Hüseyin Dağ for being there whenever I needed them.

I am really thankful to Vedat Tanrıverdi for his friendship for more than 10 years, unforgettable chuckles, great patience and tolerance to my anxious times and being a great officemate.

I would like to thank Mustafa Çimşit, whose memories have been always with me and still achieving both to laugh and cry me.

I also thank to the members of FSK especially to Süleyman Aslan, Mete Gülhan

and Cem Susuz for their lovely friendship and smiling faces. They made me feel happy and not feeling alone in some parts of my life.

A special thanks goes out to Altuğ Özpineci, for being my friend, for a while being the source of ease, and helping me for many things.

Finally and the most importantly I would like to thank my family for the moral support and patience during my study and through my entire life.

Finally, I would like to thank Scientific and Technological Research Council of Turkey (TUBITAK) for the financial support during my research and I would like to thank METU for partial support through the Project METU-BAP-2006-07-02-00-01 .

TABLE OF CONTENTS

ABSTRACT iv

ÖZ vi

ACKNOWLEDGMENTS ix

TABLE OF CONTENTS xi

LIST OF TABLES xiii

LIST OF FIGURES xvii

CHAPTERS

1 INTRODUCTION 1

2 THEORETICAL BACKGROUND ON THE COMPUTATIONAL TOOLS 5

2.1 Computational Methods 5

2.1.1 Molecular Mechanics 6

2.1.1.1 Bond stretching and bond angle bending 6

2.1.1.2 Bond dipoles 7

2.1.1.3 Dihedral motion 8

2.1.1.4 van der Waals interaction 8

2.1.2 Semi-empirical Methods 9

2.1.2.1 Charge and spin multiplicity 10

2.1.2.2 Spin pairing 11

2.1.2.3 Convergence criteria 11

2.1.3 The Hartree, Hartree-Fock and Hartree-Fock-Roothaan Methods for the Many-Particle Schrödinger Equations 12

2.1.4 Density Functional Theory 16

2.1.4.1 Basis sets 19

2.1.5 Geometry Optimizations 21

2.1.5.1 Steepest (gradient) descent method . . . 22

2.1.5.2 Conjugate gradient method with Polak-Ribiere algorithm 22

2.1.6 Molecular Dynamics 24

2.2 Properties of Carbon Nano Structures 28

3 Li/Li$^+$ ION DOPED CARBON NANOSYSTEMS 32

3.1 Li/Li$^+$ Ion Interaction with Fullerenes and Single Walled Carbon Nanotubes 32

3.2 Li/Li$^+$ Ion Doped Carbon Nanocapsules Studied with Semi-Empirical MO Method at PM3 Level 36

3.3 The Structural and Electronic Properties of Stone-Wales and Mono-Vacancy Defected Carbon Nanocapsules 41

3.4 nLi/nLi$^+$ Ion (n=1-4) Doped Defect-Free Carbon Nanocapsules Studied with DFT method 52

3.5 Structural and Electronic Properties of nLi/nLi$^+$ ion (n=1-3) Doped Vacancy Defected Carbon Nanocapsules 57

3.6 Structural and Electronic Properties of nLi/nLi$^+$ ion (n=1-4) Doped Stone-Wales Defected Carbon Nanocapsules 67

4 CONCLUSION 76

REFERENCES 79

LIST OF TABLES

TABLES

Table 2.1 Parameters of the pair potential energy functions (energy is in eV and distance is in Å). 26

Table 3.1 Calculated total potential energy (in eV) of the endohedral doped Li/Li$^+$ ion systems. 33

Table 3.2 Calculated total potential energy (in eV) of the exohedral doped Li/Li$^+$ ion systems. 34

Table 3.3 Molecular properties of the Li/Li$^+$ ion doped C(5,5) and C(9,0) nanocapsule systems. 37

Table 3.4 Calculated energy values (in kcal/mol) of the Li/Li$^+$ ion doped C(5,5) and C(9,0) nanocapsule systems. 37

Table 3.5 Calculated molecular orbital eigenvalues (in eV), dipole moments (in Debyes) and the accumulated charges on the Li/Li$^+$ ion for the C(5,5) and C(9,0) nanocapsule systems. 38

Table 3.6 Calculated energy values (in kcal/mol) of C(5,5) capsule systems (TE: total energy, BE: binding energy, IAE: isolated atomic energy, EE: electronic energy, CCI: core-core interaction, and HOF: heat of formation). 43

Table 3.7 Calculated energy values (in kcal/mol) of C(9,0) capsule systems (TE: total energy, BE: binding energy, IAE: isolated atomic energy, EE: electronic energy, CCI: core-core interaction, and HOF: heat of formation). 43

Table 3.8 Calculated molecular orbital energy eigenvalues (in a.u.) and the dipole moments (μ) (in Debyes) of C(5,5) capsule systems. 45

Table 3.9 Calculated molecular orbital energy eigenvalues (in a.u.) and the dipole moments (μ) (in Debyes) of C(9,0) capsule systems. 45

Table 3.10 Calculated total energy values (in a.u.) of the C(5,5) and C(9,0) systems. MD results (in eV) are given in paranthesis. 51

Table 3.11 Defect formation energies per atom (in eV/atom) of the C(5,5) and C(9,0) systems. 51

Table 3.12 Calculated energy values (in kcal/mol)(TE: total energy, BE: binding energy, IAE: isolated atomic energy, EE: electronic energy, CCI: core-core interaction, and HOF: heat of formation) of undoped and nLi and nLi$^+$ ion doped pristine C(5,5) optimized systems, where n=1-4 (single point/PM3 results). 53

Table 3.13 Calculated energy values (in kcal/mol)(TE: total energy, BE: binding energy, IAE: isolated atomic energy, EE: electronic energy, CCI: core-core interaction, and HOF: heat of formation) of undoped and nLi and nLi$^+$ ion doped pristine C(9,0) optimized systems, where n=1-4 (single point/PM3 results). 53

Table 3.14 Calculated HOMO, LUMO energies (in a.u.), HOMO-LUMO gap (E_g) energies (in eV) and dipole moments (μ, in Debyes) of undoped and nLi/nLi$^+$ ion doped pristine C(5,5) systems (n=1-4). (DFT B3LYP/6-31G results.) 54

Table 3.15 Calculated HOMO, LUMO energies (in a.u.), HOMO-LUMO gap (E_g) energies (in eV) and dipole moments (μ, in Debyes) of undoped and nLi/nLi$^+$ ion doped pristine C(9,0) systems (n=1-4). (DFT B3LYP/6-31G results.) 54

Table 3.16 Total energy values (in au) of the pristine C(5,5) and C(9,0) systems undoped and doped with nLi/nLi$^+$ ion (n=1-4) by applying B3LYP level of DFT calculation using 6-31G basis set. 57

Table 3.17 Binding energy values (E_b) per Li/Li$^+$ ion (in eV/Li) of the pristine C(5,5) and C(9,0) systems doped with nLi/nLi$^+$ ion (n=1-4) by applying B3LYP level of DFT calculation using 6-31G basis set. (Li-Li interactions are not considered; from Eq. 3.2.) 58

Table 3.18 Binding energy values (E_b') per Li/Li$^+$ ion (in eV/Li) of the pristine C(5,5) and C(9,0) systems doped with nLi/nLi$^+$ ion (n=2-4) by applying B3LYP level of DFT calculation using 6-31G basis set. (Li-Li interactions are considered; from Eq. 3.3.) 58

Table 3.19 Calculated energy values (in kcal/mol)(TE: total energy, BE: binding energy, IAE: isolated atomic energy, EE: electronic energy, CCI: core-core interaction, and HOF: heat of formation) of nLi and nLi$^+$ ion doped vacancy defected C(5,5) and C(9,0) optimized systems, where n=1-3 (single point/PM3 results). 61

Table 3.20 Calculated HOMO, LUMO energies (in a.u.), HOMO-LUMO gap (E_g) energies (in eV) and dipole moments (in Debyes) of the nLi/nLi$^+$ ion doped C(5,5) vacancy defected systems (n=1-3). (DFT B3LYP/6-31G results.) 62

Table 3.21 Calculated HOMO, LUMO energies (in a.u.) and HOMO-LUMO gap (E_g) energies (in eV) and dipole moments (in Debyes) of the nLi/nLi$^+$ ion doped C(9,0) vacancy defected systems (n=1-3). (DFT B3LYP/6-31G results.) 62

Table 3.22 Total energy values (in au) of the C(5,5) and C(9,0) systems doped with nLi/nLi$^+$ ion (n=1-3) by applying B3LYP level of DFT calculation using 6-31G basis set. MD results (in eV) are given in parenthesis. 65

Table 3.23 Binding energy values per Li/Li$^+$ ion (in eV/Li) of the C(5,5) and C(9,0) systems doped with nLi/nLi$^+$ ion (n=1-3) by applying B3LYP level of DFT calculation using 6-31G basis set. (Li-Li interactions are not considered; from Eq. 3.2) 66

Table 3.24 Binding energy values per Li/Li$^+$ ion (in eV/Li) of the C(5,5) and C(9,0) systems doped with nLi/nLi$^+$ ion (n=2,3) by applying B3LYP level of DFT calculation using 6-31G basis set. (Li-Li interactions are considered; from Eq. 3.3) 67

Table 3.25 Calculated energy values (in kcal/mol)(TE: total energy, BE: binding energy, IAE: isolated atomic energy, EE: electronic energy, CCI: core-core interaction, and HOF: heat of formation) of undoped and nLi and nLi^+ ion doped C(5,5) SW-defected optimized systems, where n=1-4 (single point/PM3 results). 68

Table 3.26 Calculated energy values (in kcal/mol)(TE: total energy, BE: binding energy, IAE: isolated atomic energy, EE: electronic energy, CCI: core-core interaction, and HOF: heat of formation) of undoped and nLi and nLi^+ ion doped C(9,0) SW-defected optimized systems, where n=1-4 (single point/PM3 results). 68

Table 3.27 Calculated HOMO, LUMO energies (in a.u.), HOMO-LUMO gap (E_g) energies (in eV) and dipole moments (μ in Debyes) of undoped and nLi/nLi^+ ion doped C(5,5) SW-defected systems (n=1-4). (DFT B3LYP/6-31G results. 69

Table 3.28 Calculated HOMO, LUMO energies (in a.u.), HOMO-LUMO gap (E_g) energies (in eV) and dipole moments (μ in Debyes) of undoped and nLi/nLi^+ ion doped C(9,0) SW-defected systems (n=1-4). (DFT B3LYP/6-31G results. 69

Table 3.29 Total energy values (in au) of the C(5,5) and C(9,0) SW-defected systems undoped and doped with nLi/nLi^+ ion (n=1-4) by applying B3LYP level of DFT calculation using 6-31G basis set. 71

Table 3.30 Binding energy values (E_b) per Li/Li^+ ion (in eV/Li) of the C(5,5) and C(9,0) SW-defected systems doped with nLi/nLi^+ ion (n=1-4) by applying B3LYP level of DFT calculation using 6-31G basis set. (Li-Li interactions are not considered; from Eq. 3.2.) 73

Table 3.31 Binding energy values (E_b') per Li/Li^+ ion (in eV/Li) of the C(5,5) and C(9,0) SW-defected systems doped with nLi/nLi^+ ion (n=2-4) by applying B3LYP level of DFT calculation using 6-31G basis set. (Li-Li interactions are considered; from Eq. 3.3.) 73

LIST OF FIGURES

FIGURES

Figure 2.1 Bond dipoles. 8

Figure 2.2 Dihedral motions. 9

Figure 2.3 The van der Waals (6-12) and hydrogen bond (10-12) potentials are graphed. The AMBER force field uses the (10-12) potential. 10

Figure 2.4 The steepest descent method searching for a minimum. 23

Figure 2.5 (a) The unit cell and (b) Brillouin zone of graphene are shown as the dotted rhombus and the shaded hexagon, respectively. 28

Figure 2.6 The conventional model describing a CNT formed from a graphene sheet. 30

Figure 2.7 The armchair, zigzag and chiral nanotube a)(5,5), b)(9,0), c)(10,5) nanotube. 31

Figure 3.1 The optimized geometries for the endohedral Li^+ ion doped C_{20} and C_{60}. (Similar geometries are found for Li case.) 34

Figure 3.2 The optimized geometries for Li^+ ion confined within C(4,4), C(5,5), C(7,0), and C(8,0) SWCNTs. (Similar geometries are found for Li case.) . 35

Figure 3.3 The pair potential profiles for C-Li, C-Li^+ ion, and Li-Li. 35

Figure 3.4 3D plots of HOMO, LUMO, charge density (CD), and electrostatic potential (EP) for the Li@C(5,5) capsule. 39

Figure 3.5 3D plots of HOMO, LUMO, charge density (CD), and electrostatic potential (EP) for the Li^+@C(5,5) capsule. 40

Figure 3.6 3D plots of HOMO, LUMO, charge density (CD), and electrostatic potential (EP) for the Li@C(9,0) capsule. 40

Figure 3.7 3D plots of HOMO, LUMO, charge density (CD), and electrostatic potential (EP) for the Li^+@C(9,0) capsule. 41

Figure 3.8 3D plots of spin densities of Li@C(5,5) and Li@C(9,0) systems. . . 41

Figure 3.9 Stone-Wales and mono-vacancy defects for C(5,5) and C(9,0) nanocapsules before the optimizations. 44

Figure 3.10 3D plots of charge distribution by color, total charge density, HOMO, and LUMO for the SW defected C(5,5) capsule. 46

Figure 3.11 3D plots of charge distribution by color, total charge density, HOMO, and LUMO for the SW defected C(9,0) capsule. 46

Figure 3.12 3D plots of charge distribution by color, total charge density, HOMO, and LUMO for the C(5,5) capsule with 0-type vacancy defect. 47

Figure 3.13 3D plots of charge distribution by color, total charge density, HOMO, and LUMO for the C(9,0) capsule with 0-type vacancy defect. 47

Figure 3.14 3D plots of charge distribution by color, total charge density, HOMO, and LUMO for the C(5,5) capsule with A-type vacancy defect. 48

Figure 3.15 3D plots of charge distribution by color, total charge density, HOMO, and LUMO for the C(9,0) capsule with A-type vacancy defect. 48

Figure 3.16 3D plots of charge distribution by color, total charge density, HOMO, and LUMO for the C(5,5) capsule with B-type vacancy defect. 49

Figure 3.17 3D plots of charge distribution by color, total charge density, HOMO, and LUMO for the C(9,0) capsule with B-type vacancy defect. 49

Figure 3.18 3D plots of charge distribution by color, total charge density, HOMO, and LUMO for the C(5,5) capsule with C-type vacancy defect. 50

Figure 3.19 3D plots of charge distribution by color, total charge density, HOMO, and LUMO for the C(9,0) capsule with C-type vacancy defect. 50

Figure 3.20 The HOMO-LUMO gap (E_g) energy versus the number of Li/Li^+ ion in the pristine C(5,5) (left) and C(9,0) (right) capsules. (Squares are for the lithium ions and triangles are for the lithium atoms.) 55

Figure 3.21 3D plots of charge distribution by color, total charge density, HOMO, and LUMO for the defect-free undoped C(5,5) (upper panel) and C(9,0) (lower panel) capsule. 56

Figure 3.22 3D plots of charge distribution by color (a), HOMO (b), and LUMO (c) for the nLi@C(5,5) pristine capsules (n=1-4). 57

Figure 3.23 3D plots of charge distribution by color (a), HOMO (b), and LUMO (c) for the nLi$^+$@C(5,5) pristine capsules (n=1-4). 58

Figure 3.24 3D plots of charge distribution by color (a), HOMO (b), and LUMO (c) for the nLi@C(9,0) pristine capsules (n=1-4). 59

Figure 3.25 3D plots of charge distribution by color (a), HOMO (b), and LUMO (c) for the nLi$^+$@C(9,0) pristine capsules (n=1-4). 59

Figure 3.26 The HOMO-LUMO gap (E_g) energy versus the number of Li/Li$^+$ ion in the vacancy defected C(5,5) (left) and C(9,0) (right) capsules. (Squares are for the lithium ions and triangles are for the lithium atoms.) 63

Figure 3.27 3D plots of charge distribution by color (a), HOMO (b), and LUMO (c) for the nLi atom (n=1-3) doped C(5,5) VD capsules. 64

Figure 3.28 3D plots of charge distribution by color (a), HOMO (b), and LUMO (c) for the nLi$^+$ ion (n=1-3) doped C(5,5) VD capsules. 64

Figure 3.29 3D plots of charge distribution by color (a), HOMO (b), and LUMO (c) for the nLi atom (n=1-3) doped C(9,0) VD capsules. 65

Figure 3.30 3D plots of charge distribution by color (a), HOMO (b), and LUMO (c) for the nLi$^+$ ion (n=1-3) doped C(9,0) VD capsules. 66

Figure 3.31 The HOMO-LUMO gap (E_g) energy versus the number of Li/Li$^+$ ion in the SW-defected C(5,5) (left) and C(9,0) (right) capsules. (Squares are for the lithium ions and triangles are for the lithium atoms.) 70

Figure 3.32 3D plots of charge distribution by color (a), HOMO (b), and LUMO (c) for the C(5,5) (upper panel) and C(9,0) pristine (lower panel) undoped SW-defected capsules. 71

Figure 3.33 3D plots of charge distribution by color (a), HOMO (b), and LUMO (c) for the nLi@C(5,5) SW-defected capsules (n=1-4). 72

Figure 3.34 3D plots of charge distribution by color (a), HOMO (b), and LUMO (c) for the nLi$^+$@C(5,5) SW-defected capsules (n=1-4). 73

Figure 3.35 3D plots of charge distribution by color (a), HOMO (b), and LUMO (c) for the nLi@C(9,0) SW-defected capsules (n=1-4). 74

Figure 3.36 3D plots of charge distribution by color (a), HOMO (b), and LUMO (c) for the nLi$^+$@C(9,0) SW-defected capsules (n=1-4). 75

Figure 3.37 Fully relaxed structures of the SW-defected C(5,5) and C(9,0) capsules. The compared C-C bond lengths are represented as C1-C2 75

CHAPTER 1

INTRODUCTION

Since their discoveries by Kroto [1] and Iijima [2], fullerenes and carbon nanotubes (CNTs) are attracting more and more interest among scientists and engineers because of their electronic, magnetic [3], chemical [4], high-mechanical strength and flexibility properties. Although many compounds from the fullerene class have been discovered, the physical and chemical properties of C_{60} molecule such as being the most stable one at room temperature, have been preferred to study because of its suitability to large scale synthesis [5] and its ability to be endohedrally doping [6,7]. Furthermore, endohedral metal atom doped C_{20} molecule has been investigated theoretically [8]. The space between and the interiors of the nanotubes are ideal nano-containers for intercalation of foreign atoms and molecules [9-15]. The adsorption and absorption properties of these carbon structures provide applications such as hydrogen storage [16,17], nanocatalyst [18], gas sensors [19], thermionic metal supplies [20], one-dimensional nano junction and superconductors [21], and power devices such as Li and Li^+ ion batteries [22-27].

The anode, cathode and electrolyte materials used in a battery affect the voltage, capacity, life of the battery and the safety. The lithium batteries have lithium metal or lithium compounds as the anode material. For the lithium-ion batteries, graphite has been the most popular material for the anode [28], [29]. Lithium can migrate from anode to cathode (in the discharge process) and from cathode the anode (in the charge process). The insertion/intercalation (extraction/deintercalation) is the lithium movement into (out of) the anode or cathode. Under optimal conditions lithium intercalates into graphite to form LiC_6 and the use of graphite instead of metallic lithium causes a capacity reduction from 3860 mAh/g to 372 mAh/g [30]. The performance of these batteries depends on the Li/C ratio and the mobility of the lithium. Higher energy density is obtained when the Li/C ratio is increased inside the host material.

Recently, CNTs have been thought of as promising candidates as anode material of the batteries. The lithium ions can intercalate both to the channels between the CNTs and to the interior of the CNTs themselves which results in a higher energy density. In the experiments carried out by Gao et al. [31], the intercalation density reached up to $Li_{2.6}C_6$ after ball milling process. Moreover, it was found that when the single-walled CNTs (SWCNTs) were chemically etched to short segments it was observed that the specific lithium capacity increased from LiC_6 to LiC_3 [24]. These improvements have attracted many researchers to investigate deeply the SWCNTs for the lithium-ion batteries both experimentally and theoretically. The theoretical investigations performed by Garau et al. [32] were basically on the possibilities of Li^+ ion insertion through the open ends of SWCNTs having different diameters. The first-principles calculations carried out by Zhao et al. [33] explored the potential energy profiles of lithium confined inside SWCNTs and they found that lithium had high mobility around the tube axis. The first principles calculations of Li/Li^+ ion adsorption on the side walls of CNTs performed by Udomvech et al. [34] and found that the intercalated Li/Li^+ ion preferred to localize near the CNT side wall instead of at the tubule length and the usage of larger diameter CNTs would have a drawback compared to the small diameter tubes. Zhao et al. [35] investigated the diffusion of lithium on the exteriors and the interiors of SWCNTs and they found that lithium could got adsorbed on both the interior and the exterior surfaces of the tubes.

As they once thought to be, experiments showed that CNTs are not perfect (defect-free) in reality [36,37]. Defects can appear during nanotube growth or can be created by external actions. These defects can be classified into three groups: topological (introduction of ring types other than hexagons), rehybridization (ability of carbon atom to hybridize between sp^2 and sp^3), and incomplete bonding defects [38]. The defect types are Stone-Wales (SW) defects, single or multiple vacancies, adatom, impurity, and dislocation defects. It is a known fact that the existence of defects affects the mechanical, electrical and thermal properties of CNTs. It has been shown that the atomic vacancies can lower the tensile strength by up to 85% [39]. Moreover, the conductivity changes through the defective region of the CNT [40]. Moreover, single monoatomic vacancies induce magnetic properties and defects can cause the thermal conductivity to reduce. These defects have an important role in the diffusion process of lithium ions through the nanotubes [41]. An ab initio study of Meunier et al. [30] investigated the lithium diffusion into different CNTs through the defective rings and found that while lithium ions could enter the tubes through the topological defects which are more than nine-sided rings, the lithium could not diffuse through the side walls of the tubes. Nishidate et al. [42] studied the energetics of lithium ion adsorption on SWCNTs and the change in total average voltage caused by the lithium adsorption on the possible sides of the defective tubes using density functional theory (DFT) calculations and found that the adsorption of lithium on SWCNTs was very feasible. Another theoretical investigation was performed by Kar et al. [25] to explore the Li^+ ion insertion through the side-wall or through the cap region of the CNTs and it was found that the outside position of lithium ions were more favorable and as the size of the rings increased insertion of lithium ions were easier.

As can be seen from the above paragraphs, in the literature there are many experimental and theoretical investigations related to the Li/Li^+ ion interactions with CNTs. However, up to our knowledge, the defect-free and defected carbon nanocapsule (CNC) systems with Li/Li^+ doping have not been investigated. The purpose of this thesis is to investigate these kind of systems in detail and to do our best to fill the blanks in the literature about these topics.

This thesis is divided into four chapters. In the second chapter, the theoretical methods used in the investigations of the studied systems have been explained. In the third chapter, a brief introduction to the systems and the results of the studies will be presented. In the last chapter, a summary of this thesis will be given.

CHAPTER 2

THEORETICAL BACKGROUND ON THE COMPUTATIONAL TOOLS

2.1 Computational Methods

In this thesis Molecular Mechanics, Quantum Mechanics Calculations and Molecular Dynamics Simulations are performed. Therefore, this section is divided into three subsections. Molecular mechanics is the simplest method among the others since it uses the equations of vibrational spectroscopy in order to investigate the potential energy surfaces and the structural properties of molecules. Quantum mechanics methods include semi-empirical, ab initio and density functional theory. In this thesis, since ab initio calculations have not been used, no theoretical background for this method will be presented. Semi-empirical methods make approximations to solve the Schrödinger equation by replacing the mathematical expressions with experimental values. On the other hand, density functional theory solves the Schrödinger equation for the electron density not for a wavefunction.

The main advantage of using molecular mechanics or semi-empirical methods over density functional theory is that these methods are very fast which gains more importance as the system size increases. Furthermore, if the system is well-parameterized the calculation results are found to be more closer to experiment than small basis set used ab initio or density functional theories. The drawback of the molecular mechanics is that the calculations require parameters which is time-consuming to develop.

2.1.1 Molecular Mechanics

In molecular mechanics, a force field defines the functional form of the potential energy and the set of parameters for each type of atom in the system. The molecular mechanics methods have separate functional forms such as MM+ which is the extension of MM2 [43, 44], AMBER [45], OPLS [46], and BIO+ [47]. In this thesis, MM+ is used for the optimization purposes because of the fact that it works best for thermodynamical and structural properties of nonpolar molecules. In general, a force field includes several interaction terms such as bond stretching, bond angle bending, bond dipoles, dihedral motions, and van der Waals interactions.

2.1.1.1 Bond stretching and bond angle bending

The atoms of a molecule may be thought as the collection of mutually independent springs. Bond stretching is related to the deformation of a bond from its equilibrium bond length. At very large deformations a Morse potential can be used instead of a harmonic potential. However, because of the requirement of excessive amounts of time, they are not preferred. For small displacements from equilibrium a harmonic potential is given as:

$$V_{bond} = \sum_{bonds} k_r (r - r_0)^2 \tag{2.1}$$

where k_r is the stretch force constant and r_0 is the equilibrium distance.

MM+ uses the following formula:

$$V_{bond} = 142.88 \sum_{bonds} \frac{1}{2} K_r (r - r_0)^2 \left[1 - switch(a_1, a_2, a_3) CS (r - r_0)\right] \qquad (2.2)$$

where $a_1 = r - r_0$, $a_2 = -\frac{1}{3}CS$, $a_3 = -\frac{4}{3}CS$, and CS is set to -2.0 and the cutoff function (switch) is defined as

$$\begin{aligned} switch(x,a,b) &= 1 \quad x \leq a \\ switch(x,a,b) &= 0 \quad x \geq b \\ switch(x,a,b) &= \frac{(b-x)^2(b+2x-3a)}{(b-a)^3} \quad a < x < b. \end{aligned} \qquad (2.3)$$

The deformation of an angle from its "natural" value is associated to the bond angle bending. For small displacements from equilibrium the form of a harmonic potential is used:

$$V_{bond\ angle} = \sum_{angles} k_\theta (\theta - \theta_0) \qquad (2.4)$$

where k_θ is the bending force constant.

MM+ includes a sextic angle bending term for the angle bending which has the following form:

$$V_{bond\ angle} = 0.044 \sum_{angles} \frac{1}{2} K_\theta (\theta - \theta_0)^2 [1 + SF(\theta - \theta_0)^4] \qquad (2.5)$$

where the SF is the scale factor and the default value is 7.0×10^{-8}.

2.1.1.2 Bond dipoles

Electrostatic charge-charge interactions or definition of a set of atomic charges are not used in MM+ calculations. The electrostatic contribution is obtained from a set of bond dipole moments which are associated with polar bonds. The center of the dipole is the midpoint of the bond and the two dipoles μ_i and μ_j

are separated by R$_{ij}$ (see Fig. 2.1). The dipole interaction potential is defined as [43]:

$$V_{dipole} = 14.39\varepsilon \sum_{ij \in polar\ bonds} \mu_i \mu_j [\frac{\cos\chi - 3\cos\alpha_i \cos\alpha_j}{R_{ij}^3}] \tag{2.6}$$

where ε is the dielectric constant, χ is the angle between the two dipole vectors, and α_i and α_j are the angles that the two dipole vectors make with the R$_{ij}$ vector. Bond dipoles are given in units of Debyes.

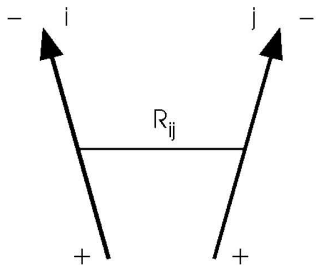

Figure 2.1: Bond dipoles.

2.1.1.3 Dihedral motion

The dihedral potential in MM+ is given in the following equation [43]:

$$V_{dihedrals} = \sum_i \frac{V_1}{2}(1 + \cos\phi_i) + \frac{V_2}{2}(1 - \cos 2\phi_i) + \frac{V_3}{2}(1 + 3\cos\phi_i) \tag{2.7}$$

where the values of V$_1$, V$_2$, and V$_3$ are in kcal/mol and ϕ_i is the phase angle. The dihedral angle (torsional) rotation arises from the bonding of 4 atoms with 2 planes and shown in Fig. 2.2.

2.1.1.4 van der Waals interaction

The total interaction potential describes the sum of the repulsive and attractive forces for a pair of atoms. Lennard-Jones potential (see Fig. 2.3) is the most

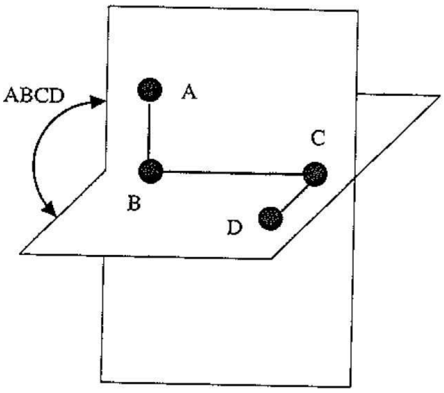

Figure 2.2: Dihedral motions.

widely used interaction among the force fields. However, an exponential repulsion term with an attractive 1/R^6 dispersion interaction is combined. The van der Waals interaction potential is the following:

$$V_{vanderWaals} = \sum_{ij \in vdW} \varepsilon_{ij}(2.90 \times 10^5 e^{-12.5\rho_{ij}} - 2.25\rho_{ij}^{-6}) \qquad (2.8)$$

where r$_i$ (van der Waals radii for the atoms) and ε_{ij} (hardness parameter determining the depth of the attractive well) are the basic parameters. The parameters for a pair are calculated from individual atom parameters, such as:

$$\begin{aligned} r_{ij}^* &= r_i^* + r_j^* \\ \varepsilon_{ij} &= \sqrt{\varepsilon_i \varepsilon_j} \\ \rho_{ij} &= \frac{R_{ij}}{r_{ij}^*}. \end{aligned} \qquad (2.9)$$

2.1.2 Semi-empirical Methods

Semi-empirical calculations use many parameters related to the type of the atom. The carefully constructed quantum mechanical formulation is combined with these empirical parameters which are compared with the experiment. HyperChem package supports ten semi-empirical self-consistent field (SCF) methods:

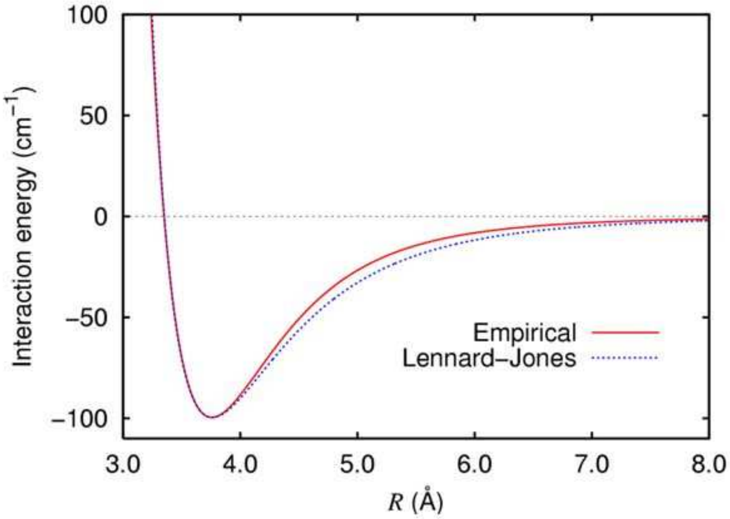

Figure 2.3: The van der Waals (6-12) and hydrogen bond (10-12) potentials are graphed. The AMBER force field uses the (10-12) potential.

complete neglect of differential overlap (CNDO), intermediate neglect of differential overlap (INDO), modified intermediate neglect of differential overlap (version 3, use of d-orbitals) (MNDO(/3/d)), Austin model which is a modification of MNDO (AM1), PM3 (parametric model number 3) is a reparameterization of AM1 and based on the neglect of diatomic differential overlap approximation, ZINDO/1 and ZINDO/S are modified version of INDO, and total neglect of differential overlap (TNDO). In this thesis, PM3 calculations have been performed using both HyperChem and Gaussian03 [48] packages. In order to run a semi-empirical calculation certain options are needed which take part on the option dialog boxes on the Setup menu of the package programs. In the following subsection, some of the options will be explained briefly.

2.1.2.1 Charge and spin multiplicity

The extra (net) charge given to the system specifies whether the system is a neutral one, cation (positively charged), or anion (negatively charged) system.

Multiplicity (total spin state) is calculated as $2S + 1$, i.e., the total number of unpaired electrons+1. Closed-shell systems have a multiplicity of one which means it is a singlet state. When the molecule has one unpaired electron it is a doublet with spin multiplicity two. In general, a system having two unpaired electrons has a multiplicity of three, however, in some cases it can be a singlet as in the case of a biradical.

2.1.2.2 Spin pairing

Unrestricted Hartree-Fock (UHF) and restricted Hartree-Fock (RHF) calculations are chosen according to the number of electrons in the system. While UHF can be used for both closed-shell (singlets) and open-shell (doublets and triplets) calculations, RHF is used for closed-shell calculations.

2.1.2.3 Convergence criteria

The precision of the self-consistent field (SCF) calculations is controlled by the convergence limit and the iteration limit. Convergence limit is the difference in total electronic energy between two successive SCF iterations. Iteration limit is the maximum number of iterations permitted to reach the desired convergence limit. The convergence limit in the single point energy calculations at PM3 level performed using HyperChem package is taken to be 0.001 kcal/mol. Moreover, the convergence on energy is set to 10^{-6} au. in the DFT calculations.

2.1.3 The Hartree, Hartree-Fock and Hartree-Fock-Roothaan Methods for the Many-Particle Schrödinger Equations

Hartree theory [49-51] is the fundamental to the traditional electronic structure methods the aim of which is to solve the electronic Schrödinger equation. It is an approximate method for obtaining the ground-state wavefunction and the ground-state energy. Hartree and the other methods developed from Hartree method are based on the many-electron wavefunction which depends on 3N coordinates of all N electrons. The methods are grounded on the idea that 3N-dimensional of N-electron wavefunction of the system can be approximated by a single Slater determinant [52]. With the help of the variational principle N coupled equations for the N spin orbitals can be derived and the solutions of these equations produces the Hartree-Fock wavefunction and the energy of the system can be obtained, which are the approximate results. In the following parts, the details of the Hartree and the other methods will be presented briefly. The interested readers are referred to Ref. [53] to follow up the material in greater depth.

The many-body Hamiltonian for the time-independent Schrödinger equation is in the following form:

$$\begin{aligned}\hat{H}_e &= \hat{T}_e + \hat{V}_{ne} + \hat{V}_{ee} + \hat{T}_n + \hat{V}_{nn} \\ &= -\frac{\hbar^2}{2m}\sum_{i=1}^{N}\nabla_i^2 - \sum_{i=1}^{N}\sum_{k=1}^{M}\frac{1}{4\pi\varepsilon_0}\frac{Z_k e^2}{|\vec{r}_i - \vec{R}_k|} + \frac{1}{2}\sum_{i_1\neq i_2=1}^{N}\frac{1}{4\pi\varepsilon_0}\frac{e^2}{|\vec{r}_{i_1} - \vec{r}_{i_2}|} \\ &- \frac{\hbar^2}{2M_k}\sum_{k=1}^{M}\nabla_k^2 + \sum_{k_1<k_2}^{M}\frac{1}{4\pi\varepsilon_0}\frac{Z_{k_1}Z_{k_2}e^2}{|\vec{R}_{k_1} - \vec{R}_{k_2}|}\end{aligned} \tag{2.10}$$

where H_e is the electronic Hamiltonian, N is the number of electrons, M is the number of nuclei, $\hat{T}_e$ is the kinetic energy of the electrons, $\hat{V}_{ne}$ is the nuclei-electron interaction, $\hat{V}_{ee}$ is the electron-electron interaction, $\hat{T}_n$ is the kinetic energy of the nuclei, and $\hat{V}_{nn}$ is the nuclei-nuclei interaction.

After constructing the many-body Hamiltonian, the first approach is the Born-

Oppenheimer approximation [54] which states that the electrons move much faster than the nuclei so that the motion of the nuclei can be separated from the motion of electrons. The advantage of using this approximation is that since it treats the nuclei as classical particles which contribute to the total energy and give an electrostatic field in which the electrons move, but their effects otherwise are ignored. When the Born-Oppenheimer approximation is taken into account, the atomic unit conventions ($\hbar$=m$_e$=e=1/4$\pi\varepsilon_0$=1) are applied and for the time being the final term ($\hat{V}_{nn}$) is taken to be a constant for the many-electron Hamiltonian, Eq. 2.10 takes the following form:

$$\hat{H}_e = -\frac{1}{2}\sum_{i=1}^{N}\nabla_i^2 - \sum_{i=1}^{N}\sum_{k=1}^{M}\frac{Z_k}{|\overrightarrow{r}_i - \overrightarrow{R}_k|} + \frac{1}{2}\sum_{i_1 \neq i_2 = 1}^{N}\frac{1}{|\overrightarrow{r}_{i_1} - \overrightarrow{r}_{i_2}|}. \tag{2.11}$$

The Hamiltonian operator contains one- and two-electron operators,

$$\begin{aligned} \hat{h}_1(\vec{r_i}) &= -\frac{1}{2}\nabla_i^2 - \sum_{k=1}^{M}\frac{Z_k}{|\overrightarrow{r}_i - \overrightarrow{R}_k|} \\ \hat{h}_2(\vec{r_i}, \vec{r_j}) &= \frac{1}{|\overrightarrow{r}_i - \overrightarrow{r}_j|} \\ \hat{H}_e &= \sum_{i=1}^{N}\hat{h}_1(\vec{r_i}) + \frac{1}{2}\sum_{i \neq j = 1}^{N}\hat{h}_2(\vec{r}_{i_1}, \vec{r}_{i_2}). \end{aligned} \tag{2.12}$$

An approximate solution to the electronic Schrödinger equation should be searched

$$\hat{H}_e\Psi_e = E_e\Psi_e \tag{2.13}$$

and the approximate solution to the wavefunction is

$$\Psi_e \simeq \Phi. \tag{2.14}$$

The important point is that the approximate wavefunction Φ should be so exact that the calculated observables are accurate enough. One of the ways of constructing the approximate wavefunction is the Hartree approximation which is a variational approach. The method is based on thinking of N electrons as occupying N different orbitals each of which can accommodate one electron. The approximate wavefunction can be written in terms of the individual orbitals (ϕ_i):

$$\Phi(\vec{x}_1, \vec{x}_2, ..., \vec{x}_N) = \phi_1(\vec{x}_1) \cdot \phi_2(\vec{x}_2) ... \phi_N(\vec{x}_N) \tag{2.15}$$

with the constraint that all the individual orbitals are orthonormal. The deficiency of the Hartee approximation is that it can not obey the Pauli-exclusion principle which satisfies the antisymmetry property. The antisymmetry conditions are satisfied by using the Hartree-Fock method [50, 55]. The required antisymmetric wavefunction is found to be in the following form:

$$\Phi(\vec{x}_1, \vec{x}_2, ..., \vec{x}_N) = \frac{1}{\sqrt{N!}} \begin{vmatrix} \phi_1(\vec{x}_1) & \phi_2(\vec{x}_1) & \cdots & \phi_N(\vec{x}_1) \\ \phi_1(\vec{x}_2) & \phi_2(\vec{x}_2) & \cdots & \phi_N(\vec{x}_2) \\ \vdots & \vdots & \ddots & \vdots \\ \phi_1(\vec{x}_N) & \phi_2(\vec{x}_1) & \cdots & \phi_N(\vec{x}_1) \end{vmatrix} \tag{2.16}$$

where the factor $1/\sqrt{N!}$ comes from the normalization. The determinant of Eq. 2.16 is the so-called Slater determinant. Hartree-Fock approximation depends on the approximation of independent particles like the Hartree approximation. Although Hartree-Fock method is not perfect, it includes a very important part of the physics of most of the systems.

The expectation value of the Hamiltonian for the Slater determinant is

$$E_{HF} = \langle \Phi | \hat{H}_e | \Phi \rangle = \sum_{i=1}^{N} \langle \phi_i | \hat{h}_1 | \phi_i \rangle + \frac{1}{2} \sum_{i,j=1}^{N} [\langle \phi_i \phi_j | \hat{h}_2 | \phi_i \phi_j \rangle - \langle \phi_j \phi_i | \hat{h}_2 | \phi_i \phi_j \rangle]. \tag{2.17}$$

While finding the approximate wavefunction, the variational principle plays an important role. It is crucial to notice that any change in the expectation value of the Hamiltonian because of an infinitesimal change in any of the orbitals ϕ_k should be zero, i.e.,

$$\phi_k(\vec{x}) \rightarrow \phi_k(\vec{x}) + \delta\phi_k(\vec{x}) \quad \Rightarrow \quad \delta\langle \Phi | \hat{H}_e | \Phi \rangle = 0. \tag{2.18}$$

Moreover, the set of orbitals ϕ_k should be orthogonal throughout the minimization process which should satisfy the following equation:

$$\delta F = \delta \left[\langle \Phi | \hat{H}_e | \Phi \rangle - \sum_{i,j} \lambda_{ij} (\langle \phi_i | \phi_j \rangle) - \delta_{ij} \right] = 0. \tag{2.19}$$

After calculating the changes of one- and two-body terms under an infinitesimal variation of one of the orbitals, ϕ_k, the minimization condition δF=0 requires the following in terms of integrals:

$$\hat{h}_1\phi_k(\vec{x}_1) + \sum_i \left\{ \int \phi_i^*(\vec{x}_2)\hat{h}_2[\phi_i(\vec{x}_2)\phi_k(\vec{x}_1)]d\vec{x}_2 - \int \phi_i^*(\vec{x}_2)\hat{h}_2[\phi_i(\vec{x}_1)\phi_k(\vec{x}_2)]d\vec{x}_2 \right\}$$
$$= \sum_i \lambda_{ki}\phi_i(\vec{x}_1). \tag{2.20}$$

The above equation (Eq. 2.20) can be rewritten using the orbital dependent operators, $\hat{J}_i$ and $\hat{K}_i$, respectively, as

$$\left[\hat{h}_1 + \sum_i(\hat{J}_i - \hat{K}_i)\right]\phi_k = \sum_i \lambda_{ki}\phi_i. \tag{2.21}$$

The Coulomb operators, $\hat{J}_i$, identify the classical electrostatic interactions between two charge distributions. The exchange operators is the result of the requirement that the N-electron wavefunction is to be antisymmetric in the case of interchanging two electrons. Then the Fock operator is defined as

$$\hat{F} = \hat{h}_1 + \sum_{i=1}^{N}(\hat{J}_i - \hat{K}_i) \tag{2.22}$$

with the Fock operator Eq. 2.22 takes the form

$$\hat{F}\phi_k = \sum_{i=1}^{N} \lambda_{ki}\phi_i \tag{2.23}$$

which has many solutions and each corresponding to the different sets of λ_{ki}. Then one can concentrate on the Lagrange multipliers obeying

$$\lambda_{ki} = \delta_{k,i}\varepsilon_k. \tag{2.24}$$

In this case, the Hartree-Fock equations become a traditional eigenvalue problem

$$\hat{F}\phi_k = \varepsilon_k\phi_k. \tag{2.25}$$

The Hartree-Fock equations resemble to the Schrödinger equation but the operator is a Fock operator not a Hamiltonian operator. For each k, there is an equivalent equation which is one for single particles and not for all N particles. The Hartree-Fock equations seem to be simple, however, when the precise forms of the operators are inserted they are used to have complicated integro-differential equations. In 1951 Roothaan [56] suggested an alternative way of finding an approximate wavefunction which is in the form of a Slater determinant. He proposed to expand the orbitals in a set of fixed basis functions, that is, instead of varying all orbitals in all points, only a finite variation was considered. In Roothaan's expansion, each orbital is written as

$$\psi_l(\vec{x}) = \sum_{p=1}^{N_b} \chi_p(\vec{x}) c_{pl}, \tag{2.26}$$

where the basis function χ and N$_b$ are chosen in advance and only the expansion coefficients c$_{pl}$ are varied.

When this expansion is substituted to the Hartree-Fock equation and the minimization is done, again an eigenvalue equation is obtained:

$$\sum_{m=1}^{N_b} \left\{ \langle \chi_p | \hat{h}_1 | \chi_m \rangle + \sum_{i=1}^{N} \sum_{n,q=1}^{N_b} c_{ni} c_{qi}^{*} [\langle \chi_p \chi_q | \hat{h}_2 | \chi_m \chi_n \rangle - \langle \chi_q \chi_p | \hat{h}_2 | \chi_m \chi_n \rangle] \right\} c_{ml}$$
$$= \varepsilon_l \sum_{m=1}^{N_b} \langle \chi_p | \chi_m \rangle c_{ml} \tag{2.27}$$

which is called as the Hartree-Fock-Roothaan equations and may be solved using standard matrix techniques in a self-consistent manner.

2.1.4 Density Functional Theory

DFT uses the electron density depending on 3 variables which is simpler than the wavefunction approach. The history of DFT starts with Hohenberg and Kohn theorem [57]. According to this theorem, the energy E of a molecular system is a universal functional (E depends not only on simple variables but also complicated function) of the electron density, i.e., E=E[ρ] and it is a ground state theory. They showed that when the ρ is exact, the ground state energy is exact, too. Hohenberg-Kohn theorems provide a formalistic proof to calculate any ground state property but they do not provide any practical scheme for calculating them from the electron density. In 1965, the approach of Kohn and Sham [58] provided the necessary information to calculate the ground state properties from the electron density.

As it is stated before, solving the many-particle Schrödinger equation for the ground state wavefunction even for small systems is a very difficult task. Instead of dealing with the electron wavefunction, electron density n($\vec{r}$) provides many simplifications to the problem. For a many-body system n($\vec{r}$) is found by calculating the expectation value of the single-particle density operator, i.e., $\hat{n}(\vec{r})$, for the many-body wavefunction. The single-particle density operator is given as:

$$\hat{n}(\vec{r}) = \sum_{i=1}^{N} \delta(\vec{r} - \vec{r}_i) \tag{2.28}$$

and the corresponding density is calculated as:

$$\begin{aligned} n(\vec{r}) &= \langle \Psi | \hat{n}(\vec{r}) | \Psi \rangle = \sum_{i=1}^{N} \int \delta(\vec{r} - \vec{r}_i) |\Psi(\vec{r}_1, ..., \vec{r}_N)|^2 d\vec{r}_1 ... \vec{r}_N \\ &= N \int |\Psi(\vec{r}, ..., \vec{r}_N)|^2 d\vec{r}_2 ... \vec{r}_N. \end{aligned} \tag{2.29}$$

Hohenberg and Kohn proved that the expression above for the electron density can be reversed, i.e., for a given ground state density n($\vec{r}$) it is possible to calculate the corresponding ground-state wavefunction $\Phi(\vec{r})$, which is equivalent to say that Φ is a unique functional of the density. As a result the other ground state observables are also functionals of n. The next procedure is to write the many-body Schrödinger equation in terms of the electron density. Remembering the Eq. 2.11, one can write the ground-state energy as a functional of density:

$$E_e = T[n(\vec{r})] + \int V_{ext}(\vec{r}) n(\vec{r}) d\vec{r} + \int V_C(\vec{r}) n(\vec{r}) d\vec{r} + E'_{xc}[n(\vec{r})] \tag{2.30}$$

where T is the kinetic energy term, V_C is the classical electrostatic (Coulomb) potential from the interaction of electrons which is found in the form:

$$V_C(\vec{r}_1) = \int \frac{\rho(\vec{r}_2)}{|\vec{r}_2 - \vec{r}_1|} d\vec{r}_2 \tag{2.31}$$

and V$_{ext}$ is the external field potential which is the electrostatic field generated by the nuclei having the following form:

$$V_{ext}(\vec{r}) = \sum_{k=1}^{M} \frac{-Z_k}{|\vec{R}_k - \vec{r}|}. \tag{2.32}$$

The last term in the Eq. 2.30, E'$_{xc}$ comes from the corrections made to the Hartree-Fock method and named as the exchange-correlation energy. It is the sum of the kinetic energy correction and the electron-electron energy correction. In the Hartree-Fock method kinetic energy was calculated as the sum of the kinetic energies of the Kohn-Sham orbitals however this is not the case for real systems. Moreover, since the electron-electron term is written in terms of the two-particle density not in terms of the single-particle density, it needs to be made an approximation which is the assumption of considering the two electrons completely uncorrelated so that the electron-electron term can be written in terms of the single-particle density and the correction to this term is called as the correlation energy. Exchange energy arises from the Pauli exclusion principle and the correlation energy comes from the repulsion between electrons. The explicit form of the Eq. 2.30 is written as

$$\begin{aligned} E_e &= \frac{1}{2}\sum_{n=1}^{N}\int d\vec{r}\phi_n^*(\vec{r})\nabla^2\phi_n(\vec{r})d\vec{r} + \int n(\vec{r})V_{ext}(\vec{r})d\vec{r} \\ &+ \frac{1}{2}\int\int d\vec{r}_1 d\vec{r}_2 \frac{n(\vec{r}_1)n(\vec{r}_2)}{|\vec{r}_1 - \vec{r}_2|} + E'_{xc}[n(\vec{r})]. \end{aligned} \tag{2.33}$$

Another problem with the DFT is that the exact functionals for exchange and correlation energies are not known except for the free electron gas and again approximations play an important role in the calculation of the physical quantities. Local density approximation (LDA) [59] is probably the most widely used one which models the exchange-correlation energy of an electron as if it is a homogeneous electron gas [58, 60]. According to LDA the electron density is constant in space, as a result of this V$_{xc}$ can be calculated as a function of the constant density. Vosko-Wilk-Nusair (VWN) [61], Perdew-Zunger 81 (PZ81) [62], Lee-Yang-Parr (LYP) [63], and Perdew-Wang (PW92) [64] functionals are some of the examples for the LDA. For the case of nonuniform charge densities, some deviations for the exchange-correlation energy can occur from the uniform case. The generalized gradient approximation (GGA) which uses the gradient of the charge density is used to correct this deviation. Some of the functionals of GGA type are developed by Becke [65], Perdew [66], Perdew-Wang [67], and Perdew-Burke-Ernzerhof (PBE-96) [68].

During the half of the 1980s, all DFT studies were carried out using one of the available LDA for the exchange and correlation effects. After the middle of the 1980s, different nonlocal or gradient approximations were developed. It was the beginning of 1990s that a new approach has been come out by Becke [69] which combines the Hartree-Fock and DFT for the exchange effects and uses DFT for the correlation effects. This approach is called as the hybrid method and it is based on the adiabatic connection approach [70]. The most popular hybrid methods are the Becke's 3 parameter functional where the non-local correlation is provided by the LYP expression (B3LYP) [71], the Becke's 3 parameter functional with Perdew 86 correlation functional (B3P86) [71, 72], and the Becke's 3 parameter functional with PW91 correlation functional (B3PW91) [66, 73].

2.1.4.1 Basis sets

As it is mentioned before single electron orbitals ϕ_k should be expanded in a set of pre-defined basis functions χ_i (Roothaan's theorem). If a reliable result is expected the choice of the basis function plays an important role in the calculations because they describe the shape of the orbitals in an atom and the positions of the electrons to the nucleus and to the each other. The pre-defined basis function $\chi(\vec{r})$ can be written as

$$\chi(\vec{r}) = R_{nl}(r)Y_{lm}(\theta, \phi) \tag{2.34}$$

where the function χ is assumed to belong to an atom placed at the origin and Y_{lm} is the spherical harmonic function. One should decide how to choose the radial parts of χ. There are orbitals used for this purpose which are the Slater-type [74], Gaussian-type, plane-wave, and augmented-wave orbitals [53]. In the following, since the Gaussian-type orbitals are used in this thesis, they will be explained briefly.

Gaussian-type orbitals (GTOs, Gaussian orbitals, or Gaussians) are the functions used as atomic orbitals to calculate the electron orbitals. These type of orbitals make easier the overlap and other integrals to solve than the Slater-type orbitals. GTOs have the following form:

$$\chi(\vec{r}) = \chi_{\vec{R},\alpha,n,l,m}(\vec{r}) = 2^{n+1}\frac{\alpha^{(2n+1)/4}}{[(2n-1)!!]^{1/2}(2\pi)^{1/4}}r^{n-1}e^{-\alpha r^2}Y_{lm}(\theta,\phi) \qquad (2.35)$$

where α is known as the exponent of the Gaussian function or an orbital coefficient. There are many basis sets composed of Gaussians. The smallest of these basis sets is called the minimal basis set. For a minimal basis set a single basis function is used on each atom. STO-nG [75, 76] (each STO is expanded in n Gaussians) and STO 4-31G (the core electrons are described by expanding the STOs in four Gaussians, the valance s and p orbitals are expanded in three and one Gaussians, respectively) are the examples to the minimal basis sets. Since minimal basis sets see all the electrons the same they are not used for research just for qualitative purposes.

Another basis set type is the split valance basis sets which take into account that the valance electrons are involved in bonding and chemical reactions. The most popular split valance basis sets are found by Pople [77] and in the form of X-YZG where X represents the number of primitive Gaussians consisting each core atomic basis function, and each valance orbital is described by two contractions, one with Y primitives and the other with Z primitive (for example 3-21G [78, 79] and 6-31G [80-83]).

The minimal and split valance basis sets do not take into account the polarization and diffusion effects. If polarization effect is neglected an atom will not be affected by the presence of the other one which does not happen to real systems. As two atoms get closer, the shape of the orbitals are distorted. This polarization effect is added to the basis sets by an "*" symbol. As an example, writing the electron configuration for the hydrogen atom shows that the electron is in the s-orbital and a p-orbital does not exist. Addition of polarization means that some of the 1s electron is in a p-orbital. The symbols "*" and "**" notation means that (d) and (d,p) orbitals added to the calculations. Diffuse functions are used when there is a probability of electrons being found away from the nucleus which is the case for the anions and excited systems. Diffuse basis sets are shown by a "+" symbol. If they are doubly diffused indicated by a "++" symbol.

2.1.5 Geometry Optimizations

Most of the calculations serve to find the optimized geometries of the molecules for which the system has the minimum energy. For a potential energy V and cartesian coordinates $\vec{r}$, the following equation is satisfied:

$$\frac{\partial V}{\partial \vec{r}} = 0. \tag{2.36}$$

A geometry optimization calculation can be performed to find a potential energy minimum or to get a new stable structure for the following single point, quantum chemical calculations or molecular dynamics simulations. In the HyperChem package program three types of optimization methods are available: steepest descent [84], conjugate gradient (Fletcher-Reeves and Polak-Ribiere) and block diagonal (Newton-Raphson). In this thesis steepest descent and Polak-Ribiere algorithms have been used and will be explained in the following. For a detailed information for the optimization techniques, the interested readers can consult to the Refs. [85-87].

2.1.5.1 Steepest (gradient) descent method

It is a first order minimization method and the simplest of the gradient methods. It uses the negative gradient of the potential energy to find a local minimum because the choice of the direction where the energy decreases is in the direction of negative gradient. If the positive gradient is followed, one reaches a local maximum of the energy which is known as the gradient ascent. The direction of the movement, i.e., the gradient $\vec{g}_i$, is calculated as:

$$\vec{g}_i = -\frac{\nabla V(\vec{r}_i)}{|\nabla V(\vec{r}_i)|}. \tag{2.37}$$

The minimum energy search starts at an arbitrary point and then move down the gradient. The iterative procedure is given by:

$$\vec{r}_{i+1} = \vec{r}_i + \lambda_i \vec{g}_i \tag{2.38}$$

where λ_i is the step size.

This method is very simple and fast, however the convergence towards a minimum is very slow. The process of the steepest descent method is illustrated in Fig. 2.4 [43]. The energy minimum is located at point M and the starting point is A. The importance of the step size can be seen in this figure. If the initial step size is appropriate then the next point on the potential energy surface will be the point B and then it follows the B-C path. However if the initial step size is large, the next step will be the point D and then it goes to a point on the D-E path which brings the position away from the minimum.

2.1.5.2 Conjugate gradient method with Polak-Ribiere algorithm

While the steepest descent method uses the gradient of the energy, conjugate gradient methods use both the current gradient and the previous search direc-

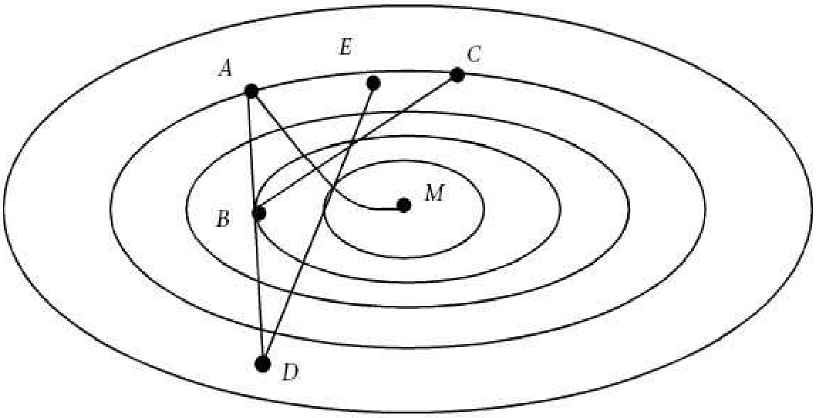

Figure 2.4: The steepest descent method searching for a minimum.

tion. The main advantage of the conjugate gradient methods over the steepest descent is that they search the minimum in all directions. Because of using the minimization history to find the gradient direction, it is faster than the steepest descent method. The new gradient of the search is given as

$$\vec{s}_{i+1} = \vec{g}_{i+1} + b_{i+1}\vec{s}_i \tag{2.39}$$

where the coefficient b mixes the new gradient with the old step information. The differences in the definition of the coefficient b yields different conjugate gradient methods. For example, the Polak-Ribiere method uses the following form:

$$b_{i+1} = \frac{(\vec{g}_{i+1} - \vec{g}_i) \cdot \vec{g}_{i+1}}{\vec{g}_i \cdot \vec{g}_i} \tag{2.40}$$

while the Fletcher-Reeves method uses the coefficient as:

$$b_{i+1} = \frac{\vec{g}_{i+1} \cdot \vec{g}_{i+1}}{\vec{g}_i \cdot \vec{g}_i}. \tag{2.41}$$

For non-quadratic functions Polak-Ribiere based algorithms found to give better results [87].

2.1.6 Molecular Dynamics

In the late 1950's molecular dynamics (MD) simulation was introduced by Alder and Wainwright [88, 89] to study the interactions of hard spheres and the first realistic system (liquid water) was studied by Stillinger and Rahman [90] in 1974. MD simulations are based on the computation of the equilibrium and transport properties of a classical many-body system where the classical implies that the nuclear motion of the particles obeys the laws of Newtonian mechanics. Performing a MD simulation is very similar to an experiment: first the model system is chosen consisting of N particles, then the Newton's equations of motion are solved until the system is equilibrated (i.e., there is no any change of the properties of the system with time), and finally the actual measurements are performed. In this section a brief introduction to MD simulations will be provided, for a detailed investigation the following textbooks are very complimentary [91-93].

A very simple MD program works as:

1. The initial positions and velocities to all particles in the system are assigned.
2. The forces on the particles are calculated.
3. The Newton's equations of motions are integrated.
4. The averages of the measured quantities are calculated.

There are many potential functions which serve to describe the motion of each particle the chose of which depends on the purpose and type of the calculation. Empirical potentials (Brenner potential [94]), pair and many-body potentials (Lennard-Jones potential [95], Tersoff potential [96]), semi-empirical potentials and polarizable potentials are the potentials that can be used to calculate the forces. Moreover, ab-initio [97] and hybrid quantum mechanical methods can be used in the MD simulations.

In this thesis, Tersoff potential and an empirical many-body potential [98] have been used in the MD simulations. Tersoff potential have been used to model the two- and three-body carbon interactions and C-Li, C-Li$^+$, Li-Li and Li$^+$-Li$^+$ interactions have been modeled by the by the many-body potential. The total interaction energy is taken to be the sum of two-body and three-body contributions:

$$\Phi = \phi_2 + \phi_3. \tag{2.42}$$

For the Tersoff potential, the explicit form of the two-body and three-body energies are:

$$\phi_2 = A \sum_{i<j}^{N} U_{ij}^{(1)} \tag{2.43}$$

$$\phi_3 = -B \sum_{i<j}^{N} U_{ij}^{(2)} \left[1 + \beta^n \left(\sum_{k \neq i,j}^{N} W_{ijk} \right)^n \right]^{-1/2n} \tag{2.44}$$

where U$_{ij}$ and W$_{ijk}$ are the two-body and three-body interactions and the forms are given as:

$$\begin{aligned} U_{ij}^{(1)} &= f_c(r_{ij}) exp(-\lambda_1 r_{ij}) \\ U_{ij}^{(2)} &= f_c(r_{ij}) exp(-\lambda_2 r_{ij}) \\ W_{ijk} &= f_c(r_{ik}) g(\theta_{ijk}) \end{aligned} \tag{2.45}$$

where

$$f_c(r) = \begin{cases} 1 & \text{for r<R-D} \\ \frac{1}{2} - \frac{1}{2}\sin[\frac{\pi}{2}(r-R)/D] & \text{for R-D< r <R+D} \\ 0 & \text{for r>R+D} \end{cases} \tag{2.46}$$

and

$$g(\theta_{ijk}) = 1 + \frac{c^2}{d^2} - \frac{c^2}{d^2 + (h - \cos\theta_{ijk})^2}. \tag{2.47}$$

The Tersoff potential parameters for carbon atom are: A=1393.6 eV, B=346.74 eV, λ_1=3.4879 Å^{-1}, λ_2=2.2119 Å^{-1}, β=1.5724×10^{-7}, n=0.72751, c=38049, d=4.3484, h=-0.57058, R=1.95 Å, and D=0.15 Å.

The potential energy function for C-Li, C-Li$^+$, and Li-Li is given:

$$U_{ij} = \frac{A_1}{r_{ij}^{\lambda_1}} exp(-\alpha_1 r_{ij}^2) - \frac{A_2}{r_{ij}^{\lambda_2}} exp(-\alpha_2 r_{ij}^2) \tag{2.48}$$

where A$_1$, A$_2$, λ_1, λ_2, α_1, and α_2 are the parameters given in Table 2.1 [98, 99].

Table 2.1: Parameters of the pair potential energy functions (energy is in eV and distance is in Å).

Parameter	C-Li	C-Li$^+$	Li-Li
A$_1$	12.6669958	38.4637591	13.8015320
A$_2$	6.78888092	21.3476845	2.80900799
λ_1	2.90177754	1.71241891	0.465222263
λ_2	0.08715453	1.16453151	0.165690375
α_1	0.0554067374	0.229357324	0.490324725
α_2	0.0967419455	0.133259571	0.101058131

The potential energy function for Li$^+$-Li$^+$ interaction is taken as purely repulsive:

$$U_{ij} = \frac{a'}{r_{ij}} exp(-b' r_{ij}) \tag{2.49}$$

where a' and b' are the parameters (a'=0.5429457 eV Å, b'=0.0033331 Å^{-1}) [98, 99].

After calculating the interaction energies one can easily find the forces between the particles. Now everything is ready for the integration of Newton's equations of motion. The simplest way to construct an integrator is to expand the positions and velocities in a Taylor series. These type of algorithms are named as Verlet algorithm [100, 101]. For a small time step δt, the Taylor expansion is:

$$r(t+\delta t) = r(t) + v(t)\delta t + \frac{a(t)}{2}\delta t^2 + \frac{1}{6}\frac{d^3r}{dt^3}\delta t^3 + O(\delta t^4)... \tag{2.50}$$

and in a similar manner

$$r(t-\delta t) = r(t) - v(t)\delta t + \frac{a(t)}{2}\delta t^2 - \frac{1}{6}\frac{d^3r}{dt^3}\delta t^3 + O(\delta t^4)... \tag{2.51}$$

Addition of the Eq. 2.50 and 2.51 gives:

$$r(t+\delta t) = 2r(t) - r(t-\delta t) + a(t)\delta t^2 + O(\delta t^4). \tag{2.52}$$

As can be seen form the Eq. 2.52, velocity is not needed while computing the position of the particle, however, for the control of the energy conservation the velocity is also required. Substraction of Eq. 2.51 from Eq. 2.50 and dividing by the time step δt gives:

$$v(t) = \frac{r(t+\delta t) - r(t-\delta t)}{2\delta t} + O(\delta t^2). \tag{2.53}$$

This velocity algorithm calculates the velocities at time step t, not at t+δt or t+δt. The leap-frog algorithm [102] solves this problem. According to this algorithm the velocity is calculated at half time steps which uses the acceleration information at t and the previous velocity at (t-$\frac{1}{2}$δt):

$$v\left(t + \frac{1}{2}\delta t\right) = v\left(t - \frac{1}{2}\delta t\right) + a(t)\delta t \tag{2.54}$$

and the position can be calculated using this velocity:

$$x(t+\delta t) = x(t) + v\left(t + \frac{1}{2}\delta t\right)\delta t. \tag{2.55}$$

The last two equations shows that the velocity and the position of the particles can not be determined simultaneously. The velocity at time t can be approximated as:

$$v(t) = \frac{v(t+\frac{\delta t}{2}) + v(t-\frac{\delta t}{2})}{2}. \tag{2.56}$$

The "velocity Verlet algorithm" is used to overcome this problem which stores information from one time step using:

$$r(t+\delta t) = r(t) + v(t)\delta t + \frac{1}{2}a(t)\delta t^2 \tag{2.57}$$

$$v(t+\frac{\delta t}{2}) = v(t) + \frac{1}{2}\delta t a(t). \tag{2.58}$$

$$a(t+\delta t) = -\frac{1}{m}\nabla V|_{r(t+\delta t)} \tag{2.59}$$

$$v(t+\delta t) = v(t+\frac{\delta t}{2}) + \frac{1}{2}a(t+\delta t)\delta t. \tag{2.60}$$

2.2 Properties of Carbon Nano Structures

Carbon is one of the most interesting elements in the periodic table since it is found in many different forms such as graphite, graphene, diamond, carbon fibers, fullerens and carbon nanotubes. This variety in carbon arises from the fact that it can form different types of valence bonds (hybridization).

It is very surprising that although the discovery of graphene [103] is very late (in 2004) when compared with the other types of carbon, it is the starting point for all other types. Graphene is a planar sheet of sp^2-bonded carbon atoms in the form of a honeycomb crystal lattice. The unit cell and the Brillouin zone of the two-dimensional graphene is shown in Fig. 2.5 [104].

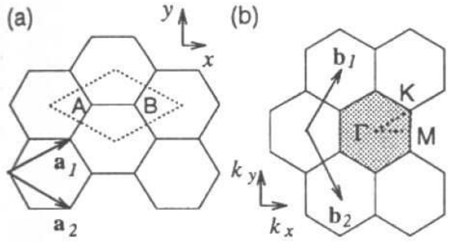

Figure 2.5: (a) The unit cell and (b) Brillouin zone of graphene are shown as the dotted rhombus and the shaded hexagon, respectively.

In the above figure, $\vec{a}_i$ are the unit vectors in real space and $\vec{b}_i$ are the reciprocal lattice vectors. In the x,y coordinates, the unit vectors $\vec{a}_1$ and $\vec{a}_2$ are expressed as:

$$\vec{a}_1 = \left(\frac{\sqrt{3}a}{2}, \frac{a}{2}\right), \quad \vec{a}_2 = \left(\frac{\sqrt{3}a}{2}, -\frac{a}{2}\right) \tag{2.61}$$

where a=2.46 Å is the lattice constant of graphene. The reciprocal lattice vectors are given as:

$$\vec{b}_1 = \left(\frac{2\pi}{\sqrt{3}a}, \frac{2\pi}{a}\right), \quad \vec{b}_2 = \left(\frac{2\pi}{\sqrt{3}a}, -\frac{2\pi}{a}\right) \tag{2.62}$$

which has a lattice constant of $4\pi/\sqrt{3}a$. The high symmetry points are the Γ, K and M and the energy dispersion relation is calculated for the triangle formed by these three symmetry points.

In 1985, Kroto [1] found C_{60} in molecular beam experiments the discovery of that brought them the 1996 Nobel Prize in Chemistry. C_{60} is named as buckminsterfullerene because of the resemblance to the geodesic domes built by the architect R. Buckminster Fuller. C_{60} has 12 pentagons and 20 hexagons as faces like a football. The smallest possible fullerene is C_{20} the production of which was a hard process because of the high curvature of the surface [105].

A single wall carbon nanotube (SWCNT) [2] is described as rolling-up a graphene sheet on a seamless cylinder. Because of the large aspect ratio of the cylinder (length to diameter ratio which can be as large as 10^4-10^5), these structures are considered as one-dimensional nanostructures. A graphene sheet can be rolled more than one way and the rolling up vector is defined as $\vec{C}_h = n\vec{a}_1 + m\vec{a}_2 \equiv (n,m)$ where $\vec{a}_1$ and $\vec{a}_2$ are the primitive lattice vectors of the graphene and n, m are integers as shown in Fig. 2.6 [104]. The length of the chiral vector is the circumference of the cylinder and the angle between the chiral vector and the the basis vector $\vec{a}_1$ is the chiral angle θ and it is defined as:

$$\cos\theta = \frac{\vec{C}_h \cdot \vec{a}_1}{\mid \vec{C}_h \mid\mid \vec{a}_1 \mid} = \frac{2n+m}{2\sqrt{n^2+m^2+nm}}. \tag{2.63}$$

The diameter of the CNT, d_t is calculated as L/π , where L is the circumferential length of the tube:

$$d_t = L/\pi, \quad L = \mid \vec{C}_h \mid = \sqrt{\vec{C}_h \cdot \vec{C}_h} = a\sqrt{n^2 + m^2 + nm}. \tag{2.64}$$

The length of the translation vector defines the nanotube unit cell length and it is perpendicular to $\vec{C}_h$ and parallel to the nanotube axis. The lattice vector can be defined as:

$$\vec{T} = t_1\vec{a}_1 + t_2\vec{a}_2 \equiv (t_1, t_2) \tag{2.65}$$

where t_1 and t_2 are integers.

There are three directions of the that the chiral vector can take which are named as armchair, zigzag, and chiral and designated by (n,0), (n,n) and (n,m), respectively. The names of these tubes come out from the shape of the cross-sectional ring. Since the mirror images of the armchair and zigzag nanotubes have an identical structure to the original ones they are classified as the achiral (symmorphic). On the other hand, chiral tubes have a spiral symmetry so they do not have a mirror image. The chiral angles of the armchair tubes are equal to 30°, zigzag tubes are 0°, and the chiral tubes are $0° < |\theta| < 30°$. The three types of CNTs are shown in Fig. 2.7.

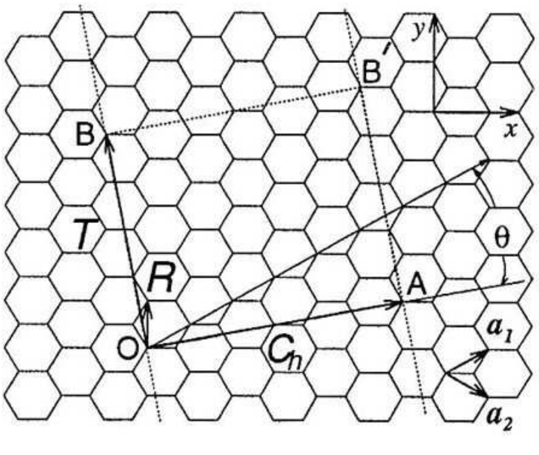

Figure 2.6: The conventional model describing a CNT formed from a graphene sheet.

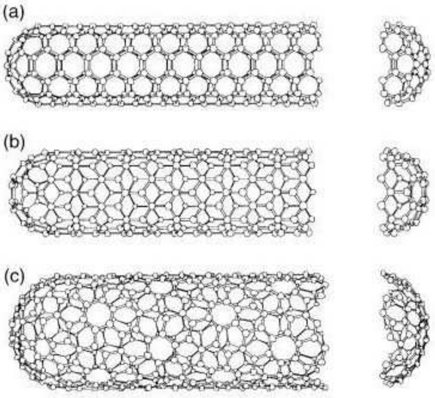

Figure 2.7: The armchair, zigzag and chiral nanotube a)(5,5), b)(9,0), c)(10,5) nanotube.

CHAPTER 3

Li/Li$^+$ ION DOPED CARBON NANOSYSTEMS

3.1 Li/Li$^+$ Ion Interaction with Fullerenes and Single Walled Carbon Nanotubes

In this section, Li atom and Li$^+$ ion interactions with fullerenes (C_{20} and C_{60}) and SWCNTs (C(4,4), C(5,5), C(7,0), and C(8,0)) have been investigated by performing molecular dynamics (MD) simulations [99]. All of the atoms in the simulations were free to move and the canonical ensemble MD NVT [106] have been proceeded. The temperature of the systems was kept constant at 1K and one time step was taken as 10^{-16} seconds. Periodic boundary conditions were not used in the simulations. More details of the MD simulations have been given in Chapter 2.

The total number of carbon atoms in the C(4,4), C(5,5), C(7,0), and C(8,0) is 80, 100, 98, and 112, respectively. The initial distance between the Li-Li and Li$^+$-Li$^+$ is 3 $\AA$. The reason of this specific distance is the following: Li atoms give their 2s electron to the carbon nanotube and then they are positively charged [107]. The tubes are polarizable and they provide very good screening, hence two Li atoms separated by more than 3 $\AA$ in the tube do not see each other. Also in order to avoid forming clusters in the tube the distances between the Li-Li are taken to be 3 $\AA$ in the optimization procedure. This can be seem that the concentration of the Li/Li$^+$ ion in the systems will be low however, Liu et al. [107] found that C(6,0) tube could exothermally absorb at least 9 Li atoms

Table 3.1: Calculated total potential energy (in eV) of the endohedral doped Li/Li$^+$ ion systems.

System	Energy	System	Energy	System	Energy
$Li^+@C_{20}$	-85.7	$2Li^+@C_{20}$	-	$3Li^+@C_{20}$	-
$Li@C_{20}$	-146.3	$2Li@C_{20}$	-	$3Li@C_{20}$	-
$Li^+@C_{60}$	-363.3	$2Li^+@C_{60}$	-429.9	$3Li^+@C_{60}$	-
$Li@C_{60}$	-438.9	$2Li@C_{60}$	-558.2	$3Li@C_{60}$	-
$Li^+@C(4,4)$	-427.5	$2Li^+@C(4,4)$	-477.6	$3Li^+@C(4,4)$	-527.7
$Li@C(4,4)$	-510.3	$2Li@C(4,4)$	-591.0	$3Li@C(4,4)$	-772.8
$Li^+@C(5,5)$	-505.2	$2Li^+@C(5,5)$	-562.9	$3Li^+@C(5,5)$	-629.8
$Li@C(5,5)$	-585.4	$2Li@C(5,5)$	-713.4	$3Li@C(5,5)$	-830.3
$Li^+@C(7,0)$	-559.9	$2Li^+@C(7,0)$	-632.6	$3Li^+@C(7,0)$	-677.8
$Li@C(7,0)$	-634.6	$2Li@C(7,0)$	-771.4	$3Li@C(7,0)$	-891.7
$Li^+@C(8,0)$	-634.3	$2Li^+@C(8,0)$	-702.5	$3Li^+@C(8,0)$	-732.2
$Li@C(8,0)$	-706.5	$2Li@C(8,0)$	-873.7	$3Li@C(8,0)$	-936.5

which is a high concentration.

Endohedral and exohedral doping of Li/Li$^+$ ion into fullerenes and SWCNTs have been studied in order to investigate the structural properties and the energetics of these systems. It was found that endohedral doping is more favorable than exohedral doping since, the energy of the systems with endohedral Li/Li$^+$ ion doping is lower than the exohedral doping (see Tables 3.1 and 3.2). Lithium atom doped systems have less energy than the lithium ion doped systems indicating that the former is more stable than the latter.

The optimized geometries of endohedral Li$^+$ ion doped fullerenes are shown in Fig. 3.1. C_{20} molecule has the smallest radius among the fullerenes, so doping of more than one Li/Li$^+$ ion has caused deformation on the system. Similarly, not more than two Li/Li$^+$ ions could have been doped to C_{60} without any deformation on the structure. For the minimum energy configuration of the systems, Li/Li$^+$ ion prefers to locate on the center of the fullerenes. The lowest-energy structures for the endohedral Li$^+$ ion doped SWCNTs are presented in Fig. 3.2. As can be seen from the figure, Li/Li$^+$ ion is located on the axis of the tube.

Table 3.2: Calculated total potential energy (in eV) of the exohedral doped Li/Li$^+$ ion systems.

System	Energy	System	Energy	System	Energy
$Li^+@C_{20}$	-72.6	$2Li^+@C_{20}$	-	$3Li^+@C_{20}$	-
$Li@C_{20}$	-89.9	$2Li@C_{20}$	-	$3Li@C_{20}$	-
$Li^+@C_{60}$	-325.2	$2Li^+@C_{60}$		$3Li^+@C_{60}$	
$Li@C_{60}$	-329.9	$2Li@C_{60}$	-347.8	$3Li@C_{60}$	-
$Li^+@C(4,4)$	-356.4	$2Li^+@C(4,4)$	-403.0	$3Li^+@C(4,4)$	-420.6
$Li@C(4,4)$	-372.8	$2Li@C(4,4)$	-418.3	$3Li@C(4,4)$	-442.9
$Li^+@C(5,5)$	-465.5	$2Li^+@C(5,5)$	-494.1	$3Li^+@C(5,5)$	-512.2
$Li@C(5,5)$	-482.4	$2Li@C(5,5)$	-508.4	$3Li@C(5,5)$	-532.1
$Li^+@C(7,0)$	-525.2	$2Li^+@C(7,0)$	-549.8	$3Li^+@C(7,0)$	-565.7
$Li@C(7,0)$	-530.6	$2Li@C(7,0)$	-552.2	$3Li@C(7,0)$	-575.4
$Li^+@C(8,0)$	-589.6	$2Li^+@C(8,0)$	-609.6	$3Li^+@C(8,0)$	-616.5
$Li@C(8,0)$	-601.2	$2Li@C(8,0)$	-618.4	$3Li@C(8,0)$	-642.3

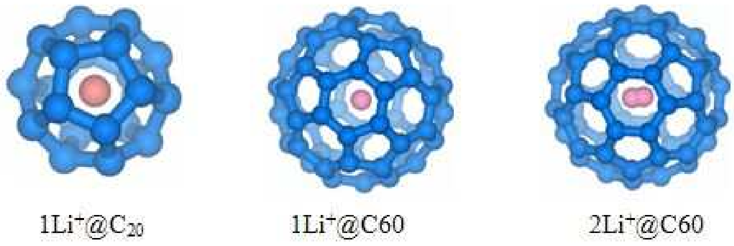

Figure 3.1: The optimized geometries for the endohedral Li$^+$ ion doped C$_{20}$ and C$_{60}$. (Similar geometries are found for Li case.)

The pair potential energy profiles for C-Li, C-Li$^+$ ion, and Li-Li are shown in Fig. 3.3 and the minima occurs at about 2.1 $\AA$, 2.5 $\AA$, and 2.8 $\AA$, respectively. Moreover, there is a sharp decrease in energy below and a slow increase above these minima. Also, C-Li interaction is stronger than the C-Li$^+$ ion interaction, which is consistent with the calculated total energy values of the systems.

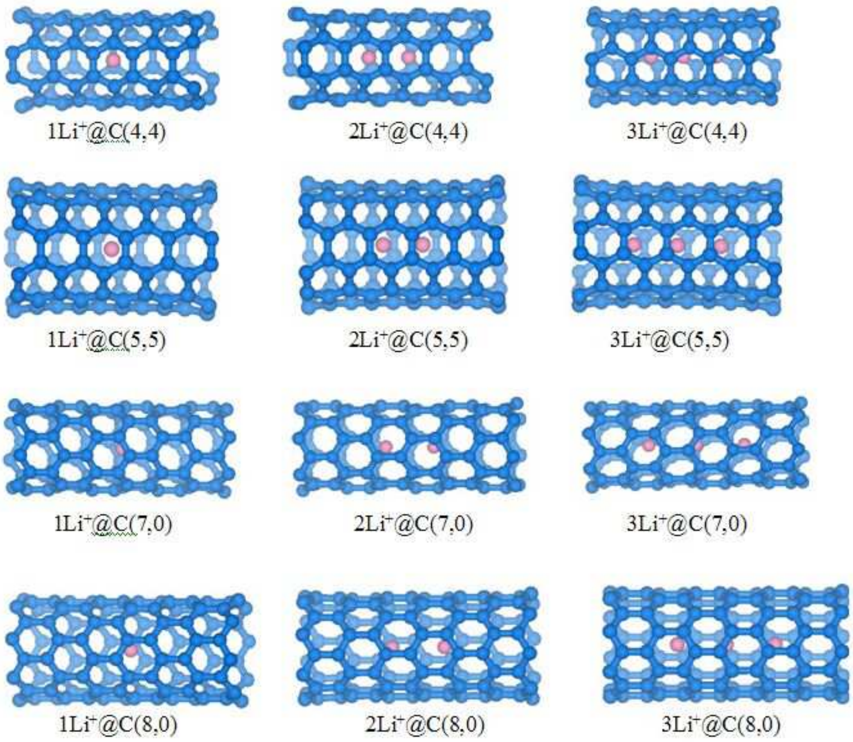

1Li$^+$@C(4,4) 2Li$^+$@C(4,4) 3Li$^+$@C(4,4)

1Li$^+$@C(5,5) 2Li$^+$@C(5,5) 3Li$^+$@C(5,5)

1Li$^+$@C(7,0) 2Li$^+$@C(7,0) 3Li$^+$@C(7,0)

1Li$^+$@C(8,0) 2Li$^+$@C(8,0) 3Li$^+$@C(8,0)

Figure 3.2: The optimized geometries for Li$^+$ ion confined within C(4,4), C(5,5), C(7,0), and C(8,0) SWCNTs. (Similar geometries are found for Li case.)

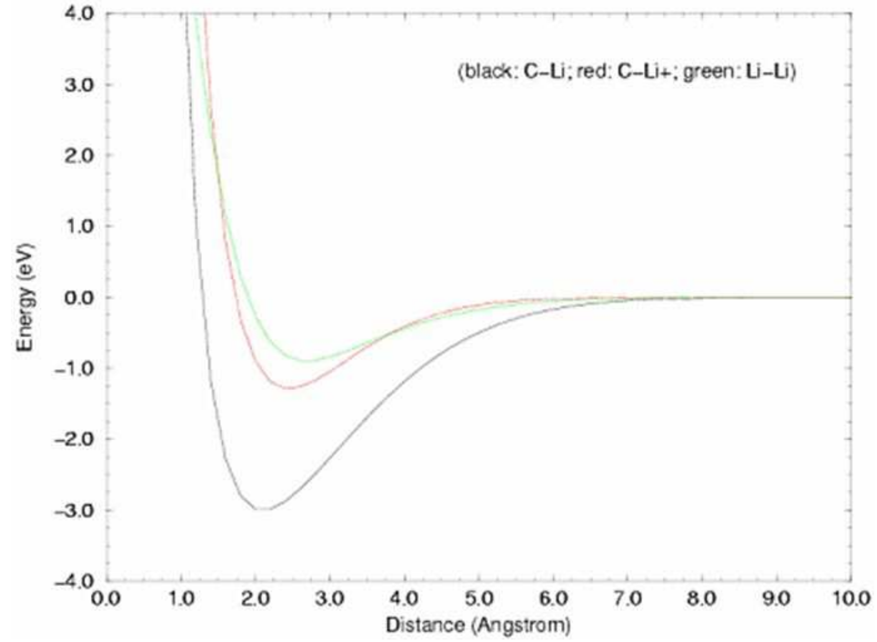

Figure 3.3: The pair potential profiles for C-Li, C-Li$^+$ ion, and Li-Li.

3.2 Li/Li^{+} Ion Doped Carbon Nanocapsules Studied with Semi-Empirical MO Method at PM3 Level

In this section, the interaction of Li/Li^{+} ion with carbon nanocapsules will be presented [108]. Carbon nanocapsules are formed by using SWCNTs the open sides of which have been capped with half of the fullerenes (see Fig. 2.7). Li/Li^{+} ion doped armchair C(5,5) and zigzag C(9,0) carbon nanocapsules have been investigated through the molecular mechanics and semi-empirical molecular orbital self-consistent-field (SCF) methods. Initially the geometries of the undoped capsules have been optimized by using the molecular mechanics method with MM+ force field which facilitated the further optimizations (PM3 type calculation). The optimized geometries of capsules have been doped with Li/Li^{+} ion and these systems have been optimized in their ground states. Polak-Ribiere algorithm has been used as the conjugate gradient method. In order to get sufficient accuracy in the calculations the SCF convergence limit was set to 0.001 kcal/mol and the root-mean-square (RMS) gradient was set to 0.001 kcal/($\mathring{A}$ mol). These computations have been performed using HyperChem package program. Moreover, molecular dynamics simulations have been performed to find the optimized geometries of the systems and the corresponding total interaction energies.

Carbon nanocapsules are formed by using C_{60} fullerene because the diameters of the C(5,5) and C(9,0) tubes and the C_{60} are very close to each other. The initial lengths of C(5,5) and C(9,0) capsules were 14.478 and 17.677 $\mathring{A}$ and the initial diameters were 7.031 and 7.284 $\mathring{A}$, respectively. The molecular properties of the systems are presented in Table 3.3. After the optimization process of the capsules doped with Li/Li^{+} ion, it was found that the length of the C(5,5) and C(9,0) systems decreased about 0.35 and 0.49 $\mathring{A}$, and the decrease in the diameters was at about 0.19 and 0.24 $\mathring{A}$, respectively. These diminishes on the diameters and the lengths implies that the doping of Li/Li^{+} ion to the capsules causes the capsules shrink slightly.

Table 3.3: Molecular properties of the Li/Li$^+$ ion doped C(5,5) and C(9,0) nanocapsule systems.

Quantity	Li@C(5,5)	Li$^+$@C(5,5)	Li@C(9,0)	Li$^+$@C(9,0)
No. of C atoms	120	120	150	150
Length of capsule ($\AA$)	14.136	14.111	17.191	17.198
Diameter of capsule ($\AA$)	7.032	7.032	7.284	7.284
No. of electrons	481	480	601	600
No. of α electrons	241	240	301	300
No. of β electrons	240	-	300	-
Total no. of orbitals	484	484	604	604

Table 3.4: Calculated energy values (in kcal/mol) of the Li/Li$^+$ ion doped C(5,5) and C(9,0) nanocapsule systems.

Quantity	Li@C(5,5)	Li$^+$@C(5,5)	Li@C(9,0)	Li$^+$@C(9,0)
Total energy	-327256.19	-327039.97	-409131.96	-408175.10
Binding energy	-19324.97	-19108.75	-24248.48	-24034.04
Isolated atomic energy	-307931.23	-307931.23	-384883.48	-384883.48
Electronic energy	-6823215.78	-6851142.88	-9621611.84	-9642306.04
Core-core int. energy	6495959.59	6524102.90	9212479.88	9233388.52
Heat of formation	1220.24	1436.46	1423.43	1637.87

The total energy calculations with semi-empirical method at PM3 level reveal that the total energies of the Li atom doped capsules are smaller (in magnitude) than the total energies of the Li$^+$ ion doped capsules which means that for both of the systems lithium doped capsules are more stable than lithium ion doped capsules. These results can be seen from the binding energy values (see Table. 3.4). The electronic energies of lithium ion doped capsules are found to be more negative and the core-core interaction energies of lithium atom doped capsules are smaller than that of lithium ion doped systems. All the systems are found to have endothermic heat of formation values and the lithium ion doped systems are found to be more endothermic than lithium atom doped systems.

The calculated molecular orbital eigenvalues such as the lowest occupied and the highest unoccupied molecular orbital energies (LOMO and HUMO, respectively)

Table 3.5: Calculated molecular orbital eigenvalues (in eV), dipole moments (in Debyes) and the accumulated charges on the Li/Li$^+$ ion for the C(5,5) and C(9,0) nanocapsule systems.

Quantity	Li@C(5,5)	Li$^+$@C(5,5)	Li@C(9,0)	Li$^+$@C(9,0)
LOMO (α)	-48.132	-50.954	-48.116	-50.584
HOMO (α)	-7.137	-10.741	-7.807	-10.045
LUMO (α)	-2.854	-5.952	-2.927	-6.093
E$_g$ (α)	4.283	4.789	4.880	3.952
HUMO (α)	5.982	3.180	5.571	3.409
LOMO (β)	-48.117	-	-48.103	-
HOMO (β)	-8.501	-	-7.676	-
LUMO (β)	-2.849	-	-3.353	-
E$_g$ (β) 5.652	-	4.323	-	
HUMO (β) 6.065	-	5.590	-	
Dipole moment	6.841	1.905	3.254	1.726
Charge on Li$^+$	0.666	0.675	0.641	0.688

as well as the frontier molecular orbital energies (the highest occupied HOMO and the lowest unoccupied LUMO, respectively), the interfrontier molecular orbital energy gaps (LUMO-HOMO difference, E$_g$), and the dipole moments of the studied systems are presented in Table 3.5. It can be inferred from the MO energy values that both HOMO and LUMO energy levels of α-orbitals of lithium ion doped systems are lower than that of the lithium atom doped systems. While the LUMO energy level of β-orbitals of Li@C(5,5) system is higher than that of Li@C(9,0), the HOMO energy level of β-orbitals of Li@C(5,5) system is lower than that of Li@C(9,0). The E$_g$ of α-orbital of Li@C(5,5) is lower than that of Li$^+$@C(5,5) and Li@C(9,0) but higher than that of Li$^+$@C(9,0) and the energy gap of the β-orbital of Li@C(5,5) is higher than that of Li@C(9,0). The calculated dipole moment of the system gives information about the symmetry of the structures. All of the systems have non-zero dipole moment values implying the systems are asymmetric. Li@C(5,5) system has the largest dipole moment since after the optimization the change in the position of the lithium atom is the largest when compared with the other systems. The net accumulated charges on Li/Li$^+$ ion are given in Table 3.5.

3D plots of HOMO, LUMO, charge density (CD) and electrostatic potential (EP) of the systems are presented in Figs. 3.4-3.7. While HOMO of the Li@C(5,5) system is localized on carbon atoms which are close to the lithium atom, LUMO is totally localized on lithium atom. HOMO and LUMO of Li^+@C(5,5) are localized on the surface of the capsule, the former aligned horizontally and the latter aligned vertically. HOMO and LUMO of Li@C(9,0) system are localized on different sides of the capsule. HOMO and LUMO of Li^+@C(9,0) are localized on the surface of the capsule but the former is more localized than the latter. The 3D charge density distributions of the systems considered seem to be homogeneous, the electrons are localized in the vicinity of the surface atoms and the interior of the capsules are charge free apart from the lithium sites. There is a slight increase in EP in the vicinity of Li/Li^+ ion. If lithium was closer to surface the effects of this gradient would be observed more. Since lithium has one valance electron which causes a net spin density on the corresponding systems; the plot of the homogeneous spin densities are shown in Fig. 3.8.

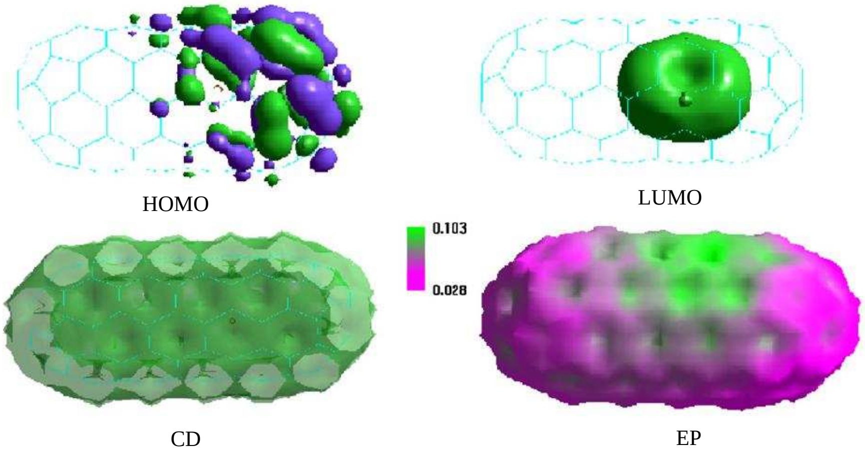

Figure 3.4: 3D plots of HOMO, LUMO, charge density (CD), and electrostatic potential (EP) for the Li@C(5,5) capsule.

Molecular dynamics simulations have been performed to investigate the energetics and the structural properties of the studied systems. The total energies

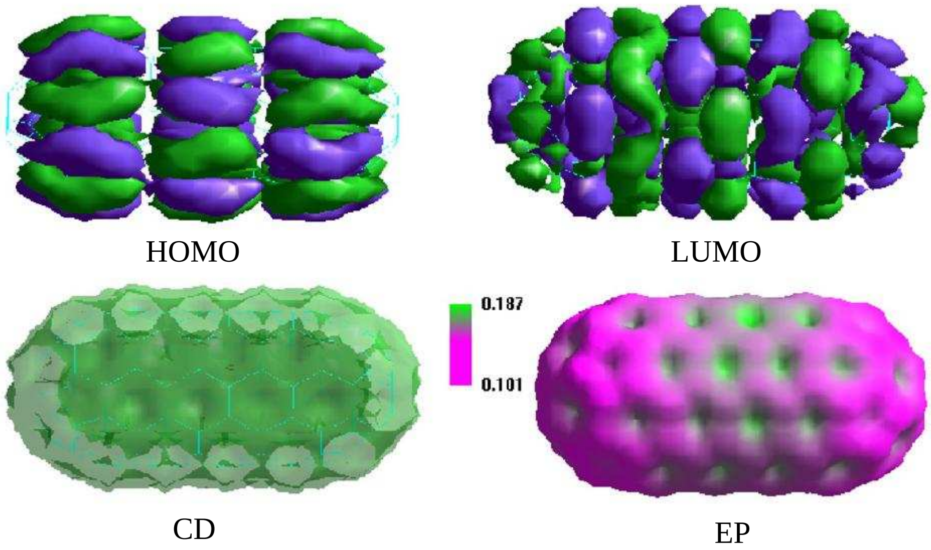
HOMO
LUMO
0.187
0.101
CD
EP

Figure 3.5: 3D plots of HOMO, LUMO, charge density (CD), and electrostatic potential (EP) for the Li^+@C(5,5) capsule.

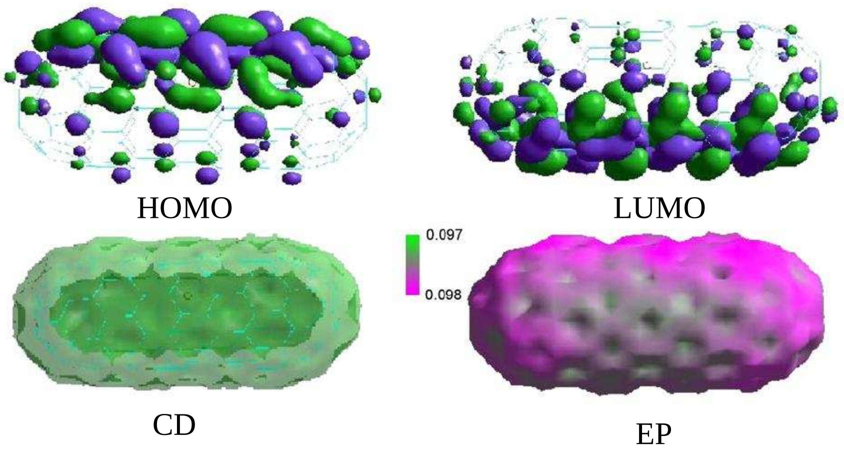
HOMO
LUMO
0.097
0.098
CD
EP

Figure 3.6: 3D plots of HOMO, LUMO, charge density (CD), and electrostatic potential (EP) for the Li@C(9,0) capsule.

are found to be -711.33, -629.30, -843.43, and -757.93 eV for the Li@C(5,5), Li^+@C(5,5), Li@C(9,0), and Li^+@C(9,0) systems, respectively. The relaxed geometries are found to be very similar to the optimized geometries of PM3 results.

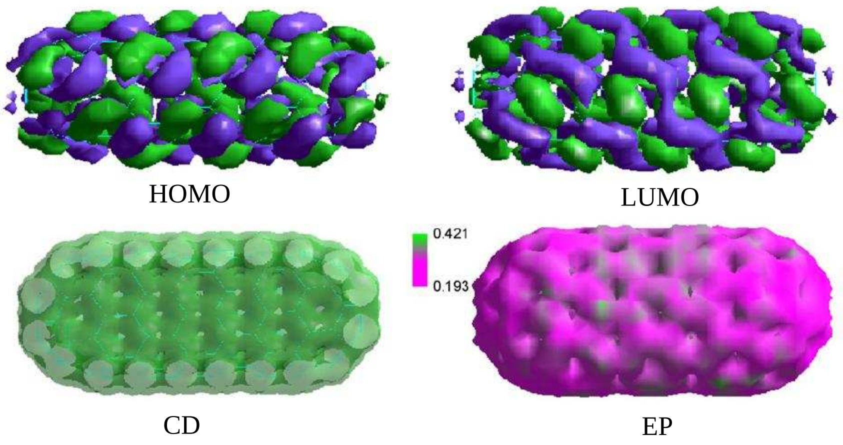

Figure 3.7: 3D plots of HOMO, LUMO, charge density (CD), and electrostatic potential (EP) for the Li^+@C(9,0) capsule.

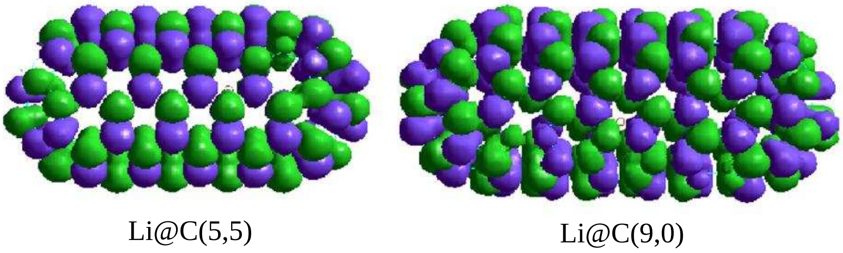

Figure 3.8: 3D plots of spin densities of Li@C(5,5) and Li@C(9,0) systems.

3.3 The Structural and Electronic Properties of Stone-Wales and Mono-Vacancy Defected Carbon Nanocapsules

The optimized geometries, electronic structures and some thermodynamical values of the Stone-Wales (SW) and mono-vacancy defected C(5,5) and C(9,0) CNCs have been studied in their ground states [109]. The initial geometries of the defected capsules have been optimized by applying molecular mechanics method using MM+ force field. Then semi-empirical MO method at PM3 level within the RHF formalism has been used for the further optimization using HyperChem package. The SCF convergence limit and RMS gradient were set to 0.001 kcal/mol and0.001 kcal/($\mathring{A}$ mol), respectively, in the calculations to get sufficient structural optimization. The optimized geometries have been taken and using Gaussian 03 package program further optimizations have been performed applying molecular mechanics method at UFF level and semi-empirical MO method at PM3 level. The single point energy calculations of the final geometries of the optimized structures have been performed using DFT method with B3LYP exchange-correlation functional with 3-21G basis set.

Stone-Wales defects are formed by the rotation of a C-C bond by 90° in the hexagonal network which change four hexagons into two pentagons and two heptagons and, which is also known as 5-7-7-5 defect. Vacancy defects result from removing carbon atoms from the surface. When a single atom is removed from the nanotube, two of three carbon atoms rebond and the third atom has the dangling bond (DB) even after the relaxation, forming a pentagon ring coupling with a DB left, and named as 5-1DB defect. The number of carbon atoms in the systems is 120 and 119 for C(5,5) and 114 and 113 for C(9,0) with SW and vacancy defects, respectively. The capsules having SW and vacancy type defects are shown in Fig. 3.9.

The calculated energy values of the optimized (PM3 level with HyperChem package) systems are presented in Tables 3.6 and 3.7. The total energies per atom of C(9,0) defected systems are smaller in magnitude than the total energies per atom of the C(5,5) defected systems, which means that C(5,5) systems are more stable than C(9,0) systems. The most stable system is the C(5,5) capsule with 0-type vacancy defect and the least stable system is the C(9,0) capsule with B-type vacancy defect. These results can be validated by comparing the binding energies of the systems. For the C(5,5) and C(9,0) systems the electronic energies of 0-type VD are more negative and the core-core interaction energies are more repulsive than the other types of the VD capsules. The calculations give endothermic heat of formation values for the studied systems.

The highest occupied and the lowest unoccupied molecular orbital energies, namely HOMO and LUMO energies, the lowest occupied and the highest unoc-

Table 3.6: Calculated energy values (in kcal/mol) of C(5,5) capsule systems (TE: total energy, BE: binding energy, IAE: isolated atomic energy, EE: electronic energy, CCI: core-core interaction, and HOF: heat of formation).

Quantity	0-type VD	A-type VD	B-type VD	C-type VD	SW defect
TE	-327097.12	-324213.05	-324220.36	-324178.38	-327009.96
BE	-19288.12	-18969.12	-18976.43	-18934.45	-19200.95
IAE	-307809.00	-305243.93	-305243.93	-305243.93	-307809.00
EE	-6828150.92	-6732122.99	-6732431.70	-6723875.78	-6819317.80
CCI	6501053.80	6407909.94	6408211.33	6399697.39	6492307.84
HOF	1218.69	1366.79	1359.48	1401.46	1305.85

Table 3.7: Calculated energy values (in kcal/mol) of C(9,0) capsule systems (TE: total energy, BE: binding energy, IAE: isolated atomic energy, EE: electronic energy, CCI: core-core interaction, and HOF: heat of formation).

Quantity	0-type VD	A-type VD	B-type VD	C-type VD	SW defect
TE	-307824.67	-307824.67	-307786.68	-307833.77	-310668.45
BE	-17971.19	-17971.19	-17933.20	-17980.29	-18249.89
IAE	-289853.48	-289853.48	-289853.48	-289853.48	-292418.55
EE	-6222789.06	-6222787.11	-6216046.90	-6214507.87	-6307316.99
CCI	5914964.39	5914962.44	5908260.22	5906674.10	5996648.54
HOF	1339.38	1339.38	1377.37	1330.28	1231.56

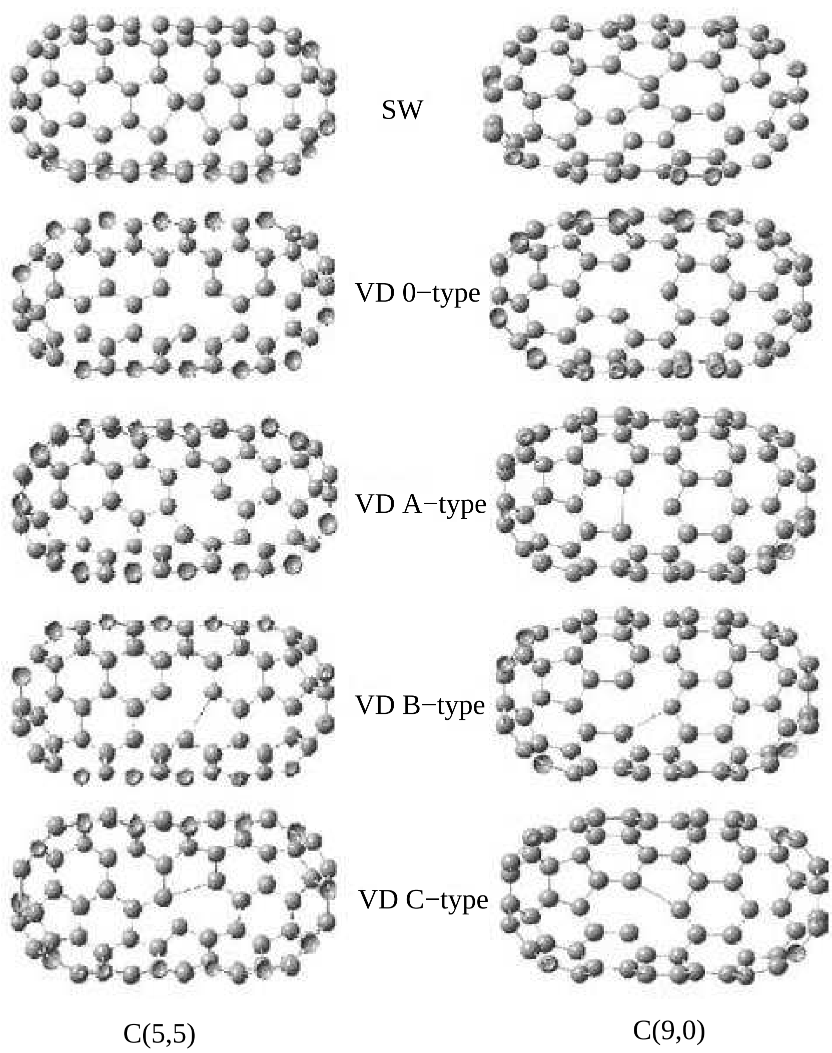

Figure 3.9: Stone-Wales and mono-vacancy defects for C(5,5) and C(9,0) nanocapsules before the optimizations.

cupied molecular orbital energies, namely LOMO and HUMO energies, respectively, and the interfrontier molecular orbital energy gap, that is LUMO-HOMO energy difference, E_g, and the calculated dipole moment values of the defected systems are given in Tables 3.8 and 3.9. The LOMO and HUMO energy values of the different systems are very close to each other. The E_g of the C(9,0) defected capsules are smaller than the E_g of the C(5,5) capsules. Moreover, B-type vacancy defected C(5,5) capsule has the highest E_g value. The dipole moments of the SW defected capsules are smaller than that of VD capsules because SW defected systems are more symmetric than the VD systems. Furthermore, SW

Table 3.8: Calculated molecular orbital energy eigenvalues (in a.u.) and the dipole moments (μ) (in Debyes) of C(5,5) capsule systems.

Quantity	0-type VD	A-type VD	B-type VD	C-type VD	SW defect
LOMO	1.768	1.768	1.768	1.767	1.768
HOMO	0.305	0.305	0.311	0.301	0.292
LUMO	0.131	0.131	0.124	0.141	0.131
E_g	0.174	0.174	0.187	0.160	0.161
HUMO	0.200	0.200	0.201	0.201	0.200
μ	1.633	1.675	1.026	5.663	1.240

Table 3.9: Calculated molecular orbital energy eigenvalues (in a.u.) and the dipole moments (μ) (in Debyes) of C(9,0) capsule systems.

Quantity	0-type VD	A-type VD	B-type VD	C-type VD	SW defect
LOMO	1.767	1.767	1.767	1.766	1.764
HOMO	0.302	0.302	0.297	0.301	0.292
LUMO	0.134	0.134	0.143	0.136	0.137
E_g	0.168	0.168	0.154	0.165	0.155
HUMO	0.200	0.200	0.200	0.200	0.203
μ	1.537	1.538	3.102	1.371	0.402

defected C(9,0) capsule has a smaller dipole moment than the C(5,5) capsule.

Further optimizations using semi-empirical MO method at PM3 level using Gaussian 03 program have been performed and 3-dimensional plots of charge by color, HOMO, LUMO, and total charge density (TCD) of the systems are presented in Figs. 3.10-3.19. From the charge by color figures it can be seen that positive and negative charges are accumulated on the defective regions of the capsules. The figures of the total charge distribution show that the distributions are homogenous except at the defected regions where there are outward deformations because of the excess charges on these sides. While HOMO of SW-defected C(5,5) capsule is mainly localized on the right side of the defect, LUMO of the same type capsule is more uniformly distributed and the HOMO aligned horizontally and the LUMO aligned vertically. Whereas HOMO of SW-defected C(9,0) capsule is mainly localized on the defect region but distributed to the other carbon atoms, LUMO are localized on the defect and on the right side of the defect. HOMO

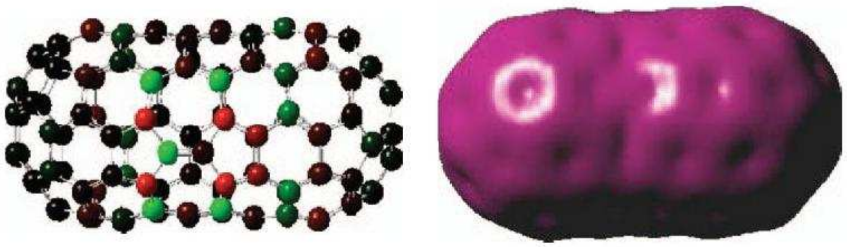

charge by color charge density

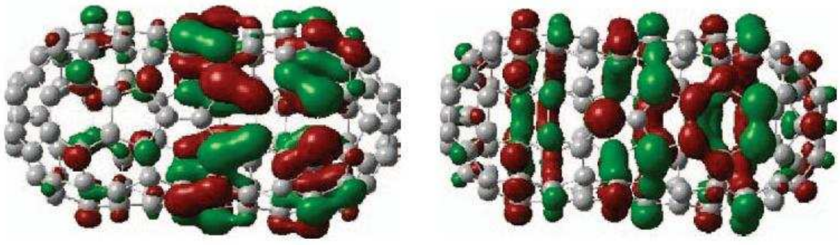

HOMO LUMO

Figure 3.10: 3D plots of charge distribution by color, total charge density, HOMO, and LUMO for the SW defected C(5,5) capsule.

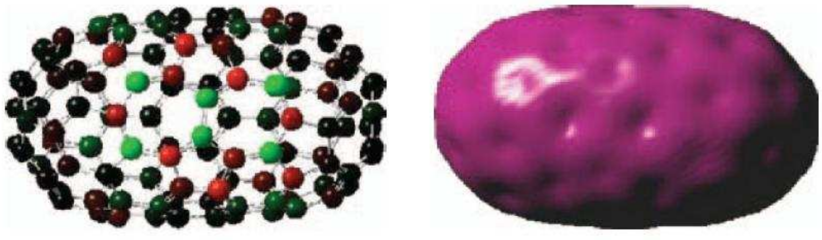

charge by color charge density

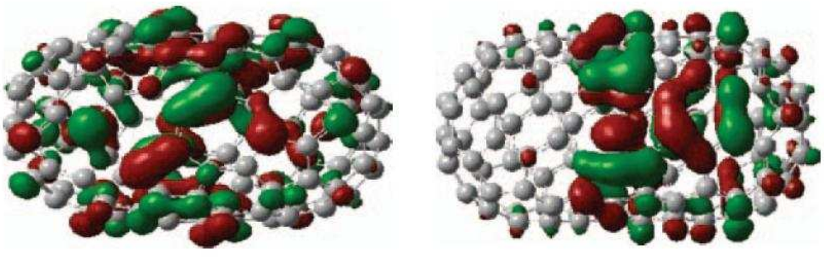

HOMO LUMO

Figure 3.11: 3D plots of charge distribution by color, total charge density, HOMO, and LUMO for the SW defected C(9,0) capsule.

and LUMO of C(5,5) capsule with 0-type VD are localized on the defect side but while HOMO are distributed mainly on the left side of the capsule, LUMO are distributed nearly to the whole capsule. Both the HOMO and LUMO of the 0-type VD C(9,0) capsule are localized on the defected side and they are

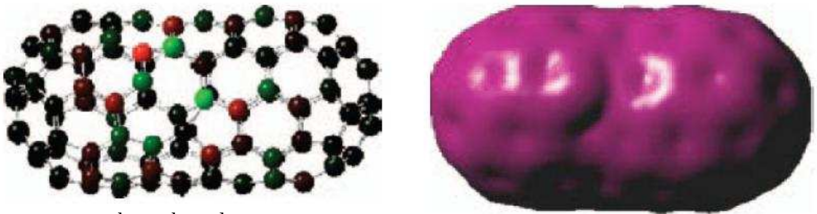

charge by color

charge density

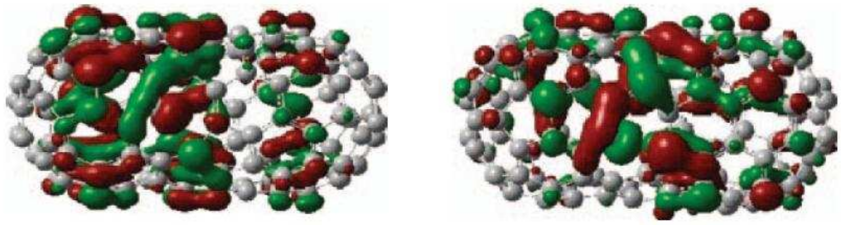

HOMO

LUMO

Figure 3.12: 3D plots of charge distribution by color, total charge density, HOMO, and LUMO for the C(5,5) capsule with 0-type vacancy defect.

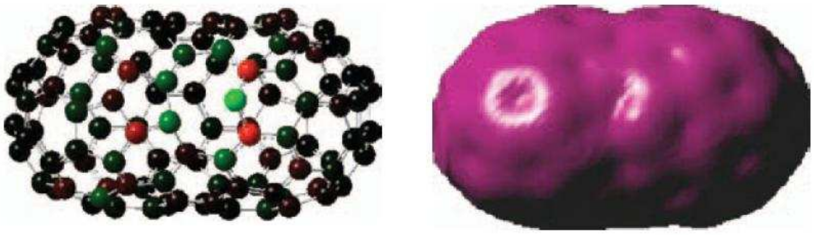

charge by color

charge density

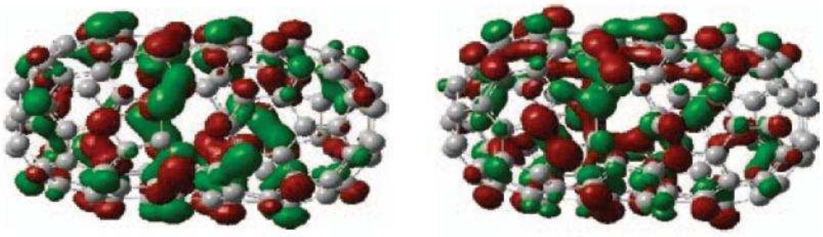

HOMO

LUMO

Figure 3.13: 3D plots of charge distribution by color, total charge density, HOMO, and LUMO for the C(9,0) capsule with 0-type vacancy defect.

distributed to the carbon atoms of the capsule. HOMO and LUMO of C(5,5) capsule with A-type defect are localized on the defected regions but HOMO is more distributed than LUMO on the surface of the capsule. LUMO of the A-type VD C(9,0) capsule is more localized on the defected region than the HOMO and both of them are distributed on the capsule. While HOMO of the C(5,5) capsule with B-type VD is localized on the defected side, LUMO is distributed

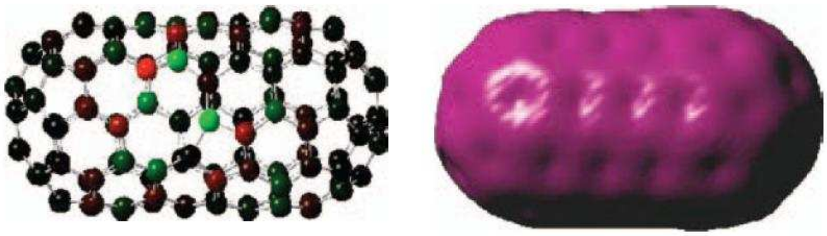

charge by color charge density

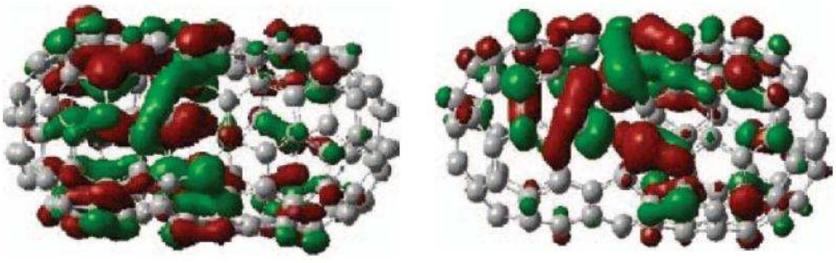

HOMO LUMO

Figure 3.14: 3D plots of charge distribution by color, total charge density, HOMO, and LUMO for the C(5,5) capsule with A-type vacancy defect.

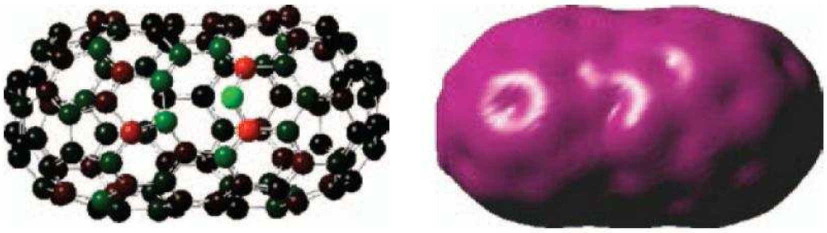

charge by color charge density

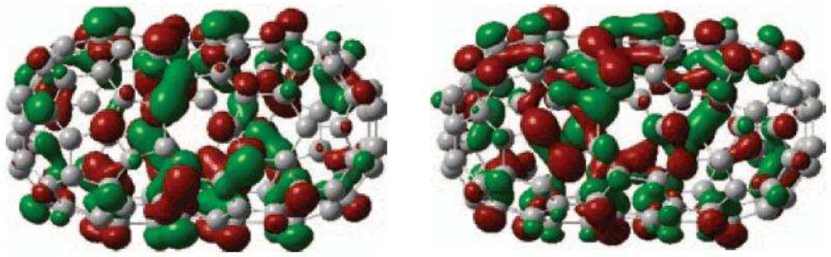

HOMO LUMO

Figure 3.15: 3D plots of charge distribution by color, total charge density, HOMO, and LUMO for the C(9,0) capsule with A-type vacancy defect.

randomly on the surface. HOMO of the B-type VD C(9,0) capsule is more localized on the defected side than the LUMO and while the former is distributed mainly on the middle of the capsule the latter preferred to distribute on the one half of the capsule. Both HOMO and LUMO of C(5,5) capsule with C-type defect are localized on the defect but HOMO are more distributed than LUMO

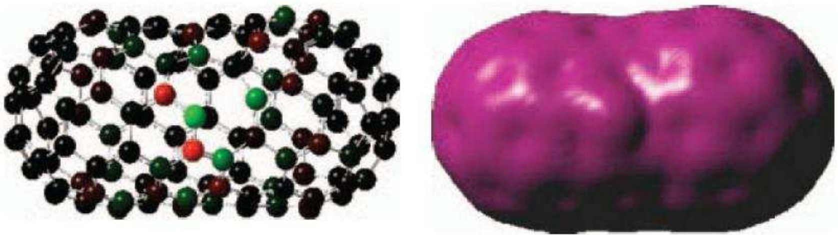

charge by color charge density

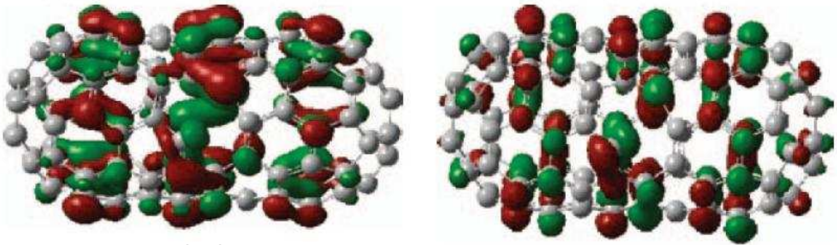

HOMO LUMO

Figure 3.16: 3D plots of charge distribution by color, total charge density, HOMO, and LUMO for the C(5,5) capsule with B-type vacancy defect.

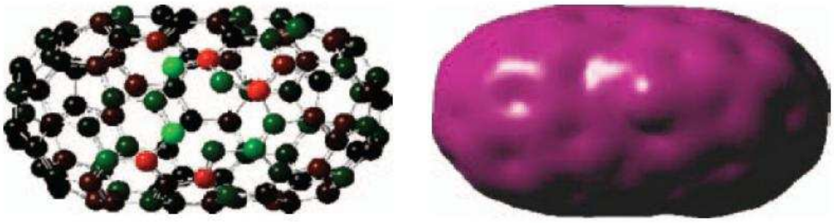

charge by color charge density

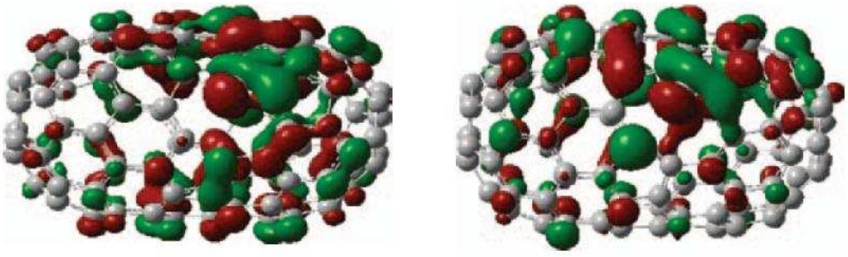

HOMO LUMO

Figure 3.17: 3D plots of charge distribution by color, total charge density, HOMO, and LUMO for the C(9,0) capsule with B-type vacancy defect.

and the former have a horizontal alignment. For the C-type defect of C(9,0) capsule, both HOMO and LUMO are distributed in a similar manner and the localizations can be seen clearly on the defected regions.

Total energy values of the studied systems have been obtained using DFT

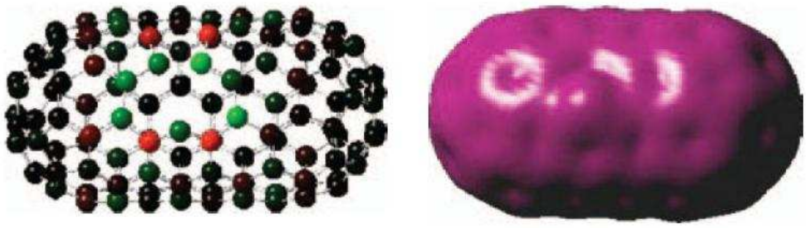

charge by color

charge density

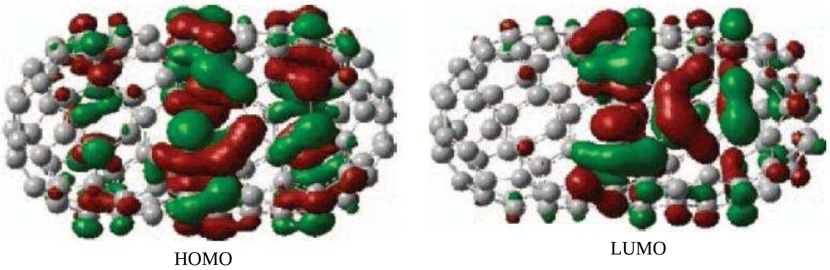

HOMO

LUMO

Figure 3.18: 3D plots of charge distribution by color, total charge density, HOMO, and LUMO for the C(5,5) capsule with C-type vacancy defect.

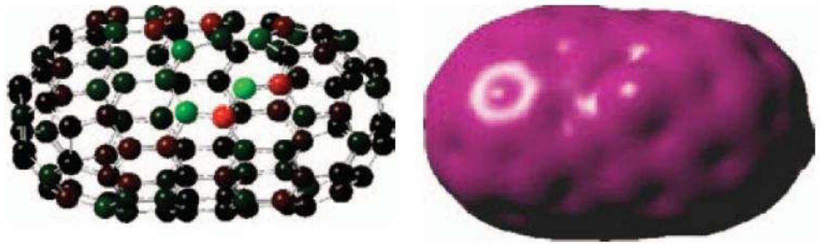

charge by color

charge density

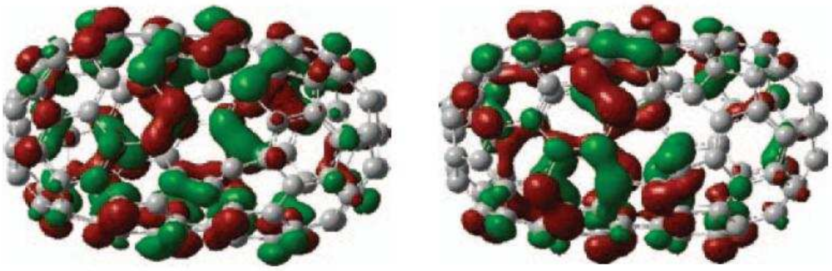

HOMO

LUMO

Figure 3.19: 3D plots of charge distribution by color, total charge density, HOMO, and LUMO for the C(9,0) capsule with C-type vacancy defect.

method with B3LYP functional and 3-21G basis set. The calculations show that defect-free capsules are more stable than the defected ones (Table 3.10). Among the VD structures the A-type and the 0-type ones are the most stable for the C(5,5) and C(9,0) capsules. Molecular dynamics simulations gave the same trend for the C(5,5) capsules however, for the C(9,0) capsules MD found

Table 3.10: Calculated total energy values (in a.u.) of the C(5,5) and C(9,0) systems. MD results (in eV) are given in paranthesis.

System	C(5,5)	C(9,0)
defect-free	-4547.485 (-820.379)	-4320.071 (-554.330)
0-type VD	-4509.360 (-583.350)	-4281.980 (-552.960)
A-type VD	-4509.361 (-584.440)	-4281.938 (-552.960)
B-type VD	-4509.360 (-581.200)	-4281.877 (-552.960)
C-type VD	-4509.270 (-584.440)	-4281.930 (-552.960)
SW type defect	-4547.355 (-596.710)	-4320.014 (-569.180)

Table 3.11: Defect formation energies per atom (in eV/atom) of the C(5,5) and C(9,0) systems.

System	C(5,5)	C(9,0)
0-type VD	0.0523	0.0470
A-type VD	0.0522	0.0572
B-type VD	0.0523	0.0719
C-type VD	0.0728	0.0592
SW type defect	0.0295	0.0136

the same total energy values for the VD capsules. The formation energy/atom values for the SW-defected and VD capsules are presented in Table 3.11 and calculated as the following:

$$\begin{aligned} E_f(SW) &= [E(SW) - E(perfect)]/n \\ E_f(VD) &= E(VD)/n_{VD} - E(perfect)/n \end{aligned} \tag{3.1}$$

where E(SW), E(perfect) and E(VD) are the total energy of the SW-defected, perfect and VD capsules, respectively, and n and n$_{VD}$ are the total number of carbon atoms in the systems. The SW defect formation energies are smaller than that of the VDs which implies that it is easier to form a SW defect on a capsule. The SW defect formation energy/atom of the zigzag capsule is smaller than that of the armchair capsule. While for the C(5,5) VD capsule C-type defect has the highest defect formation energy, for the C(9,0) VD capsule B-type defect has the highest defect formation energy. The calculated SW defect formation energy (3.537 eV) is consistent with another study (3.5 eV) which is performed by using ab initio DFT method [30].

3.4 nLi/nLi$^+$ Ion (n=1-4) Doped Defect-Free Carbon Nanocapsules Studied with DFT method

The structural properties and the energetics of the endohedral nLi/nLi$^+$ ion (n=1-4) doped perfect (pristine, defect-free) capsules have been studied [110]. The optimization procedures of the systems have been carried out using semi-empirical MO method at PM3 level and the energetics have been calculated with the DFT method using B3LYP exchange-correlation functional and 6-31G basis set. The main difference between this study and the study in section 2.2 is that the size of the C(9,0) capsule is taken to be smaller for the present case in order to facilitate the optimizations and the methods used to calculate the energetics of the systems are different. The thermodynamical properties of the optimized systems are obtained from the PM3 type single point energy calculations using HyperChem program and the energetics are calculated using the Gaussian 03 program. The convergence on the energy was set to 10^{-6} au. and the RMS density matrix was set to 10^{-8} au. Initially the lithium atoms and lithium ions have been positioned on the midpoints of the central axis of the capsules and the initial distance between lithium atoms was 3 $\mathring{A}$ in order to prevent from forming clusters as mentioned before. Molecular dynamics simulations have been performed for these systems however, reliable results could not have been obtained as the lithium number increased. The reason could be due to the semi-empirical force field used in the simulations.

The thermodynamical properties (total energy, binding energy, isolated atomic energy, electronic energy, core-core interaction energy, and heat of formation energy) of the nLi/nLi$^+$ ion doped pristine C(5,5) and C(9,0) nanocapsules are given in Tables 3.12 and 3.13, respectively. The results are obtained from the semi-empirical method at PM3 level with single point energy calculations of the optimized geometries. From the point of view of the total and binding energies, nLi atom doped capsules are more stable then nLi$^+$ ion doped capsules for both of the capsule systems. Moreover, heat of formation energies of the nLi$^+$

ion doped systems are larger than that of the nLi atom doped systems and the positive values of the heat of formation energies mean that the processes are endothermic. As the number of Li/Li$^+$ increase in the capsules, the isolated atomic energies and electronic energies become more negative (increase in magnitude) and core-core interaction energies become more positive for both of the type of the systems.

Table 3.12: Calculated energy values (in kcal/mol)(TE: total energy, BE: binding energy, IAE: isolated atomic energy, EE: electronic energy, CCI: core-core interaction, and HOF: heat of formation) of undoped and nLi and nLi$^+$ ion doped pristine C(5,5) optimized systems, where n=1-4 (single point/PM3 results).

Quantity	TE	BE	IAE	EE	CCI	HOF
undoped	-327096.5	-19287.6	-307809.0	-6831305.5	6504208.9	1219.3
1Li@C(5,5)	-327257.3	-19326.1	-307931.2	-6837140.2	6509882.9	1219.1
1Li$^+$@C(5,5)	-327039.2	-19107.9	-307931.2	-6854967.6	6527928.3	1437.2
2Li@C(5,5)	-327267.5	-19214.0	-308053.5	-6878896.5	6551629.1	1369.6
2Li$^+$@C(5,5)	-326918.9	-18865.4	-308053.5	-6876645.1	6549726.2	1718.2
3Li@C(5,5)	-327343.5	-19167.8	-308175.7	-6879801.4	6552457.9	1454.2
3Li$^+$@C(5,5)	-326732.4	-18556.7	-308175.7	-6896853.9	6570121.5	2065.3
4Li@C(5,5)	-327464.7	-19166.8	-308297.9	-6919978.9	6592514.3	1493.7
4Li$^+$@C(5,5)	-326486.2	-18188.3	-308297.9	-6914968.5	6588482.3	2472.2

Table 3.13: Calculated energy values (in kcal/mol)(TE: total energy, BE: binding energy, IAE: isolated atomic energy, EE: electronic energy, CCI: core-core interaction, and HOF: heat of formation) of undoped and nLi and nLi$^+$ ion doped pristine C(9,0) optimized systems, where n=1-4 (single point/PM3 results).

Quantity	TE	BE	IAE	EE	CCI	HOF
undoped	-310707.2	-18288.6	-292418.6	-6317533.8	6006826.6	1192.8
1Li@C(9,0)	-310853.6	-18312.8	-292540.8	-6326905.3	6016051.7	1207.0
1Li$^+$@C(9,0)	-310650.9	-18110.2	-292540.8	-6340154.0	6029503.1	1409.7
2Li@C(9,0)	-310889.6	-18226.6	-292663.0	-6364075.2	6053185.6	1331.7
2Li$^+$@C(9,0)	-310526.9	-17863.9	-292663.0	-6361431.1	6050904.2	1694.4
3Li@C(9,0)	-311033.1	-18247.9	-292785.2	-6369911.2	6058878.0	1348.8
3Li$^+$@C(9,0)	-310340.8	-17555.6	-292785.2	-6380388.7	6070047.9	2041.1
4Li@C(9,0)	-311101.5	-18194.0	-292907.4	-6405258.8	6094157.4	1441.1
4Li$^+$@C(9,0)	-310084.7	-17177.2	-292907.4	-6399220.7	6089136.0	2457.9

The calculated HOMO, LUMO, E$_g$ and the dipole moment (μ) values are given in Tables 3.14 and 3.15. While the E$_g$'s of nLi (n=1,2) doped C(5,5) and C(9,0) capsules are smaller than that of nLi$^+$ ion (n=1,2) doped capsules, the opposite is valid for the n=3,4 case. The trends of the E$_g$'s of the studied systems are presented in Fig. 3.20. Furthermore, the HOMO and LUMO energies of the nLi atom (n=1-4) doped capsules are larger (smaller in magnitude) than that of the nLi$^+$ ion (n=1-4) doped capsules. The dipole moments of the undoped pristine capsules are zero since the capsules have a symmetric geometry after the optimizations. The smallest dipole moment (0.025 Debye) among the studied systems belongs to the 4Li$^+$ ion doped C(5,5) capsule which is highly symmetric.

Table 3.14: Calculated HOMO, LUMO energies (in a.u.), HOMO-LUMO gap (E_g) energies (in eV) and dipole moments (μ, in Debyes) of undoped and nLi/nLi$^+$ ion doped pristine C(5,5) systems (n=1-4). (DFT B3LYP/6-31G results.)

Quantity	HOMO(α)	LUMO(α)	$E_g(\alpha)$	HOMO(β)	LUMO(β)	$E_g(\beta)$	μ
undoped	-0.189	-0.131	1.578	-	-	-	0.000
1Li	-0.162	-0.121	1.116	-0.186	-0.139	1.279	1.301
1Li$^+$	-0.282	-0.224	1.578	-	-	-	1.450
2Li	-0.163	-0.130	0.898	-	-	-	0.463
2Li$^+$	-0.373	-0.316	1.551	-	-	-	1.201
3Li	-0.164	-0.120	1.197	-0.159	-0.138	0.571	2.086
3Li$^+$	-0.465	-0.433	0.871	-	-	-	2.353
4Li	-0.164	-0.118	1.252	-	-	-	0.638
4Li$^+$	-0.556	-0.540	0.435	-	-	-	0.025

Table 3.15: Calculated HOMO, LUMO energies (in a.u.), HOMO-LUMO gap (E_g) energies (in eV) and dipole moments (μ, in Debyes) of undoped and nLi/nLi$^+$ ion doped pristine C(9,0) systems (n=1-4). (DFT B3LYP/6-31G results.)

Quantity	HOMO(α)	LUMO(α)	$E_g(\alpha)$	HOMO(β)	LUMO(β)	$E_g(\beta)$	μ
undoped	-0.188	-0.137	1.388	-	-	-	0.000
1Li	-0.168	-0.122	1.252	-0.187	-0.145	1.143	1.377
1Li$^+$	-0.283	-0.233	1.361	-	-	-	1.095
2Li	-0.170	-0.144	0.708	-	-	-	1.074
2Li$^+$	-0.377	-0.326	1.388	-	-	-	0.053
3Li	-0.169	-0.125	1.197	-0.169	-0.136	0.898	1.826
3Li$^+$	-0.471	-0.454	0.462	-	-	-	0.608
4Li	-0.171	-0.123	1.306	-	-	-	0.357
4Li$^+$	-0.563	-0.549	0.381	-	-	-	0.431

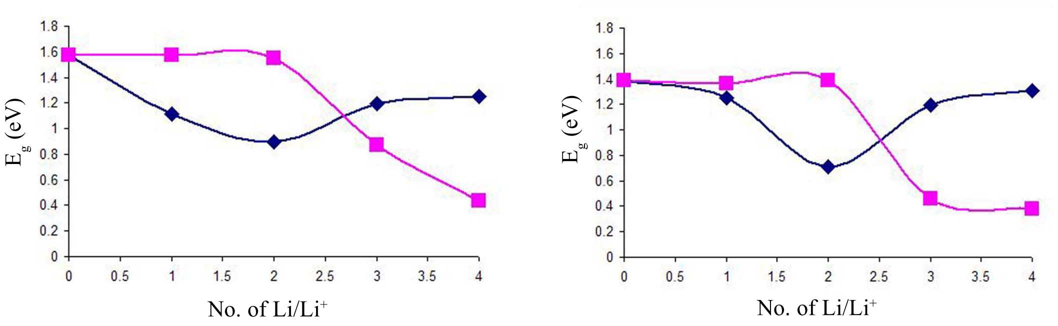

Figure 3.20: The HOMO-LUMO gap (E_g) energy versus the number of Li/Li$^+$ ion in the pristine C(5,5) (left) and C(9,0) (right) capsules. (Squares are for the lithium ions and triangles are for the lithium atoms.)

The 3D plots of the charge by color, HOMO and LUMO of the undoped and nLi/nLi$^+$ ion doped perfect C(5,5) and C(9,0) nanocapsules are presented in Figs. 3.21-3.25. In the figures of charge distribution, green is for positive charges and red is for negative charges. Fig. 3.21a shows that while the charge distribution of the undoped C(5,5) capsule is on the capping cross section, the charge distribution of the undoped C(9,0) capsule is mainly on the tube region, not on the capping region. The HOMO and LUMO localization of the capsules are very low and distributed on the capsules. Figs. 3.22 and 3.23 show the charge by color, HOMO and LUMO of nLi/nLi$^+$ ion doped perfect C(5,5) capsules. From the charge distributions, lithiums are positively charged which means they are ionized and this result is consistent with the other studies [30, 35]. The HOMOs of the systems are delocalized on carbon atoms but the distribution is very low. The LUMOs of the 2Li, 3Li$^+$ ion, and 4Li$^+$ ion cases are localized on the lithiums. Figs. 3.24 and 3.25 show the charge by color, HOMO and LUMO of nLi/nLi$^+$ ion doped perfect C(9,0) capsules. The trends of the distributions are the same with the C(5,5) undoped capsule system.

Total energy values of the pristine capsule systems, which are calculated by performing DFT method with B3LYP/6-31G level, are presented in Table 3.16. The lithium atom doped systems have less energy so they are more stable than the lithium ion doped systems which is the expected result because the C-Li

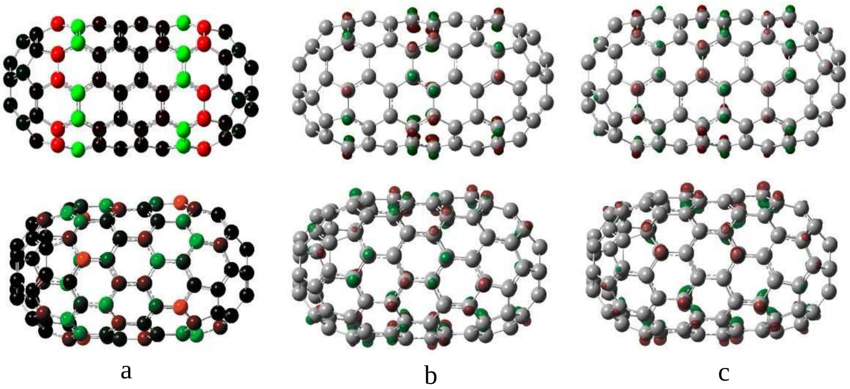

Figure 3.21: 3D plots of charge distribution by color, total charge density, HOMO, and LUMO for the defect-free undoped C(5,5) (upper panel) and C(9,0) (lower panel) capsule.

interaction is stronger than the C-Li$^+$ ion interaction. The binding energies of the systems are calculated using two different approaches: one with not paying attention to the interaction between lithiums and the other with taking into account the lithium interactions. The binding energies for the former and latter cases are presented in Tables 3.17 and 3.18, respectively, and calculated as:

$$E_b = [E(nLi@CNC) - E(CNC) - n * E(Li)]/n \tag{3.2}$$

$$E'_b = [E(nLi@CNC) - E(CNC) - E(nLi)]/n. \tag{3.3}$$

where n is the number of Li/Li$^+$ ion in the systems, E(nLi@CNC) is the total energy of the capsule containing nLi/nLi$^+$ ion, E(CNC) is the total energy of the capsule, and E(Li) is the total energy of Li/Li$^+$. According to the Table 3.17 (Li-Li interaction is ignored) the binding energy of Li atom doped capsules are smaller (larger in magnitude) than the Li$^+$ ion doped cases but not for the 1Li@C(5,5) system. As the number of Li$^+$ ions increase in the systems the binding energy increases which implies that it is less favorable to dope lithium ions into the capsules than to dope lithium atoms. When the Li-Li interactions are considered, the binding energy properties of the systems change. The binding energies of lithium ion doped capsules are more negative than that of lithium atom doped capsules which implies that lithium ion doping is energetically more favorable than lithium atom doping. On the other hand, for the working principles of lithium batteries the movement/diffusion of the lithium is

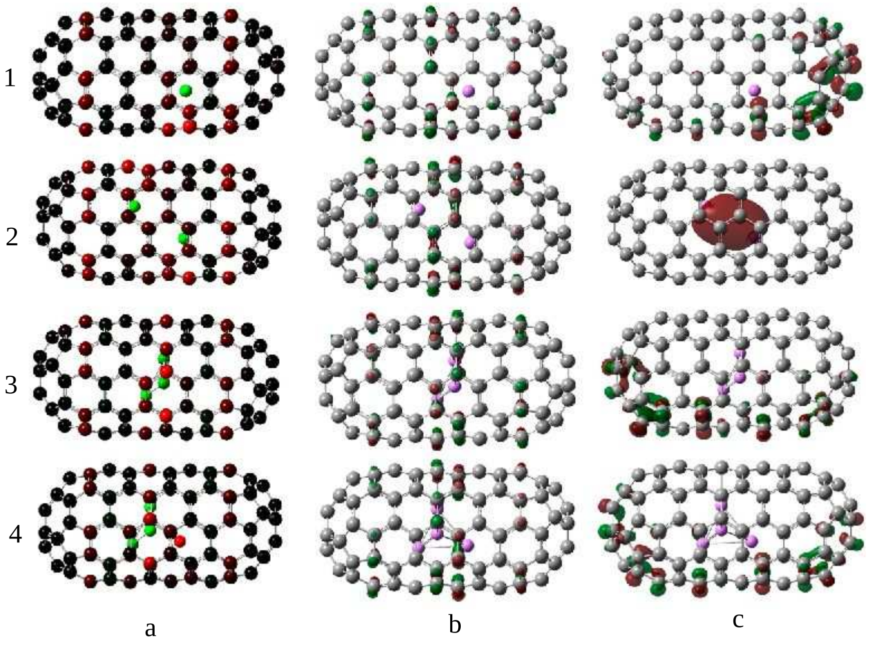

Figure 3.22: 3D plots of charge distribution by color (a), HOMO (b), and LUMO (c) for the nLi@C(5,5) pristine capsules (n=1-4).

an important concept. Thus, lithium atoms move easily through the capsules because of having low binding energies.

Table 3.16: Total energy values (in au) of the pristine C(5,5) and C(9,0) systems undoped and doped with nLi/nLi$^+$ ion (n=1-4) by applying B3LYP level of DFT calculation using 6-31G basis set.

System	C(5,5)	C(9,0)
undoped	-4571.693	-4343.069
1Li/1Li$^+$	-4579.227/-4579.027	-4350.610/-4350.401
2Li/2Li$^+$	-4586.740/-4586.261	-4358.130/-4357.634
3Li/3Li$^+$	-4594.280/-4593.392	-4365.675/-4364.757
4Li/4Li$^+$	-4601.837/-4600.418	-4373.228/-4371.788

3.5 Structural and Electronic Properties of nLi/nLi$^+$ ion (n=1-3) Doped Vacancy Defected Carbon Nanocapsules

The structural and electronic properties of lithium/lithium ion doped C(5,5) armchair and C(9,0) zigzag carbon nanocapsules with mono-atom vacancy defected structures have been studied using quantum chemical treatments and

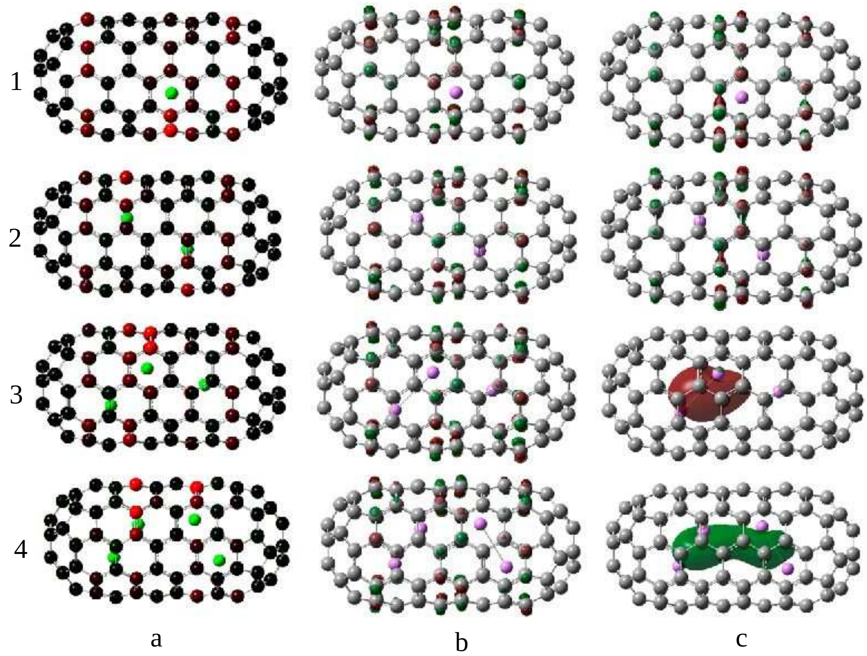

Figure 3.23: 3D plots of charge distribution by color (a), HOMO (b), and LUMO (c) for the nLi$^+$@C(5,5) pristine capsules (n=1-4).

Table 3.17: Binding energy values (E$_b$) per Li/Li$^+$ ion (in eV/Li) of the pristine C(5,5) and C(9,0) systems doped with nLi/nLi$^+$ ion (n=1-4) by applying B3LYP level of DFT calculation using 6-31G basis set. (Li-Li interactions are not considered; from Eq. 3.2.)

System	C(5,5)	C(9,0)
1Li/1Li$^+$	-1.183/-1.340	-1.360/-1.284
2Li/2Li$^+$	-0.892/+0.018	-1.071/+0.052
3Li/3Li$^+$	-1.033/+1.397	-1.209/+1.506
4Li/4Li$^+$	-1.226/+2.809	-1.325/+2.856

Table 3.18: Binding energy values (E$_b$') per Li/Li$^+$ ion (in eV/Li) of the pristine C(5,5) and C(9,0) systems doped with nLi/nLi$^+$ ion (n=2-4) by applying B3LYP level of DFT calculation using 6-31G basis set. (Li-Li interactions are considered; from Eq. 3.3.)

System	C(5,5)	C(9,0)
2Li/2Li$^+$	-0.618/-1.742	-0.752/-1.671
3Li/3Li$^+$	-0.727/-2.179	-0.860/-2.297
4Li/4Li$^+$	-0.872/-2.558	-1.006/-2.623

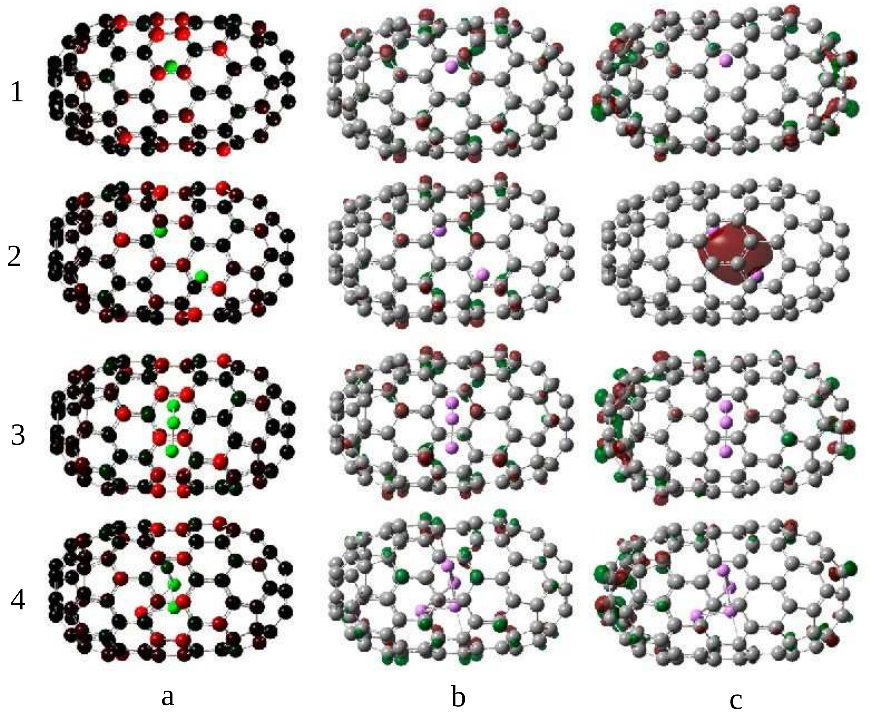

Figure 3.24: 3D plots of charge distribution by color (a), HOMO (b), and LUMO (c) for the nLi@C(9,0) pristine capsules (n=1-4).

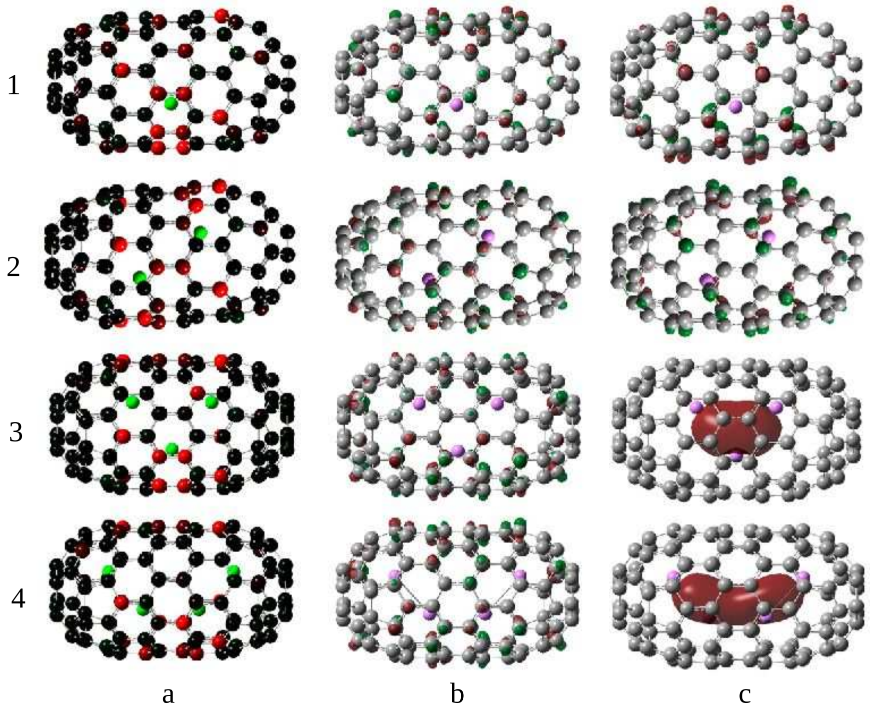

Figure 3.25: 3D plots of charge distribution by color (a), HOMO (b), and LUMO (c) for the nLi$^+$@C(9,0) pristine capsules (n=1-4).

molecular dynamics simulations [111]. The optimization and the single point energy calculation procedures for the present systems are the same with the Li/Li^+ ion doped defect free carbon nanocapsules (previous section). The structural and electronic properties of the mono-vacancy defected C(5,5) and C(9,0) capsules are presented in section 2.3. Among four types of mono-vacancy defects, A-type defected capsules are chosen for the Li/Li^+ ion doping because their defect formation energies and total energies are smaller than the other types of the defects (see section 2.3).

Some thermodynamical properties of the systems such as total energy, binding energy, isolated atomic energy, electronic energy, core-core interaction and heat of formation are presented in Table 3.19. Since the single point energy calculations performed with HyperChem did not converge for a few systems, the related data can not be introduced. For the rest of the systems, lithium ion doped defected capsules have more energy than lithium atom doped capsules which means that lithium atom doped capsules are more stable. These conclusions can be derived from the binding energy data. Moreover, lithium atom doped systems have less repulsive core-core interaction energy and less attractive electronic energy. The systems have positive heat of formation values meaning that the reactions are endothermic. Furthermore, lithium atom doped systems are less endothermic than lithium ion doped systems.

Tables 3.20 and 3.21 presents the calculated dipole moments, HOMO and LUMO energies and the MO energy gaps (E_g) of the C(5,5) and C(9,0) Li/Li^+ ion doped VD capsules, respectively. The HOMO and LUMO of the lithium atom doped capsules are larger (smaller in magnitude) than that of the lithium ion doped capsules. The reactivity of a system is also related to the MO energy gaps. The lower the E_g, the greater the reactivity of the system. Since the E_g of the undoped defected armchair capsule is higher than that of the undoped defected zigzag capsule, the latter is more reactive than the former. While lithium

Table 3.19: Calculated energy values (in kcal/mol)(TE: total energy, BE: binding energy, IAE: isolated atomic energy, EE: electronic energy, CCI: core-core interaction, and HOF: heat of formation) of nLi and nLi$^+$ ion doped vacancy defected C(5,5) and C(9,0) optimized systems, where n=1-3 (single point/PM3 results).

Quantity	TE	BE	IAE	EE	CCI	HOF
1Li@C(5,5)	-324426.9	-19060.8	-305366.2	-6740652.3	6416225.3	1313.5
1Li$^+$@C(5,5)	-324172.6	-18806.5	-305366.2	-6756171.3	6431998.7	1567.9
2Li@C(5,5)	-324383.3	-18894.9	-305488.4	-6762244.9	6437861.6	1517.8
2Li$^+$@C(5,5)	-324045.9	-18557.6	-305488.4	-6779523.2	6455477.2	1855.1
3Li$^+$@C(5,5)	-323869.1	-18258.5	-305610.6	-6796927.2	6473058.1	2192.7
1Li@C(9,0)	-307983.6	-18007.9	-289975.7	-6225042.8	5917059.2	1341.1
1Li$^+$@C(9,0)	-307745.0	-17769.3	-289975.7	-6230995.2	5923250.2	1579.7
2Li@C(9,0)	-308153.9	-18055.9	-290097.9	-6226902.3	5918748.5	1331.5
2Li$^+$@C(9,0)	-307604.7	-17506.8	-290097.9	-6239317.6	5931712.9	1880.6
3Li$^+$@C(9,0)	-307409.5	-17189.3	-290220.1	-6256006.2	5948596.7	2236.5

atom doped defected C(5,5) capsules have smaller E$_g$ than that of lithium ion doped defected C(5,5) capsules, lithium ion doped defected C(9,0) capsules have smaller E$_g$ energies than that of lithium atom doped defected C(9,0) capsules. From these points of view, one can conclude that lithium atom doped C(5,5) systems are more reactive than lithium ion doped C(5,5) systems and lithium ion doped C(9,0) capsules are more reactive than lithium atom doped C(9,0) capsules. For both of the defected capsule systems, HOMO and LUMO energy levels of α-orbital of lithium ion doped systems are smaller than that of lithium doped systems. While the E$_g$ of α-orbitals of lithium ion doped C(5,5) defected capsules are higher than that of lithium atom doped C(5,5) defected capsules, the E$_g$ of α-orbitals of lithium atom doped C(9,0) capsule systems have higher energies than that of lithium ion doped defected C(9,0) capsules (see Fig. 3.26). None of the dipole moments of the studied systems are zero since the systems have no molecular symmetry.

3D plots of charge by color, HOMO, and LUMO of the nLi/nLi$^+$ ion doped vacancy-defected C(5,5) and C(9,0) capsule systems are shown in Figs. 3.27-3.30. All of the Li atoms and Li$^+$ ions are positively charged (green color on the charge by color figures) and the defected sites are mostly negatively charged (red

Table 3.20: Calculated HOMO, LUMO energies (in a.u.), HOMO-LUMO gap (E_g) energies (in eV) and dipole moments (in Debyes) of the nLi/nLi$^+$ ion doped C(5,5) vacancy defected systems (n=1-3). (DFT B3LYP/6-31G results.)

Quantity	HOMO(α)	LUMO(α)	$E_g(\alpha)$	HOMO(β)	LUMO(β)	$E_g(\beta)$	μ
undoped	-0.198	-0.136	1.687	-	-	-	1.131
1Li	-0.178	-0.140	1.034	-0.182	-0.140	1.142	2.043
1Li$^+$	-0.292	-0.237	1.496	-	-	-	0.819
2Li	-0.159	-0.142	0.463	-	-	-	3.091
2Li$^+$	-0.383	-0.331	1.415	-	-	-	1.030
3Li	-0.165	-0.128	1.007	-0.175	-0.146	0.789	3.409
3Li$^+$	-0.476	-0.422	1.469	-	-	-	1.823

Table 3.21: Calculated HOMO, LUMO energies (in a.u.) and HOMO-LUMO gap (E_g) energies (in eV) and dipole moments (in Debyes) of the nLi/nLi$^+$ ion doped C(9,0) vacancy defected systems (n=1-3). (DFT B3LYP/6-31G results.)

Quantity	HOMO(α)	LUMO(α)	$E_g(\alpha)$	HOMO(β)	LUMO(β)	$E_g(\beta)$	μ
undoped	-0.185	-0.152	0.898	-	-	-	1.919
1Li	-0.182	-0.146	0.980	-0.182	-0.146	0.980	1.758
1Li$^+$	-0.255	-0.254	0.027	-	-	-	3.773
2Li	-0.168	-0.129	1.061	-	-	-	14.192
2Li$^+$	-0.370	-0.349	0.571	-	-	-	0.524
3Li	-0.173	-0.126	1.279	-0.182	-0.148	0.925	2.264
3Li$^+$	-0.463	-0.443	0.544	-	-	-	1.706

color on the charge by color figures). The net charge accumulated on Li atoms are larger than that of Li$^+$ ions for the 1Li/1Li$^+$@C(5,5) and 1Li/1Li$^+$@C(9,0) systems, which are 0.635/0.595 and 0.590/0.375, respectively. However, for the other systems, the total charge on Li ions are larger than that of Li atoms. The HOMO and LUMO distributions are similar for 1Li atom doped VD capsules, they are localized on the surfaces of the capsules. Both of the HOMO of 1Li$^+$ ion doped capsules are localized mostly on the defected region. On the other hand, LUMOs are localized on the surface of the capsules. LUMO of the 1Li$^+$@C(5,5) system aligned horizontally and 1Li$^+$@C(9,0) system aligned vertically. While the HOMO of the 2Li@C(5,5) system is localized on the defected region, the LUMO of the same system and both HOMO and LUMO of the 2Li@C(9,0) system are randomly distributed on the capsule surface. Whereas the HOMO

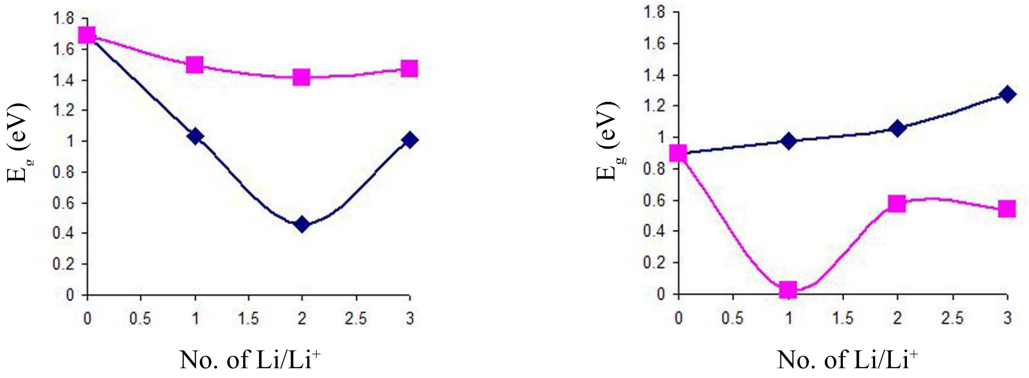

Figure 3.26: The HOMO-LUMO gap (E$_g$) energy versus the number of Li/Li$^+$ ion in the vacancy defected C(5,5) (left) and C(9,0) (right) capsules. (Squares are for the lithium ions and triangles are for the lithium atoms.)

of 2Li$^+$@C(5,5) system is more uniformly distributed on the capsule than the HOMO of 2Li$^+$@C(9,0) system, the LUMOs of the same systems are localized on the defected region. For the three lithium atom doped systems there is no similarity. While the HOMO of the C(5,5) system is not significantly distributed on the capsule, LUMO is localized on the defect. HOMO and LUMO of the 3Li@C(9,0) capsule are distributed on the capsule and the latter is especially on the caps of the capsule. While the HOMO of 3Li$^+$@C(5,5) system is horizontally distributed on the capsule, the LUMO of the same system is localized mainly on the Li ions and on the defect. For the 3Li$^+$@C(9,0) capsule, HOMO is randomly distributed on the capsule and LUMO is localized on the defected region.

The calculated total energy values of the defected doped capsules by applying DFT method and MD simulations are given in Table 3.22. These two different methods predict the same trend for both of the systems. Lithium atom doped defected capsules have less energy which means that these systems are more stable than lithium ion doped capsules. This is an expected result because C-Li interaction is stronger than the C-Li$^+$ interaction.

The calculated average binding energy per Li/Li$^+$ ion is defined by two ways

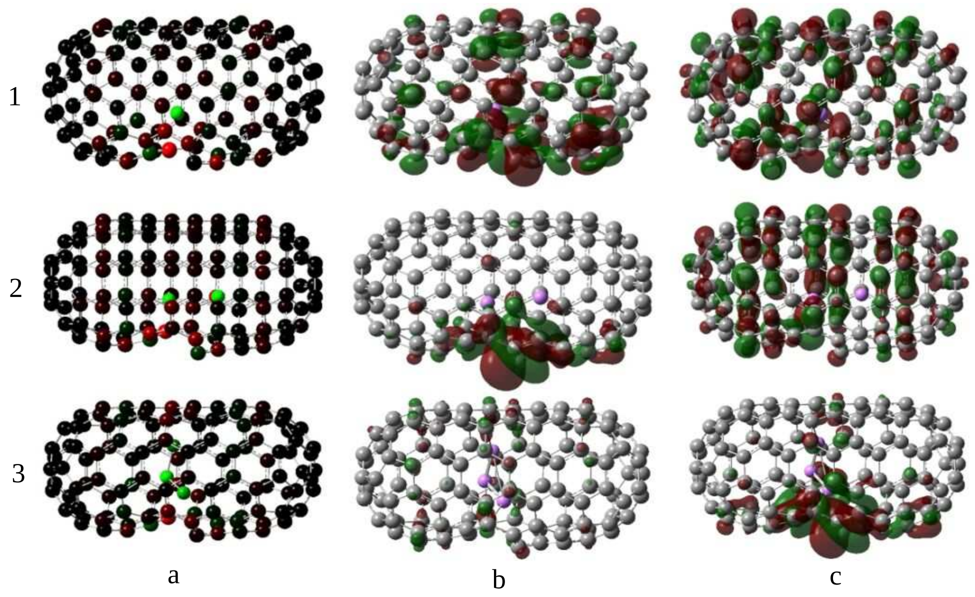

Figure 3.27: 3D plots of charge distribution by color (a), HOMO (b), and LUMO (c) for the nLi atom (n=1-3) doped C(5,5) VD capsules.

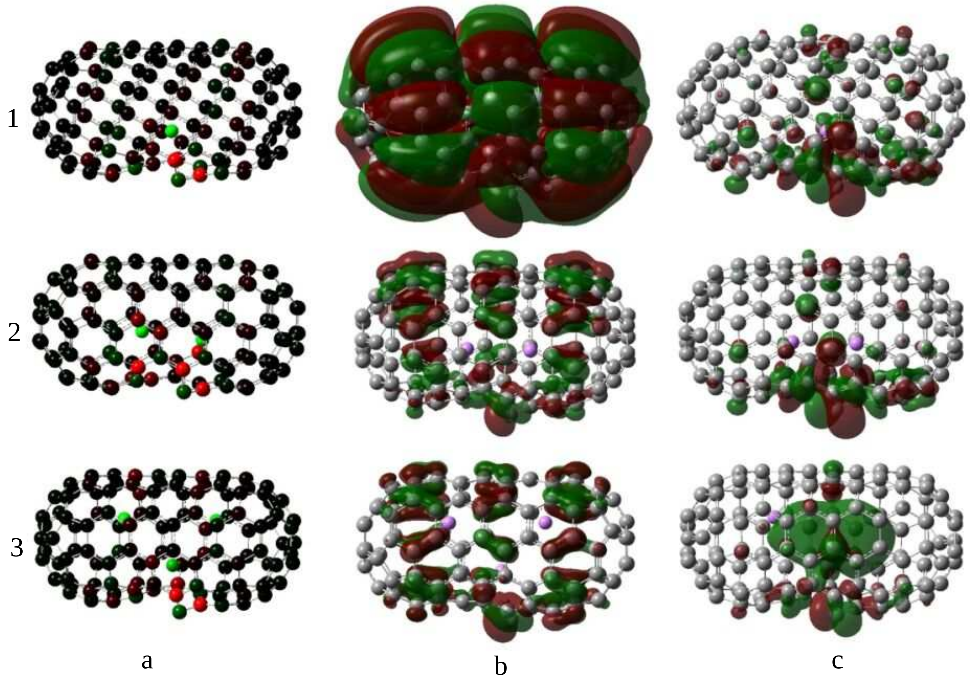

Figure 3.28: 3D plots of charge distribution by color (a), HOMO (b), and LUMO (c) for the nLi$^+$ ion (n=1-3) doped C(5,5) VD capsules.

as mentioned before in the previous section. Equations 3.2 and 3.3 have been used for the calculations. Tables 3.23 and 3.24 present the average binding energies with the Li-Li interaction is not considered and with the Li-Li interaction

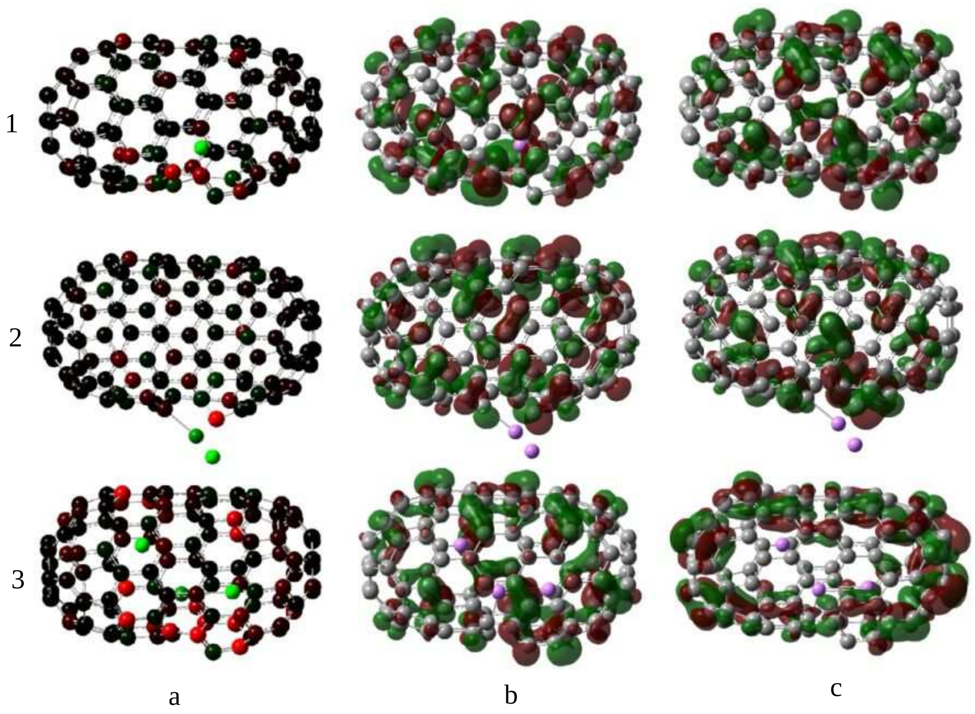

Figure 3.29: 3D plots of charge distribution by color (a), HOMO (b), and LUMO (c) for the nLi atom (n=1-3) doped C(9,0) VD capsules.

Table 3.22: Total energy values (in au) of the C(5,5) and C(9,0) systems doped with nLi/nLi$^+$ ion (n=1-3) by applying B3LYP level of DFT calculation using 6-31G basis set. MD results (in eV) are given in parenthesis.

System	C(5,5)	C(9,0)
without Li/Li$^+$	-4533.356 (-580.890)	-4304.671 (-553.788)
1Li/1Li$^+$	-4540.922 / -4540.699 (-716.651)/ (-630.083)	-4312.269 / -4312.014 (-686.877)/ (-604.779)
2Li/2Li$^+$	-4548.409 / -4547.922 (-848.548)/ (-681.735)	-4319.864 / -4319.243 (-809.876)/ (-655.024)
3Li/3Li$^+$	-4555.953 / -4555.064 (-976.335)/ (-728.805)	-4327.319 / -4326.376 (-936.105)/ (-603.149)

considered, respectively. For the former case, it is energetically most favorable to dope one lithium atom into the both capsules. The average binding energy per lithium ion for 3Li$^+$C(5,5) and 3Li$^+$C(9,0) systems are 1.31 and 1.34 eV, respectively, which means that it is unfavorable to dope three lithium ions into the defected capsules. One can conclude that Li$^+$ ion can move more easily than Li atom from the binding energy point of view. When the Li-Li interactions are

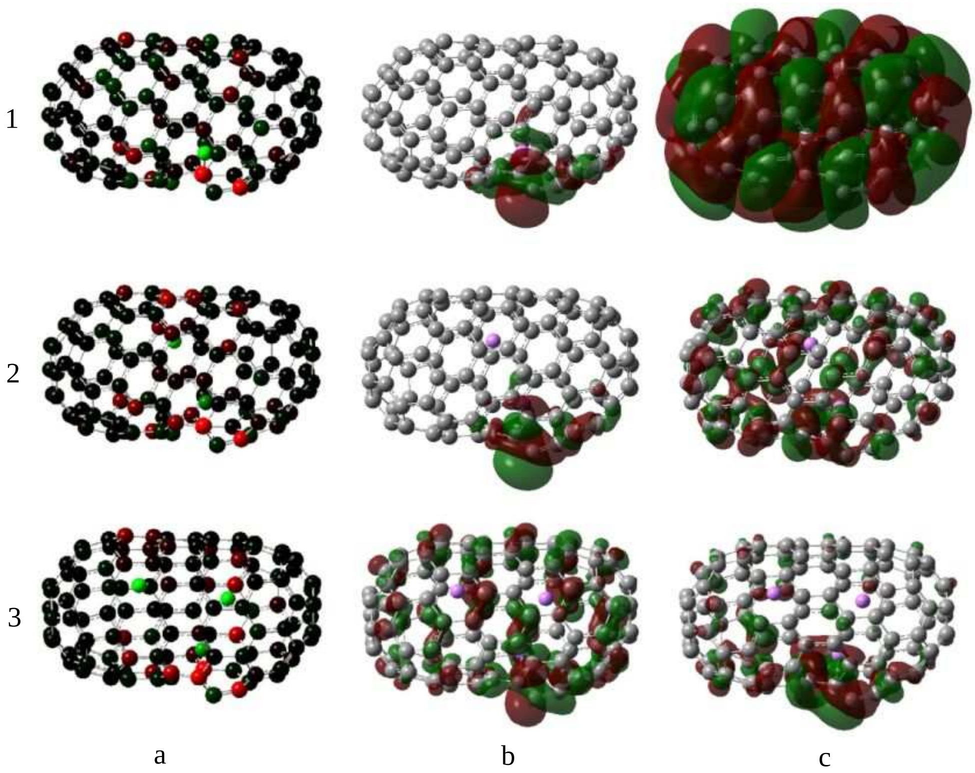

Figure 3.30: 3D plots of charge distribution by color (a), HOMO (b), and LUMO (c) for the nLi$^+$ ion (n=1-3) doped C(9,0) VD capsules.

taken into account, the binding energy values are found to be very different than the other case. For all the cases except 2Li$^+$@C(9,0), the average binding energy per lithium ion is larger in magnitude than the lithium atom, which means that clusters of lithium ion doping is energetically more favorable than clusters of lithium atom doping.

Table 3.23: Binding energy values per Li/Li$^+$ ion (in eV/Li) of the C(5,5) and C(9,0) systems doped with nLi/nLi$^+$ ion (n=1-3) by applying B3LYP level of DFT calculation using 6-31G basis set. (Li-Li interactions are not considered; from Eq. 3.2)

System	C(5,5)	C(9,0)
1Li/1Li$^+$	-2.05/-1.62	-2.92/-1.59
2Li/2Li$^+$	-0.98/+0.03	-2.87/-0.04
3Li/3Li$^+$	-1.14/+1.31	-1.59/+1.34

Table 3.24: Binding energy values per Li/Li^+ ion (in eV/Li) of the C(5,5) and C(9,0) systems doped with nLi/nLi^+ ion (n=2,3) by applying B3LYP level of DFT calculation using 6-31G basis set. (Li-Li interactions are considered; from Eq. 3.3)

System	C(5,5)	C(9,0)
2Li/2Li^+	-0.54/-2.03	-2.46/-2.07
3Li/3Li^+	-0.88/-2.23	-1.20/-2.20

3.6 Structural and Electronic Properties of nLi/nLi^+ ion (n=1-4) Doped Stone-Wales Defected Carbon Nanocapsules

In this section, the energetics and the structural properties of the undoped and nLi/nLi^+ ion (n=1-4) doped Stone-Wales defected C(5,5) and C(9,0) carbon nanocapsules have been investigated using semi-empirical PM3 method for the optimization purposes and DFT method with B3LYP/6-31G for the single point energy calculations [110]. The detailed information for the SW-defected capsules are given in section 2.3. Molecular dynamics simulations did not provide reliable results for these studied systems as the number of lithiums increased so they are not presented.

The thermodynamical properties of the optimized geometries are calculated with semi-empirical MO PM3 method using the HyperChem package. The calculated energies (total energy, binding energy, isolated atomic energy, electronic energy, core-core interaction, and heat of formation) of the SW-defected capsules undoped and doped with nLi/nLi^+ ion (n=1-4) are presented in Tables 3.25 and 3.26. From the point of view of the binding energy values, nLi atom doped capsules are more stable then nLi^+ ion doped capsules. The systems have endothermic heat of formation values. The Li^+ ion doped systems are more endothermic than Li atom doped systems. As the number of Li/Li^+ increases the heat of formation energies become more positive. Furthermore, Li atom doped systems have less heat of formation energy than Li^+ ion doped systems.

Table 3.25: Calculated energy values (in kcal/mol)(TE: total energy, BE: binding energy, IAE: isolated atomic energy, EE: electronic energy, CCI: core-core interaction, and HOF: heat of formation) of undoped and nLi and nLi$^+$ ion doped C(5,5) SW-defected optimized systems, where n=1-4 (single point/PM3 results).

Quantity	TE	BE	IAE	EE	CCI	HOF
undoped	-327009.3	-19200.3	-307809.0	-6822734.4	6495725.1	1306.5
1Li@C(5,5)	-327194.5	-19263.3	-307931.2	-6828728.3	6501533.8	1281.9
1Li$^+$@C(5,5)	-326958.5	-19027.2	-307931.2	-6846016.9	6519058.4	1517.9
2Li@C(5,5)	-327201.0	-19147.6	-308053.5	-6869340.9	6542139.9	1436.0
2Li$^+$@C(5,5)	-326836.7	-18783.3	-308053.5	-6867296.0	6540459.3	1800.3
3Li@C(5,5)	-327295.3	-19119.7	-308175.7	-6876825.4	6549530.1	1502.4
3Li$^+$@C(5,5)	-326654.5	-18478.8	-308175.7	-6888425.8	6561771.4	2143.3
4Li@C(5,5)	-327391.4	-19093.5	-308297.9	-6906540.8	6579149.5	1566.9
4Li$^+$@C(5,5)	-326411.3	-18113.4	-308297.9	-6908045.7	6581634.4	2547.0

Table 3.26: Calculated energy values (in kcal/mol)(TE: total energy, BE: binding energy, IAE: isolated atomic energy, EE: electronic energy, CCI: core-core interaction, and HOF: heat of formation) of undoped and nLi and nLi$^+$ ion doped C(9,0) SW-defected optimized systems, where n=1-4 (single point/PM3 results).

Quantity	TE	BE	IAE	EE	CCI	HOF
undoped	-310666.5	-18247.9	-292418.6	-6313838.9	6003172.4	1233.5
1Li@C(9,0)	-310816.9	-18276.1	-292540.8	-6318275.9	6007459.1	1243.8
1Li$^+$@C(9,0)	-310605.0	-18064.3	-292540.8	-6335361.4	6024756.4	1455.6
2Li@C(9,0)	-310858.9	-18195.9	-292663.0	-6356328.6	6045469.8	1362.4
2Li$^+$@C(9,0)	-310489.2	-17826.2	-292663.0	-6354260.3	6043771.1	1732.1
3Li@C(9,0)	-310951.1	-18165.9	-292785.2	-6361620.2	6050669.1	1430.8
3Li$^+$@C(9,0)	-310307.6	-17522.3	-292785.2	-6372146.1	6061838.6	2074.4
4Li@C(9,0)	-311086.6	-18179.1	-292907.4	-6399632.3	6088545.8	1455.9
4Li$^+$@C(9,0)	-310059.1	-17151.6	-292907.4	-6391866.8	6081807.8	2483.5

The calculated molecular orbital eigenvalues such as HOMO, LUMO, the interfrontier molecular orbital energy gaps, that is LUMO-HOMO energy difference, E_g (see also Fig. 3.31), and the calculated dipole moment values are given in Tables 3.27 and 3.28 for C(5,5) and C(9,0) SW-defected capsules, respectively. HOMO and LUMO energies of Li atom doped systems are larger than that of the Li$^+$ ion doped systems. 4Li$^+$ ion doped C(9,0) has the largest dipole moment value which indicates the highly asymmetric structure.

Table 3.27: Calculated HOMO, LUMO energies (in a.u.), HOMO-LUMO gap (E_g) energies (in eV) and dipole moments (μ in Debyes) of undoped and nLi/nLi$^+$ ion doped C(5,5) SW-defected systems (n=1-4). (DFT B3LYP/6-31G results.

Quantity	HOMO(α)	LUMO(α)	$E_g(\alpha)$	HOMO(β)	LUMO(β)	$E_g(\beta)$	μ
undoped	-0.180	-0.137	1.170	-	-	-	1.028
1Li	-0.170	-0.132	1.034	-0.177	-0.146	0.844	0.834
1Li$^+$	-0.274	-0.233	1.197	-	-	-	1.709
2Li	-0.172	-0.128	1.197	-	-	-	1.101
2Li$^+$	-0.366	-0.324	1.143	-	-	-	0.917
3Li	-0.167	-0.141	0.707	-0.166	-0.137	0.789	1.226
3Li$^+$	-0.455	-0.422	0.898	-	-	-	2.119
4Li	-0.172	-0.126	1.252	-	-	-	1.299
4Li$^+$	-0.547	-0.528	0.517	-	-	-	2.892

Table 3.28: Calculated HOMO, LUMO energies (in a.u.), HOMO-LUMO gap (E_g) energies (in eV) and dipole moments (μ in Debyes) of undoped and nLi/nLi$^+$ ion doped C(9,0) SW-defected systems (n=1-4). (DFT B3LYP/6-31G results.

Quantity	HOMO(α)	LUMO(α)	$E_g(\alpha)$	HOMO(β)	LUMO(β)	$E_g(\beta)$	μ
undoped	-0.181	-0.137	1.197	-	-	-	0.091
1Li	-0.168	-0.127	1.116	-0.179	-0.144	0.952	1.549
1Li$^+$	-0.277	-0.232	1.225	-	-	-	0.632
2Li	-0.171	-0.154	0.463	-	-	-	0.461
2Li$^+$	-0.371	-0.326	1.225	-	-	-	0.840
3Li	-0.170	-0.128	1.143	-0.165	-0.140	0.680	1.092
3Li$^+$	-0.463	-0.461	0.054	-	-	-	0.690
4Li	-0.171	-0.129	1.143	-	-	-	1.342
4Li$^+$	-0.560	-0.542	0.490	-	-	-	2.961

3D plots of charge by color, HOMO and LUMO of the optimized SW-defected undoped and doped capsules are presented in Figs. 3.32-3.36. The charge by color figures for the undoped systems (see Fig. 3.32) show that the excess charges are accumulated mainly on the defected regions. The localizations of the HOMO and LUMO of the undoped capsules are very low and they are localized on the defected sides. Figs. 3.33 and 3.34 show the nLi/nLi$^+$ ion doped C(5,5) SW-defected capsules. For the 2Li, 3Li, 3Li$^+$ ion, and 4Li$^+$ ion doped C(5,5) SW-defected capsules, LUMOs are localized on the lithiums and there is no weight on the carbon atoms. HOMO distribution is very low and they are

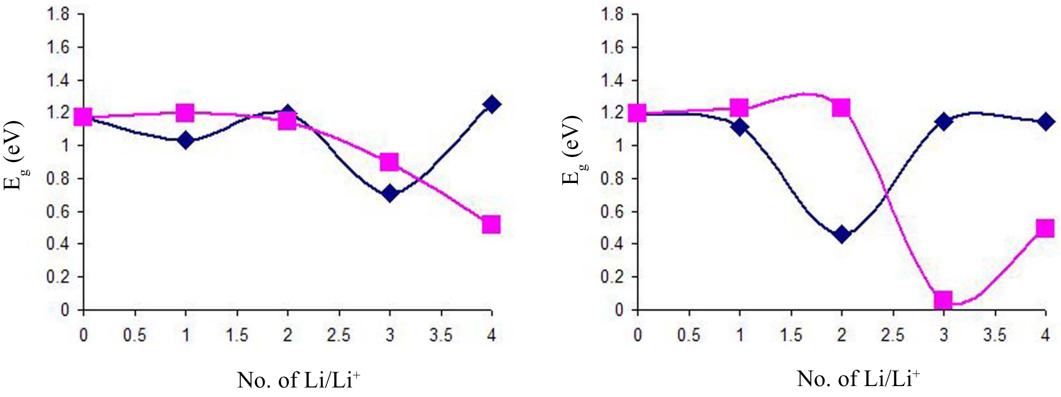

Figure 3.31: The HOMO-LUMO gap (E_g) energy versus the number of Li/Li$^+$ ion in the SW-defected C(5,5) (left) and C(9,0) (right) capsules. (Squares are for the lithium ions and triangles are for the lithium atoms.)

delocalized on carbon atoms, not on lithiums. In Figs. 3.35 and 3.36, similar properties of nLi/nLi$^+$ ion doped C(9,0) SW-defected capsules with C(5,5) capsules are presented. For the 2Li atom doped case, the distribution of HOMO is smaller than the distribution of LUMO and both HOMO and LUMO are localized between the two lithium atoms. For the 4Li$^+$ ion systems, HOMO and LUMO are localized on the Li$^+$ ions and both have very similar structures. For the 3Li$^+$ ion case, the LUMO is localized in between the lithium ions. The HOMO and LUMO distribution of the other systems are delocalized on carbon atoms. From the point of view of the Mulliken charge analysis it is shown that lithiums are ionized, but not for one lithium atom at the 4Li@C(5,5) system, which is consistent with the other results [30, 35]. For all the systems, the charge accumulated on lithium ions are larger than that of lithium atoms.

Total energy values of the doped and undoped SW-defected capsule systems are presented in Table 3.29. The lithium atom doped systems have less energy (higher in magnitude) than the lithium ion doped systems which means that lithium atom doped systems are more stable. The SW defect formation energy is again calculated using:

$$E_f = E(SW) - E(pristine) \tag{3.4}$$

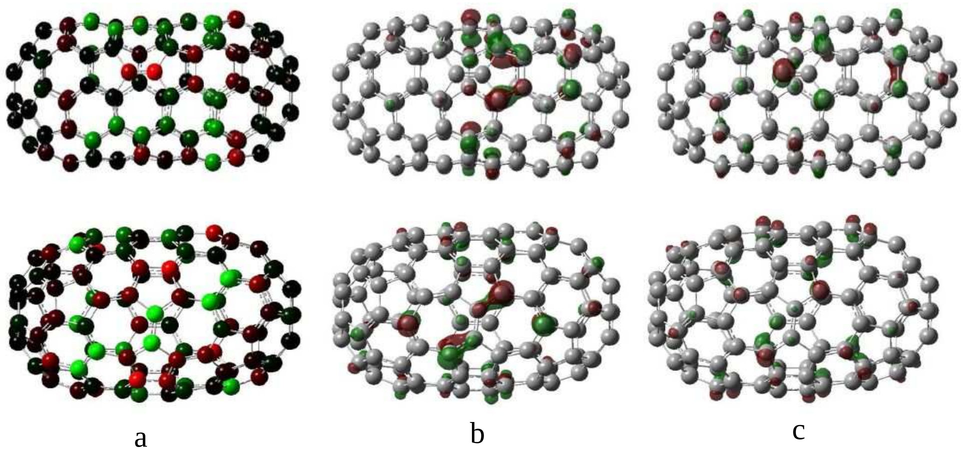

Figure 3.32: 3D plots of charge distribution by color (a), HOMO (b), and LUMO (c) for the C(5,5) (upper panel) and C(9,0) pristine (lower panel) undoped SW-defected capsules.

and the formation energies found to be 3.621 eV and 1.065 eV for the C(5,5) and C(9,0) systems, respectively. Another DFT study [112] using the LDA and GGA found the defect formation energy of C(5,5) SW defected CNT to be 3.90 eV and 4.23 eV, respectively. Meunier et al.[30] found the defect formation energy of C(5,5) tube to be 3.5 eV using ab initio calculations with LDA. The differences between the defect formation energies arise because of the different methods applied in the calculations and while the present calculations are performed for capsule systems, the other calculations are for single walled tube systems. Moreover, in the other studies the total number of carbon atoms are not given so we can not calculate the defect formation energy per atom, which would be a better result for the comparison purposes.

Table 3.29: Total energy values (in au) of the C(5,5) and C(9,0) SW-defected systems undoped and doped with nLi/nLi$^+$ ion (n=1-4) by applying B3LYP level of DFT calculation using 6-31G basis set.

System	C(5,5)	C(9,0)
undoped	-4571.560	-4343.010
1Li/1Li$^+$	-4579.104/-4578.897	-4350.554/-4350.329
2Li/2Li$^+$	-4586.621/-4586.130	-4358.076/-4357.580
3Li/3Li$^+$	-4594.132/-4593.265	-4365.632/-4364.689
4Li/4Li$^+$	-4601.706/-4600.306	-4373.201/-4371.756

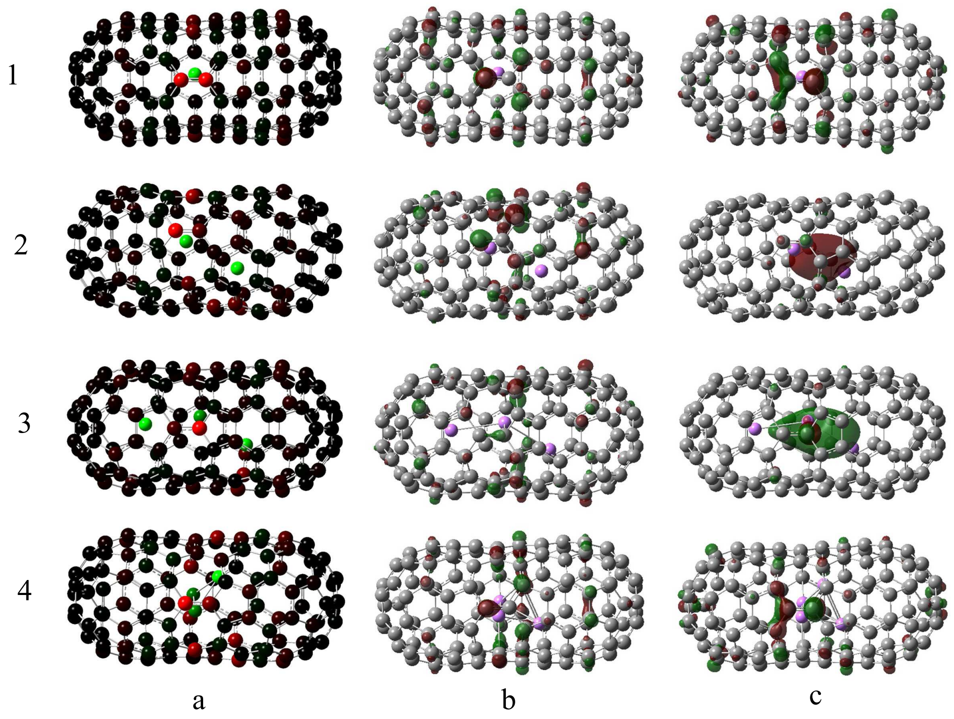

Figure 3.33: 3D plots of charge distribution by color (a), HOMO (b), and LUMO (c) for the nLi@C(5,5) SW-defected capsules (n=1-4).

The binding energies of the systems are calculated with the same consideration in section 2.4 using the Eq. 3.2 and Eq. 3.3. The binding energy values which are calculated not considering the Li-Li interactions and taking into account the Li-Li interactions are presented in Table 3.30 and 3.31, respectively. For the former case, whereas the binding energy of one lithium atom doping is the same for both of the SW-defected capsules, one lithium ion doped pristine C(9,0) capsule has smaller binding energy than the one lithium ion doped C(5,5) pristine capsule. Moreover, it is less favorable to dope lithium ions to the capsules than to dope lithium atoms but not for $1Li^+$ ion doped pristine C(5,5) capsule. For the latter case, binding energies of lithium atom doped capsules are less negative than that of lithium ion doped capsules which implies that lithium ion doping is energetically less favorable than lithium atom doping. Since the movement of lithiums are important for the batteries, lithium atoms moves easily through the capsules due to their low binding energies.

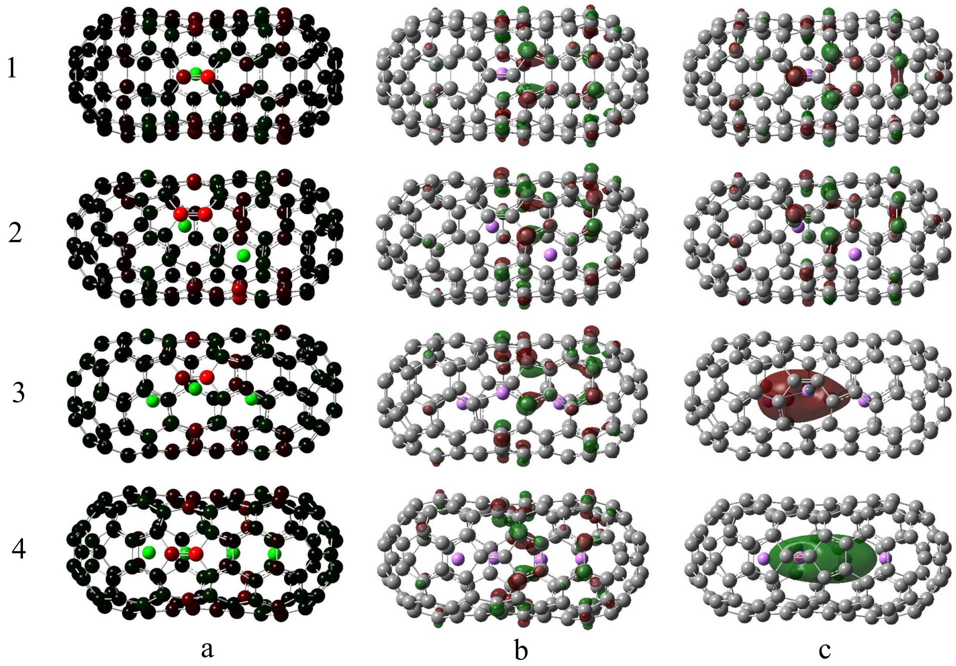

Figure 3.34: 3D plots of charge distribution by color (a), HOMO (b), and LUMO (c) for the nLi$^+$@C(5,5) SW-defected capsules (n=1-4).

Table 3.30: Binding energy values (E_b) per Li/Li$^+$ ion (in eV/Li) of the C(5,5) and C(9,0) SW-defected systems doped with nLi/nLi$^+$ ion (n=1-4) by applying B3LYP level of DFT calculation using 6-31G basis set. (Li-Li interactions are not considered; from Eq. 3.2.)

System	C(5,5)	C(9,0)
1Li/1Li$^+$	-1.45/-1.43	-1.45/-0.92
2Li/2Li$^+$	-1.08/-0.01	-1.15/-0.02
3Li/3Li$^+$	-0.90/+1.34	-1.35/+1.58
4Li/4Li$^+$	-1.24/+2.67	-1.55/+2.67

Table 3.31: Binding energy values (E_b') per Li/Li$^+$ ion (in eV/Li) of the C(5,5) and C(9,0) SW-defected systems doped with nLi/nLi$^+$ ion (n=2-4) by applying B3LYP level of DFT calculation using 6-31G basis set. (Li-Li interactions are considered; from Eq. 3.3.)

System	C(5,5)	C(9,0)
2Li/2Li$^+$	-0.72/-1.95	-0.75/-1.75
3Li/3Li$^+$	-0.51/-2.27	-0.94/-2.60
4Li/4Li$^+$	-0.95/-2.47	-1.15/-2.64

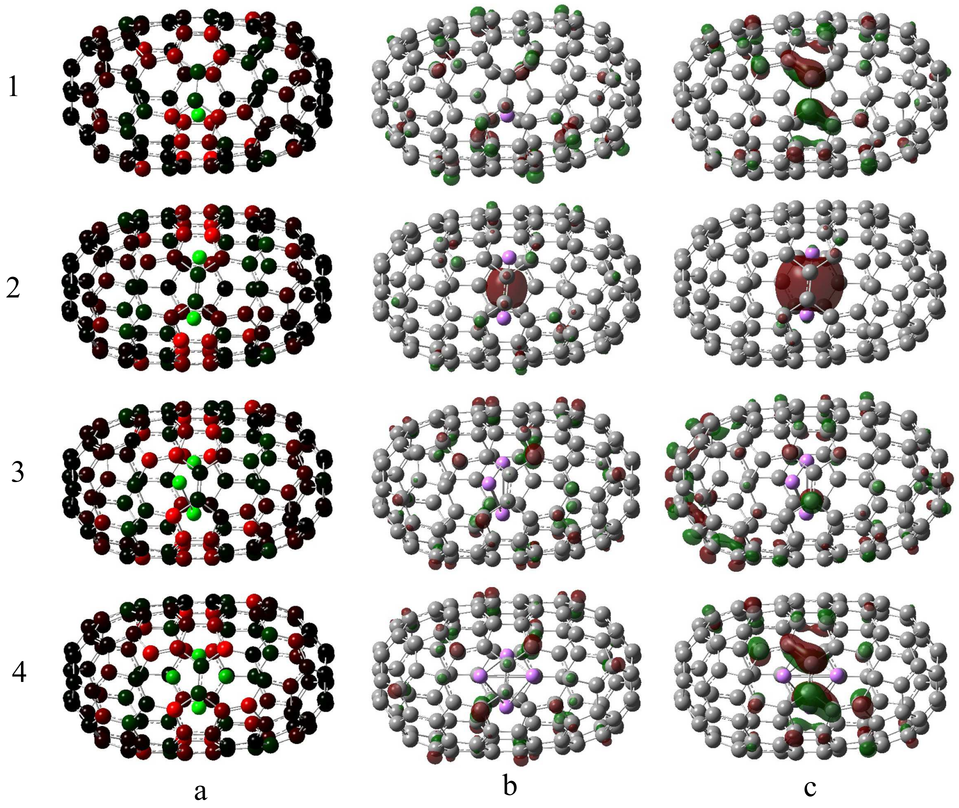

Figure 3.35: 3D plots of charge distribution by color (a), HOMO (b), and LUMO (c) for the nLi@C(9,0) SW-defected capsules (n=1-4).

For the optimized systems, the C-C bond lengths of the SW-defected sites are measured for the capsules (see Fig. 3.37). The C-C bond lengths of the SW-defected site (C1-C2) for the C(5,5) and C(9,0) undoped capsules are 1.326 $\AA$ and 1.417 $\AA$, respectively. When the nLi/nLi$^+$ ions are doped, the C-C bond lengths of 2Li and 3Li doped SW-defected C(9,0) capsule are decreased in a small amount and for other cases, they increased (1.392 $\AA$).

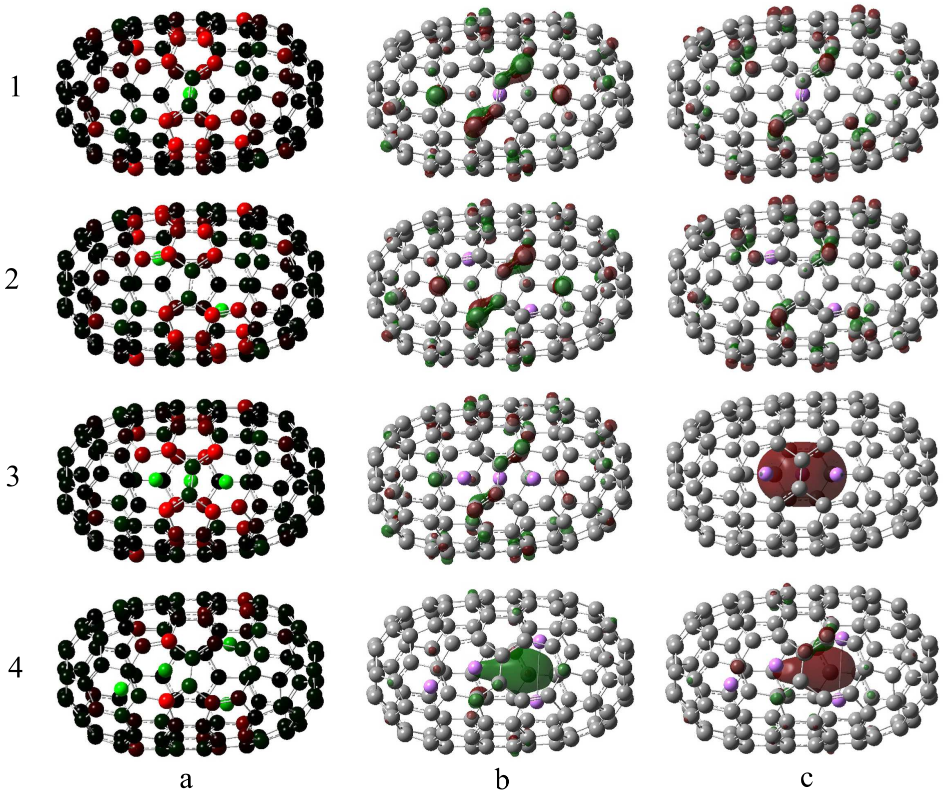

Figure 3.36: 3D plots of charge distribution by color (a), HOMO (b), and LUMO (c) for the nLi$^+$@C(9,0) SW-defected capsules (n=1-4).

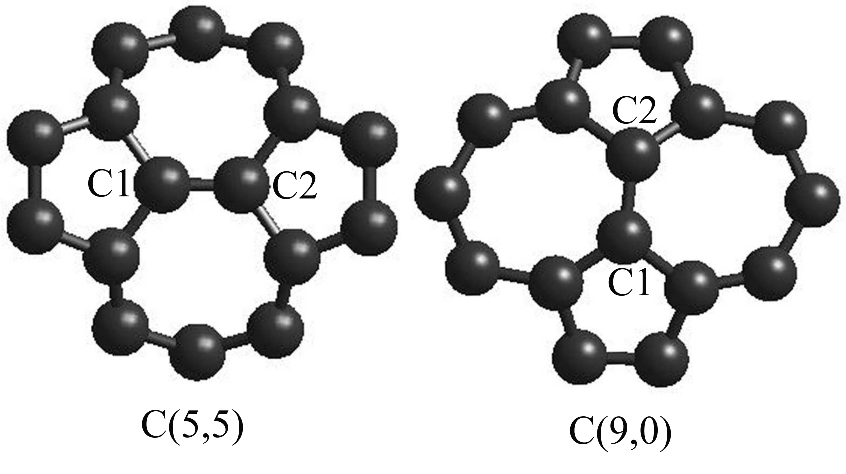

Figure 3.37: Fully relaxed structures of the SW-defected C(5,5) and C(9,0) capsules. The compared C-C bond lengths are represented as C1-C2

CHAPTER 4

CONCLUSION

From the technological point of view, Li/Li$^+$ ion batteries are one of the promising materials for the battery technology. For the Li$^+$ ion batteries, the most popular material for the anode has been graphite. Recently, because of the unique properties of carbon nanotubes such as the intercalation of foreign atoms through the channels and to the interior of the tubes, single walled carbon nanotubes gained a great interest for a strong candidate for the anode material. As well as the perfect structures, the defected carbon structures have been investigated widely for their presence in nature.

In this thesis, Li/Li$^+$ ion interaction with different carbon nano structures such as fullerenes, SWCNTs, SW- and vacancy-defected and defect free carbon nanocapsules have been investigated theoretically using molecular mechanics method with MM+ force field, semi-empirical self-consistent field molecular orbital method at PM3 level and density functional theory calculations with B3LYP exchange-correlation functional using 3-21G or 6-31G basis sets.

The aim of this thesis is to contribute to the lithium ion battery technology by filling the missing parts in the literature. As the experimental studies are expensive and the results can not be foreseen for most of the cases, it is very important to model the experiments and see the results whether it is worth to perform or not.

Some of the important results of the calculations are summarized below:

- Without causing any deformation on the fullerene systems, it was not possible to dope more than one and two lithiums to the C_{20} and C_{60} molecules, respectively.
- For all of the studied systems, the lithium atom doped systems have less energy than the lithium ion doped systems, which means that the Li atom doped systems are more stable than the Li^+ ion doped systems.
- The systems are found to have endothermic heat of formation values and lithium ion doped systems are calculated to be more endothermic than lithium atom doped systems.
- The HOMO and LUMO energies of the lithium atom doped capsules are larger than that of the lithium ion doped capsules.
- The interfrontier molecular orbital energy gaps, that is LUMO-HOMO energy difference, of the nLi/nLi^+ ion doped systems reveals that different structures show different features as the number of Li/Li^+ increases in the nanocapsules. For the most of the Li ion doped capsules, the E_g do not change much until two Li^+ ions doped case then it starts to decrease.
- The defect-free capsules are found to be more stable than the defected ones. Moreover, it is easier to form a SW defect on a capsule because of its smaller formation energy.
- For the undoped SW and vacancy defected structures, the E_g of the C(9,0) capsules are smaller than that of C(5,5) capsules.
- The charge distribution of the systems shows that there is a charge transfer from Li/Li^+ ions to carbon atoms of the nano structures.
- Two different methods have been used to calculate the binding energy values per lithiums: One is with not considering the Li-Li interactions and

the other is Li-Li interactions are taken into account. These two different calculations predicted different binding energy values for the systems.

- As the number of lithiums increased in the defect-free CNC and SW-defected doped CNC systems, the MD simulations could have not been performed properly.

Moreover, lithium atom has a better charge transfer property than the Li^+ ion which is a very important case for battery working principles so lithium metal is a candidate for the electrode material in the batteries.

In addition to these studies on the lithium battery technology, there are numerous works that should be investigated. Experimentally, it was found that the lithium intercalated into SWCNTs at the one third ratio which meant that more Li/Li^+ ion doped structures could be investigated. Furthermore, the effects of the temperature and the electric field on Li/Li^+ ion doping to the systems are worth to investigate which are believed to yield interesting results. Moreover, Li/Li^+ ion doped heteronuclear capsules, such as BN, ZnO, and CBN, might show interesting features; they worth to be investigated as further studies.

REFERENCES

[1] Kroto, H.W., Heath, J.R., O'Brien, S.C., Curl, R.F., Smalley, R.E., Nature 318, 162 (1985).

[2] Iijima, S., Nature 354, 56 (1991).

[3] Lu, J.P., Han, J., Int. J. High Speed Electron. Syst. 9, 101 (1998).

[4] Ajayan, P.M., Chem. Rev. 99, 1787 (1999).

[5] Kratschmer, W., Lamb, L.D., Fostiropoulos, K., Huffman, D.R., Nature 347, 354 (1990).

[6] Dresselhaus, M.S., Dresselhaus, G., Eklund, P.C., "Science of Fullerenes and Carbon Nanotubes", (Academic Press, San Diego, 1996).

[7] Türker, L., Erkoç, Ş., J. Mol. Struct. (Theochem) 638, 37 (2003).

[8] Erkoç, Ş., Int. J. Mod. Phys. C 16, 1553 (2005).

[9] Bendiab, N., Anglaret, E., Bantignies, J.-L., Zahab, A., Sauvajol, J.L., Petit, P., Mathis, C., Lefrant, S., Phys. Rev. B 64, 245424 (2001).

[10] Claye, A.S., Nemes, N.M., Janossy, A., Fischer, J.E., Phys. Rev. B 62, R4845 (2000).

[11] Rao, A.M., Eklund, P.C., Bandow, S., Thess, A., Smalley, R.E., Nature 388, 257 (1997).

[12] Wadhawan, A., Stallcup, R.E., Perez, J.M., Appl. Phys. Lett. 78, 108 (2001).

[13] Cao, A., Zhu, H., Zhang, X., Li, X., Ruan, D., Xu, C., Wei, B., Liang, J., Wu, D., Chem. Phys. Lett. 342, 510 (2001).

[14] Zhu, X.Y., Lee, S.M., Lee, Y.H., Frauenheim, T., Phys. Rev. Lett. 85, 2757 (2000).

[15] Yang, Q.-H., Hou, P.-X., Bai, S., Wang, M.-Z., Cheng, H.-M., Chem, Phys. Lett. 345, 18 (2001).

[16] Dillon, A.C., Heben, M.J., Appl. Phys. A 72, 133 (2001).

[17] Qin, X., Gao, X.P., Liu, H., Yuan, H.T., Yan, D.Y., Gong, W.L., Song, D.Y., Electrochem. Solid State Lett. 3, 532 (2000).

[18] Nisha, J.A., Yudasaka, M., Bandow, S., Kokai, F., Takahashi, K., Iijima, S., Chem. Phys. Lett. 328, 381 (2000).

[19] Peng, S., Cho, K., Nanotechnology 11, 57 (2000).

[20] Kan, M.-C., Huang, J.-L., Sung, J.C., Chen, K.-H., Yau, B.-S., Carbon, 41, 2839 (2003).

[21] Meyer, R.R., Sloan, J., Dunin-Borkowski, R.E., Kirkland, A.I., Novotny, M.C., Bailey, S.R., Hutchison, J.L., Green, M.L.H., Science 289, 1324 (2001).

[22] Che, G., Lakshmi, B.B., Fisher, E.R., Martin, C.R., Nature 393, 346 (1998).

[23] Garau, C., Frontera, A., Quinonero, D., Costa, A., Ballester, P., Deya, P.M., Chem. Phys. Lett. 374, 548 (2003).

[24] Shimoda, H., Gao, B., Tang, X.P., Kleinhammes, A., Fleming, L., Wu, Y., Zhou, O., Phys. Rev. Lett. 88, 015502 (2002).

[25] Kar, T., Pattanayak, J., Scheiner, S., J. Phys. Chem. A 105, 10397 (2001).

[26] Tarascon, J.-M., Armand, M., Nature 414, 359 (2001).

[27] Frackowiak, E., Beguin, F., Carbon 40, 1775 (2002).

[28] Kganyago, K., Ngoepe, P., Phys. Rev. B 68, 205111 (2003).

[29] Khantha, M., Cordero, N., Molina, L., Alonso, J., Girifalco, L., Phys. Rev. B 70, 125422 (2004).

[30] Meunier, V., Kephart, J., Roland, C., Bernhole, J., Phys. Rev. Lett. 88(7), 075506 (2002).

[31] Gao, B., Kleinhammes, A., Tang, X.P., Bower, C., Fleming, L., Wu, Y., Zhou, O., Chem. Phys. Lett. 307, 153 (1999).

[32] Garau, C., Frontera, A., Quinonero, D., Costa, A., Ballester, P., Deya, P.M., Chem. Phys., 297, 85 (2004).

[33] Zhao, M., Xia, Y., Liu, X., Tan, Z., Huang, B., Li, F., Ji, Y., Song, C., Phys. Lett. A 340, 434 (2005).

[34] Udomvech, A., Kercdharoen, T., Osotchan, T., Chem. Phys. Lett. 406, 161 (2005).

[35] Zhao, M., Xia, Y., Mei, L., Phys. Rev. B 71, 165413 (2005).

[36] Ebbesen, T.W., Takada, T., Carbon 33, 973 (1995).

[37] Kosaka, M., Ebbesen, T.W., Hiura, H., Tanigaki, K., Chem. Phys. Lett. 233, 47 (1995).

[38] Charlier, J.-C., Ebbesen, T.W., Lambin, Ph., Phys. Rev. B 53, 11108 (1996).

[39] Sammalkorpi, M., Krasheninnikov, A., Kuronen, A., Nordlund, K., Kaski, K., Phys. Rev. B 70, 245416 (2004).

[40] Gómez-Navarro, C., De Pablo, P.J., Gómez-Herrero, J., Biel, B., Garcia-Vidal, F.J., Rubio, A., Floresi, F., Nat. Mater. 4, 534 (2005).

[41] Gao, B., Bower, C., Lorentze, J., Fleming, L., Kleinhamme, A., Tang, X.P., McNeil, L.E., Wu, Y., Zhou, O., Chem. Phys. Lett. 327, 69 (2000).

[42] Nishidate, K., Sasaki, K., Oikawa, Y., Baba, M., Hasegawa, M., J. Surf. Sci. Nanotech. 3, 358 (2005).

[43] Hypercube Inc. Hyperchem 7.5 Gainesville, FL, USA.

[44] Allinger, N.L., J. Am. Chem. Soc. 99, 8127 (1977).

[45] Weiner, S.J., Kollman, P.A., Case, D.A., Singh, V.C., J. Am. Chem. Soc. 106, 765 (1984).

[46] Jorgensen, W.L., Tirado-Rives, J., J. Am. Chem. Soc. 110, 1657 (1988).

[47] Brooks, B.R., Bruccoleri, R.E., Olafson, B.D., States, D.J., Swaminathan, S., Karplus, M., J. Comput. Chem. 4, 187, (1983).

[48] Gaussian 03, Revision D.01, M. J. Frisch, *et al.*, Gaussian, Inc., Wallingford CT, 2004.

[49] Hartree, D.R., Proc. Cambridge Phil. Soc. 24, 89, 111 (1927).

[50] Hartree, D.R., Proc. Cambridge Phil. Soc. 24, 426 (1928).

[51] Hartree, D.R., Proc. Cambridge Phil. Soc. 25, 225, 310 (1929).

[52] Slater, J.C., Phys. Rev. 51, 846 (1937).

[53] Springborg, M., "Methods of electronic structure calculations", (John Wiley&Sons, New York, 2000).

[54] Born, M., Oppenheimer, R., Ann. Phys. 84, 457 (1927).

[55] Fock, V., Z. Phys. 61, 126 (1930).

[56] Roothaan, C.C.J., Rev. Mod. Phys. 23, 69 (1951).

[57] Hohenberg, P., Kohn, W., Phys. Rev. 136, B864 (1964).

[58] Kohn, W., Sham, L.J., Phys. Rev. 140, A1133 (1965).

[59] Smith, J.R., Phys. Rev. Lett. 25(15), 1023 (1970).

[60] Mahan, G.D., "Many particle physics", (Kluwer Academic/Plenum publishers, 2000).

[61] Vosko, S.H., Wilk, L., Nusair, M., Can. J. Phys. 58, 1200 (1980).

[62] Perdew, J.P., Zunger, A., Phys. Rev. B 23, 5048 (1981).

[63] Lee, C., Yang, W., Parr R.G., Phys. Rev. B 37, 785 (1988).

[64] Perdew, J.P., Wang, Y., Phys. Rev. B 45, 13244 (1992).

[65] Becke, A.D., Phys. Rev. A 38, 3098 (1988).

[66] Perdew, J.P., "Electronic structure of solids '91", (Ed. by P. Ziesche and H. Eschring, Akademie Verlag, Berlin 1991).

[67] Perdew, J.P., Wang, Y., Phys. Rev. B 33, 8800 (1986).

[68] Perdew, J.P., Burke, K., Ernzerhof, M., Phys. Rev. Lett. 77, 3865 (1996).

[69] Becke, A.D., Phys. Rev. A 38, 3098 (1988).

[70] Harris, J., Phys. Rev. A 29, 1648 (1984).

[71] Becke, A.D., J. Chem. Phys. 98, 5648 (1993).

[72] Perdew, J.P., Phys. Rev. B 33, 8822 (1986).

[73] Perdew, J.P., Burke, K., Wang, Y., Phys. Rev. B 54, 16533 (1996).

[74] Slater, J.C., Phys. Rev. 36, 57 (1930).

[75] Hehre, W.J., Stewart, R.F., Pople, J.A., J. Chem. Phys. 51, 2657 (1969).

[76] Collins, J.B., Schleyer, P.V., Binkley, J.S., Pople, J.A., J. Chem. Phys. 64, 5142 (1976).

[77] Pople, J.A., "Theoretical models for chemistry", Proceedings of the Summer Research Conference on Theoretical Chemistry, Energy Structure and Reactivity, (Ed. D.W. Smith. New York: John Wiley&Sons 1973).

[78] Binkley, J.S., Pople, J.A., Hehre, W.J., J. Am. Chem. Soc. 102, 939 (1980).

[79] Dobbs, K.D., Hehre, W.J., J. Comp. Chem. 8, 880 (1987).

[80] Ditchfield, R. Hehre, W.J., Pople, J.A., J. Chem. Phys. 54, 724 (1971).

[81] Gordon, M.S., Chem. Phys. Lett. 76, 163 (1980).

[82] Binning Jr, R.C., Curtiss, L.A., J. Comp. Chem. 11, 1206 (1990).

[83] Rassolov, V.A., Ratner, M.A., Pople, J.A., Redfern, P.C., Curtiss, L.A., J. Comp. Chem. 22, 976 (2001).

[84] Arfken, G., "Mathematical Methods for Physicists", (Orlando, FL: Academic Press, 1985).

[85] Fletcher, R. "Practical Methods of Optimization" (John Wiley&Sons, New York, 1980).

[86] Gill, P.E., Murray, W., Wright, M.H., ”Practical Optimization” (Academic Press, Inc., New York, 1981).

[87] Polak, E., ”Computational Methods in Optimization” (Academic Press, Inc., New York, 1971).

[88] Alder, B.J., Wainwright, T.E., J. Chem. Phys. 27, 1208 (1957).

[89] Alder, B.J., Wainwright, T.E., J. Chem. Phys. 31, 459 (1959).

[90] Stillinger, F.H., Rahman, A., J. Chem. Phys. 60, 1545 (1974).

[91] Allen, M.P., Tildesley, D.J., ”Computer Simulation of Liquids” (Oxford Science Publications, Oxford, 1987).

[92] Frankel, D., Smit, B., ”Understanding Molecular Simulation” (Academic Press, San Diego, 1996).

[93] Haile, J.M., ”Molecular Dynamics Simulation” (John Wiley&Sons, Inc., New York, 1992).

[94] Brenner, D.W., Phys. Rev. B 42(15), 9458 (1990).

[95] Lennard-Jones, J.E., Cohesion, J.E., Proceedings of the Physical Society 43, 461 (1931).

[96] Tersoff, J., Phys. Rev. B 39, 5566 (1989).

[97] Car, R., Parrinello, M., Phys. Rev. Lett. 55, 2471 (1985).

[98] Chakraborti, N., Jayakanth, R., Das, S., Calisir, E.D., Erkoç, Ş., J. Phase Equil. Diff. 28, 140 (2007).

[99] Peköz, R., Erkoç, Ş., J. Nanosci. Nanotech. 8, 675 (2008).

[100] Verlet, L., Phys. Rev. 159, 98 (1967).

[101] Verlet, L., Phys. Rev. 165, 201 (1967).

[102] Hockney, R.W., Meth. Comput. Phys. 9, 136 (1970).

[103] Novoselov, K.S., Geim, A.K., Morozov, S.V., Jiang, D., Zhang, Y., Dubonos, S.V., Grigorieva, I.V., Firsov, A.A., Science 306, 666 (2004).

[104] Dresselhaus, G., Dresselhaus, M.S., ”Physical Properties of Carbon Nanotubes” (Imperial College Press, London, 1999).

[105] Prinzbach, H., Weiler, A., Landenberger, P., Wahl, F., Wörth, J., Scott, L.T., Gelmont, M., Olevano, D., Issendorff, B.V., Nature 407, 60 (2000).

[106] Heermann, D.W., ”Computer Simulation Methods in Theoretical Physics” (Springer-Verlag, New York 1990).

[107] Liu, H.J., Yang, J.L., Chan, C.T., "Nano Science and Technology: Novel Structures and Phenomena" (Ed. by Z. Tang and P. Sheng, CRC Press Taylor and Francis, London 2003).

[108] Peköz, R., Erkoç, Ş., Physica E 36, 211 (2007).

[109] Peköz, R., Erkoç, Ş., J. Comp. Theo. Nanosci. 4, 764 (2007).

[110] Peköz, R., Erkoç, Ş., J. Comp. Theo. Nanosci. (in press).

[111] Peköz, R., Erkoç, Ş., Physica E 40, 2752 (2008).

[112] Nishidate, K., Hasegawa, M., Phys. Rev. B 71, 245418 (2005).

CURRICULUM VITAE

PERSONAL INFORMATION

Surname, Name: Peköz, Rengin

Nationality: Turkish (TC)

Date and Place of Birth: 1 January 1980, Hatay

Phone: +90 312 210 43 30

email: rpekoz@newton.physics.metu.edu.tr

EDUCATION

High School: Anadolu Öğretmen Lisesi, Adana, 1997.

B.S.: METU, The Faculty of Education, Department of The Science Education, Physics Education Programme, June 2002.

M.Sc: METU, The Graduate School of Natural and Applied Sciences, Physics, August 2004.

Spring 2004- present Ph.D. Program, Middle East Technical University (METU), Ankara

PUBLICATIONS

1. Ercan Yılmaz, Rengin Peköz, Cüneyt Can, "Escape of photons and electrons from an HPGe detector at 81 keV" X-Ray Spectrom. **35(1)** 42-46, 2005.

2. Rengin Peköz and Cüneyt Can, "Components of detector response function: Monte Carlo simulations and experiment" X-Ray Spectrom. **35(6)** 347-351, 2006.

3. Rengin Peköz and Şakir Erkoç, "Structural and electronic properties of lithium endohedral doped carbon nanocapsules", Physica E **36** 211, 2007.

4. N. Chakraborti, S. Das, R. Jayakanth, R. Peköz and Ş Erkoç, "Genetic

algorithms applied to Li^+ ions contained in carbon nanotubes: An investigation using particle swarm optimization and differential evolution along with molecular dynamics", Mater. Manuf. Processes, **22(5)** 562, 2007.

5. Rengin Peköz and Şakir Erkoç, "Structural and electronic properties of defected carbon nanocapsules", J. Comp. Theo. Nanosci. **4(4)** 764, 2007.
6. Rengin Peköz and Şakir Erkoç, "Li^+ and Li interactions with carbon nanocage structures", J. Nanosci. Nanotech. **8** 675, 2008.
7. Rengin Peköz and Şakir Erkoç, "Quantum chemical treatment of Li/Li^+ doped defected carbon nanocapsules", Physica E **40** 2752, 2008.
8. Rengin Peköz and Şakir Erkoç, "Density functional theory study on the structural properties and energetics of Zn_mTe_n microclusters" Physica E **40** 2921, 2008.
9. Rengin Peköz and Şakir Erkoç, "Endohedral Li/Li^+ doped Stone-Wales defected carbon nanocapsules", J. Comp. Theo. Nanosci. **6** xxx, 2008 (in press).
10. Rengin Peköz and Şakir Erkoç, "Structural and electronic properties of Ga_mSe_n microclusters: Density functional theory calculations", J. Comp. Theo. Nanosci. (submitted).
11. Rengin Peköz and Şakir Erkoç, "A density functional theory study on the structures and energetics of Cd_mTe_n clusters ($m+n\leq6$)", Comp. Mater. Sci. (submitted).
12. Rengin Peköz and Şakir Erkoç, "The structural and thermodynamical properties and energetics of $C_8(NO_2)_8$ and $C_{20}(NO_2)_{16}$", Phys. Chem. Chem. Phys. (submitted).

PROCEEDINGS PRESENTED IN NATIONAL MEETINGS

1. Ercan Yılmaz, Rengin Peköz, Cüneyt Can, ”Escape of photons and electrons from an HPGe detector at 81 keV”, VIII. National Nuclear Sciences and Technologies Congress”, 15-17 October 2003, Erciyes University, Kayseri, Turkey (Speaker).
2. Rengin Peköz and Cüneyt Can, ”Components of detector response function: Monte Carlo simulations and experiment”, 14-17 September 2004, Turkish Physics Society, Bodrum, Turkey (Speaker).
3. Rengin Peköz and Şakir Erkoç, ”Endohedral Li and Li^+ doped fullerenes: Molecular dynamics simulations”, NANO-TR-II Nanoscience and Nanotechnology, 3-5 May 2006, METU, Ankara, Turkey (Poster).

PROCEEDINGS PRESENTED IN INTERNATIONAL MEETINGS

1. Rengin Peköz and Şakir Erkoç, ”Li^+ and Li interactions with carbon nanocage structures” NANOMAT-2006 International Workshop on Nanostructured Materials, 21-23 June 2006, Antalya, Turkey (Poster).
2. Rengin Peköz and Şakir Erkoç, ”Structural and electronic properties of defected carbon nanocapsules”, 13th International Workshop on Computational Physics and Materials Science: Total Energy and Force Methods, 11-13 January 2007, ICTP-Trieste, Italy (Poster).
3. Rengin Peköz and Şakir Erkoç, ”Structural and electronic properties of $\mathrm{Li}/\mathrm{Li}^+$ doped carbon nanocapsules with mono-vacany defects”, CESEP07, Carbon for Energy Storage and Environment Protection, 2-6 September 2007, Krakow, Poland (Poster).
4. Rengin Peköz and Şakir Erkoç, ”Structural properties and energetics of doped graphene nanoribbons”, Graphene Week 2008, 25-29 August 2008,

ICTP-Trieste, Italy (Poster).

PARTICIPATED MEETINGS AND SCHOOLS

1. International Workshop on Physics Beyond the Standard Model, 22-26 September 2005, Mugla, Turkey.
2. International Conference on Low Energy Antiproton Physics, 16-22 May 2005, Bonn, Germany.
3. NANO-TR-II Nanoscience and Nanotechnology 11-14 June, 2007, Bilkent University, Ankara, Turkey.
4. Advance School on Quantum Monte Carlo Methods in Physics and Chemistry, 21 January-2 February 2008, Trieste, Italy.